

University of Southampton Research Repository ePrints Soton

Copyright © and Moral Rights for this thesis are retained by the author and/or other copyright owners. A copy can be downloaded for personal non-commercial research or study, without prior permission or charge. This thesis cannot be reproduced or quoted extensively from without first obtaining permission in writing from the copyright holder/s. The content must not be changed in any way or sold commercially in any format or medium without the formal permission of the copyright holders.

When referring to this work, full bibliographic details including the author, title, awarding institution and date of the thesis must be given e.g.

AUTHOR (year of submission) "Full thesis title", University of Southampton, name of the University School or Department, PhD Thesis, pagination

UNIVERSITY OF SOUTHAMPTON

FACULTY OF PHYSICAL SCIENCES AND ENGINEERING Physics & Astronomy

Control of Light via Individual Resonant Nanoparticle Devices

by

Daniel James Traviss

Thesis for the degree of Doctor of Philosophy

November 2016

UNIVERSITY OF SOUTHAMPTON

ABSTRACT

FACULTY OF PHYSICAL SCIENCES AND ENGINEERING Physics & Astronomy

Doctor of Philosophy

CONTROL OF LIGHT VIA INDIVIDUAL RESONANT NANOPARTICLE DEVICES

by Daniel James Traviss

This thesis investigates the control of light via isolated nanoparticles of gold or III-V semiconductor gallium phosphide. Nanoscale control of light has a range applications in on-chip devices and optoelectric interfacing, where large arrays of nanoparticles are not always practical.

Simulations, performed using the Boundary Element Method, show semiconductor nanorods to function as two-dimensional cavities, bridging the gap between more commonly used analytical models for a sphere and an infinite cylinder. Dimer structures, made of two nanorods placed end-to-end, are shown to enhance the electric field in the center of the gap, comparable to gold structures of similar design. Experiments, however, show these effects to be elusive. Further simulation using the Finite Element Method indicates that these structures also demonstrate highly directional reradiation of the incident field.

Gold nanoantennas were investigated for their interaction with a phase change material and light carried within a wavguide with the aim of producing an all-optical modulation device. A film of phase change material is shown to be able to rapidly and reversibly modulate the response of a gold nanoantenna. An antenna on top of a rib waveguide is shown to aid in the modulation of a carrier pulse by use of a second pump pulse.

Contents

Li	st of	Publi	cations and Presentations	χi
D	eclar	ation o	of Authorship xi	iii
A	ckno	wledge	ements	īV
N	omer	ıclatur	re xv	ii
1	Intr	oduct	ion	1
	1.1	Applie	cations of nanoparticles	2
		1.1.1	Solar cells and photodetectors	2
		1.1.2	Emitters and lasers	3
		1.1.3	Local near field enhancement	4
		1.1.4	Biomedical applications	4
		1.1.5	Metamaterials	5
		1.1.6	Optical circuits	5
	1.2	Mie T	Theory	6
		1.2.1	Scattering by a sphere	6
		1.2.2	Scattering by an infinite cylinder	7
	1.3	Reson	ances of metallic nanoparticles	9
	1.4	Thesis	s outline	LC
2	Met	thodol	ogy: Simulation, Fabrication, and Measurement Techniques 1	.3
	2.1	Simula	ation	14
		2.1.1	Boundary Element Method (BEM)	14
		2.1.2	Finite Element Method (FEM)	15
	2.2	Fabric	cation	16
		2.2.1	MOVPE growth and FIB milling	16
		2.2.2	Electron-beam lithography and gold deposition	L7
		2.2.3	Thin-film oxide deposition	18
	2.3	Specti	roscopic characterisation	19
		2.3.1	Dark field spectroscopy	20
		2.3.2	Spatial modulation spectroscopy	20
		2.3.3	Pump-probe spectroscopy	22
3	Ant	enna l	Resonances in Low Aspect Ratio Semiconductor Nanorods 2	25
	3.1	Introd	$\frac{1}{1}$	25
	3.2	Single	nanorod simulations	27

vi CONTENTS

		3.2.1 Identification of nanorod modes from near field maps	29
		3.2.2 Scaling of modes with nanorod length	32
	3.3	Near field enhancement	34
	3.4	Varying the angle of incidence	37
	3.5	Conclusions	37
4	T :1	et Conttonium and Entire tion of Circula and Discon Cop Name de	41
4	4.1	nt Scattering and Extinction of Single and Dimer GaP Nanorods Introduction	41 41
	4.1	Methods	41
	4.2	4.2.1 Sample preparation	41
		4.2.1 Sample preparation 4.2.2 Dark field set-up 4.2.2	41
			43
	4.9		
	4.3	Results	45
		4.3.1 Dark field spectroscopy	
	4.4	4.3.2 Spatial modulation spectroscopy	49
	4.4	Discussion	53
		4.4.1 Directional scattering	55
		4.4.2 Angular dependence	
	4.5	Spatial modulation maps	
	4.6	Conclusions	60
5	Gol	d Nanoantennas on VO_2 Thin Film	61
	5.1	Introduction	61
	5.2	Thermochromic transition of a VO_2 film	62
		5.2.1 Transition mechanisms	
		5.2.2 Change to the optical properties	
	5.3	Sample preparation and experimental set-up	66
	5.4	Effect of the IMT on the nanoantenna cross section	67
	5.5	Pulse energy dependent response	71
	5.6	Picosecond time response	
	5.7	Conclusions	
6		d Nanoantennas on Silicon Waveguide Resonators	75
	6.1	Introduction	75 7 5
	6.2	Principles of the rib waveguide	76
		6.2.1 Grating coupler	77
		6.2.2 Directional coupler	78
	6.3	Device design and experimental set-up	78
	6.4	The racetrack resonator	82
	6.5	The effect of the nanoantennas	82
	6.6	Conclusions	87
7	Cor	nclusions	89
	7.1	Summary	89
	7.2	Outlook	90
		THE LEGISLE AS D. N.	6.0
A		litional BEM Simulations of GaP Nanorods Extending the simulation to larger largeths	93
	A.1	Extending the simulation to longer lengths	93

CONTE	ENTS	vii
A.2	Varying the nanorod diameter	94
A.3	Mode characterization and additional near field profiles	95
A.4	Near field enhancement	97

References

103

List of Figures

1.1 1.2	Extinction efficiency of a GaP sphere	
2.1	Growth of a GaP nanowire.	16
2.2	Deposition of nanoantennas by e-beam lithography	
2.3	Illustration of a monochromator	
2.4	Illustration of the dark field microscopy technique	
2.5	Illustration of the spatial modulation spectroscopy technique	21
2.6	Example spatial modulation position scans	21
2.7	Illustration of the pump-probe technique	22
3.1	BEM simulation geometry	
3.2	Extinction efficiency spectra for nanorods of varying lengths	
3.3	Example near field plots of TM modes	29
3.4	Example near field plots of TE modes	
3.5	Example near field plots of higher order modes	31
3.6	Dispersion plots of the nanorod modes	32
3.7	Near field enhancement at the center of a GaP nanorod dimer	
3.8	Angular dependent response of a GaP nanorod	38
4.1	SEM images of milled nanorods	42
4.2	Dark field spectroscopy set-up	
4.3	Comparison of SEM and dark field images	
4.4		
4.5	Improvement of the scattering measurement	45
4.6	Scattering spectra as measured along the length of a nanorod dimer	46
4.7	Measured and simulated scattering spectra from a number of nanorods	47
4.8	Spatial modulation spectra for a number of nanorods	49
4.9	Spatial modulation spectra compared with spectra produced by FEM	
4.40	simulation.	50
	Near field distribution for a nanorod on a glass substrate	52
4.11	Comparison of the spectra measured using the dark field and spatial modulation set-ups	54
4.12	Directionality of the far field emission from Mie resonances	56
4.13	Effect of the finite numerical aperture on the extinction spectrum	57
	Fringes in the spatial modulation signal measured in translation	59
5.1	Crystalographic structure of VO ₂	
5.2	Dielectric function of insulating and metallic VO ₂	65

x LIST OF FIGURES

5.3 5.4	Sample profile and experimental set-up comprising spatial modulation	65
	and pump-probe techniques	67
5.5	Shift of the single nanorod resonance due to the IMT in a VO_2 film	68
5.6	Comparison of normalisation to transmission through modulated and unmodulated VO_2	69
5.7	Shift of the dimer nanoantenna resonance due to the IMT in a VO_2 film.	70
5.8	Continuous tunability of the nanoantenna resonance	71
5.9	Continuous progression of the IMT observed in the modification of the nanoantenna signal.	72
5 10	IMT induced change in the transmission in the presence of a gold nanoan-	•
0.10	tenna.	72
5.11	Temporal response of the IMT observed in the modification of the nanoantenna signal.	73
5.12	Temporal response of the IMT observed in the transmission through the	
0.12	substrate	74
6.1	Schematics of a three layer slab and rib waveguide	77
6.2	Design of the figure-of-eight racetrack resonator device	80
6.3	SEM images of the resonator device	81
6.4	The fiber coupling set-up.	81
6.5	Transmission spectra of nine identical resonator devices	82
6.6	Transmission spectra before and after the deposition of 0, 2 and 4 gold nanoantennas	83
6.7	Transmission spectra in the forward and backward direction through devicess with 0, 2 and 4 nanoantennas deposited on top	84
6.8	Modified set-up to incorperate a second laser for the purpose of a pump-probe experiment.	85
6.9	Pump-probe spectra for devices with 0, 2 and 4 nanoantennas deposited	
	on top	86
A.1	Extinction efficiency spectra for nanorod lengths up to 2.5 μm	93
A.2	Evolution of the field distribution with nanorod length for the b_2^1 TE mode.	94
A.3	Extinction spectra for nanorods of varying diamteter	95
A.4	Evolution of the field distribution with nanorod length for the a_2^n and a_3^n	
	modes	96
A.5	Near field distributions of the b_l^1 TM modes	97
A.6	Near field distributions for the b_3^3 and b_3^5 TE modes	98
A.7	Near field distributions of the b_l^1 TE modes	98
A.8	Mid-gap electric and magnetic field enhancement for TM and TE polari-	99
A.9	Evolution of the field distribution with nanorod length for the b_1^n and b_2^n	
	modes	.00
A.10	Mid-gap electric and magnetic field enhancement compared to an equivalent distance from a single nanorod	.01

List of Publications and Presentations

- D. Traviss, R. Bruck, B. Mills, M. Abb, and O. L. Muskens, "Ultrafast plasmonics using transparent conductive oxide hybrids in the epsilon-near-zero regime," *Appl. Phys. Lett.*, vol. 102, no. 12, p. 121112, 2013.
- D. J. Traviss, M. K. Schmidt, J. Aizpurua, and O. L. Muskens, "Antenna resonances in low aspect ratio semiconductor nanowires," *Opt. Express*, vol. 23, no. 17, pp. 22771-22787, 2015.
- D. J. Traviss, M. K. Schmidt, J. Aizpurua, and O. L. Muskens, "Antenna resonances in semiconductor nanorods," Poster presentation at *SPIE Photonics Europe, Nanophotonics VI* in Brussels, 2016.
- D. J. Traviss, M. K. Schmidt, J. Aizpurua, E. P. A. M. Bakkers, and O. L. Muskens, "Single particle spectroscopy of plasmonic and dielectric antennas," Oral presentation at *E-MRS Spring Meeting* in Lille, 2016.

Declaration of Authorship

I, Daniel James Traviss, declare that the thesis entitled Control of Light via Individual Resonant Nanoparticle Devices and the work presented in the thesis are both my own, and have been generated by me as the result of my own original research. I confirm that:

- this work was done wholly or mainly while in candidature for a research degree at this University;
- where any part of this thesis has previously been submitted for a degree or any other qualification at this University or any other institution, this has been clearly stated;
- where I have consulted the published work of others, this is always clearly attributed;
- where I have quoted from the work of others, the source is always given. With the exception of such quotations, this thesis is entirely my own work;
- I have acknowledged all main sources of help;
- where the thesis is based on work done by myself jointly with others, I have made clear exactly what was done by others and what I have contributed myself;
- parts of this work have been published as: Traviss et al. [1]

Signed:	 	 	
-0			
Data			

Acknowledgements

I make no secret that my approach to physics is definitely one from an experimentalist's side. My motto would be "shoot lasers first and ask questions later" were it not impractical... and potentially dangerous! Instead I take a quote from Bohren and Huffman that I found particularly amusing: "One man's rigor is another man's mortis."

All joking aside, the past four years have certainly been tough and there are many people I need to thank. Research is rarely a solo effort and I could not have done this work without their input and/or support.

First and foremost, I would like to thank my supervisor, Otto Muskens, for giving me the opportunity to do a PhD in his research group. Otto has been a source of knowledge on all aspects of this research; at times it was like there is nothing he doesn't know. Our weekly meetings helped guide me and kept me focused throughout my four years. His insight into academic writing has also been invaluable. It goes without saying that this thesis would not exist without him.

One of the highlights of my time was my visit to San Sebastian, where I was able to meet Javier and Mikolaj and learn so much more about BEM and the theory behind Mie scatterers. I of course thank them for supporting the new comer into their area of research, but I must also thank them for making me feel welcome when I was a stranger in a foreign city.

My experimental work was enabled by several people who helped me prepare my samples. I thank Zondy for teaching me how to use the various apparatus in the physics cleanroom (and for assisting me when I managed to get things wrong). I thank Stuart for his assistance with the FIB milling which produced a number of samples for me to measure. I also thank Yudong for his help with understanding various fabrication techniques and for his own skills in fabrication.

I owe many thanks to my research group for our endless discussions and distractions. In particular, I would like to thank Roman for allowing me to take part in his research when my other projects were failing, for answering the many questions I had, and for helping me in general, especially when Otto was unavailable. I also thank Tom, Simon, Leo, Rebecca and the rest of the research group for being great friends and colleagues throughout the years.

There are, of course, people beyond the world of my research who I could not have done this without. I thank my parents for their support, especially during the final months when they welcomed me back into their home and gave me a place to finish my writing. I thank my girlfriend, Laura, for always being there (even across an ocean) for the good times and the bad, whether I wanted to celebrate or needed to vent my frustrations.

There are many more friends I should thank but I cannot possibly name them all. Thank you all for being a part of this crazy journey.

As I final thought, I would like to say a thank you to those that went before me for showing me it could be done and for your reassurances that there was indeed an end to the seemingly endless writing! ;-p

Nomenclature

BEM Boundary element method

e-beam Electron beam

FEM Finite element method FIB Focussed ion beam

FP Fabry-Pérot

IMT Insulator-to-metal transition, also referred to as IM transition

ITO Indium tin oxide

PEC, PMC Perfect electric and perfect magnetic conductor

PML Perfectly matched layer

SEM Scanning electron microscope

SOI Silicon on insulator
TE Transverse electric
TM Transverse magnetic

 $\sigma_{\text{sca}}(\lambda)$, $\sigma_{\text{ext}}(\lambda)$ Wavelength dependent scattering and extinction cross section $Q_{\text{ext}}(\lambda)$, $Q_{\text{ext}}(\lambda)$ Wavelength dependent scattering and extinction efficiency

Chapter 1

Introduction

The interaction of light with matter defines how we see the world. The principles of transmission and reflection are well understood based on material properties such as its refractive index. When object dimensions are reduced to the order of the wavelength of light, however, we can no longer deal in simple ray optics. A familiar example of this is diffraction, where a beam of light passing through a gap $d \approx \lambda$ will spread out in the direction of the confinement.

Nanoscale particles, with dimensions equal to or below the wavelength of light, demonstrate similarly counterintuitive properties. The strong reduction of size and increased surface to volume ratio result in new physical phenomenon such as quantum confinement and emission, few-electron effects and tunneling, surface-enhanced interactions with molecules and new (photo)chemistry. Collective oscillations in the particle and formation of surface dipoles can result in strong optical resonances that give small nanoparticles their characteristic colors different from bulk materials. Much research has been done on these optical properties of nanoparticles with the goal of manipulating light on the nanoscale. Metal nanoparticles show collective oscillations of free electrons, known as plasmons, while dielectric particles exhibit the scattering capabilities of particles many times their size. Similar to radiowave antennas, nanoparticles are being considered as nanoscale optical antennas for controlling and directing light. One of the many drivers of our research is to achieve optical communication on a minute scale for the purpose of advance optical circuitry and lab on a chip applications.

This chapter will provide some context to the work contained in this thesis, starting with a review of some of the numerous applications of nanoparticles in devices. Following this overview, an introduction to some of the recurring themes of this thesis will be given, including the concept of Mie resonances and surface plasmon resonances in a metal nanoantenna. Finally, an outline of the following chapters is provided.

1.1 Applications of nanoparticles

Although the properties were likely not truly understood, the use of metal nanoparticles can be traced back to the Roman empire, when gold and silver nanoparticles were used to achieve a dichroic glass that transmitted red light and reflected green light. The first scientific study of metal nanoparticles came much later, in 1857, when Faraday investigated the strong colours produced by colloidal gold nanoparticles in solution [2]. A more general solution, applicable to dielectric nanoparticles, was later proposed by Mie in 1908 [3].

As fabrication techniques were developed, the scientific study of metal and dielectric nanoparticles saw a resurgence. Both metal and dielectric nanoparticles come in all shapes and sizes thanks to a number of fabrication techniques. Bottom-up techniques, such as colloidal growth and vapour deposition techniques, are capable of covering large surfaces in nanoparticles and are typically scalable. On the other hand, top-down techniques, such as lithographic processes, can achieve well defined structures with a high resolution. The shape of the particle greatly effects its optical properties, as does its environment. Thus, nanoparticles have been studied for a number of decades and a broad range of applications has developed.

1.1.1 Solar cells and photodetectors

Solar cells are the focus of a great deal of research as scientists try to find clean and renewable sources of energy to replace fossil fuels. The current issue with solar cells is the material cost. The most ubiquitous solar cell technology relies on crystalline silicon wafers that are between 200 and 300 μ m thick and account for up to 40% of the cost of the cell. Nanoparticles offer the oportunity to reduce that material cost by greatly improving the absorption depth in the silicon (or other semiconductor) wafer, therefore reducing the thickness of wafer required for the solar cell to be viable.

One way to reduce the thickness of the absorbing material needed is to "trap" the incident light within the solar cell. This can be achieved by making use of the large scattering cross section of metal nanoparticles. Several works have shown that using plasmonic nanoparticles can lead to a significant enhancement of the energy conversion efficiency in semiconductor wafers less than 2 µm thick [4, 5]. There are a number of factors that effect the level of enhancement that can be achieved. The size and shape of the nanoparticles as well as the spacing between nanoparticles all play a role in how effectively incident light can be trapped and absorbed.

Semiconductor nanoparticles have proven to be particularly useful in producing more effecient solar cells. In comparison to plasmonic nanoparticles, semiconductor nanoparticles have a greatly reduced, if not negligible, absorption cross section. This is often a source of unwanted energy loss to heating in metalic systems. Semiconductor nanoparticles were originally introduced to replace thick film electrodes and thereby increase the surface area for dye molecules to bind to. It was later found that using a densely packed array of single-crystaline nanowires improved performance further as electron transport through such nanowires is several orders of magnitude faster [6]. Using, instead, an upright nanowire forest allows for the trapping of light through random scattering, keeping light in the cell until it can be absorbed. Core-shell growth allows the nanowires themselves to be the absorbing medium by producing a radial p-n junction, providing a structure with a large surface area and short distance for carriers to travel [7, 8].

A number of properties useful to improving solar cells also lend themselves to use in photodetectors. While some work has been done using plasmonic nanoantennas to improve the response of a semiconductor photodetector by near field enhancement [9] and hot electron injection [10], a greater focus has been directed at semiconductor nanowires. By modifying the length of nanowires, it is possible to tune the wavelength range to which they are sensitive. Attaching electrical contacts to a nanowire allows us to make a photodetector device [11–13]. In this scheme, light incident on the nanowire excites carriers which increase the nanowire's conductance, which is detected via a bias applied across the nanowire. Due to the large aspect ratio of these nanowires, they can be made into polarisation sensitive devices. It has been shown that a photodetector can be engineered from a nanowire such that longitudinal light is absorbed while the nanowire remains virtually invisible under transverse polarised illumination [14]. Further work has resulted in avalanche photodiodes, greatly increasing the sensitivity of such nanowire devices [15].

1.1.2 Emitters and lasers

In addition to detectors, nanowire type structures can also be used as emitters. Several works have looked in to using semiconductor nanopillars as a cavity for lasing [16–19]. The 1D geometry of a nanowire, combined with its high refractive index and well defined growth process, makes for excellent nanoscale photonic cavities. Modifying the length of the nanopillar changes the length of the cavity, thus allowing the operational wavelength to be tuned. This allows the creation of a multicoloured device by producing an array of different heights. Not all modes show the same emission, however. The work of Maslov and Ning demonstrated that the maximum emission from the hybrid HE_{11} mode was parallel to the nanorod axis, while the pure transverese modes, TM_{01} or TE_{01} , emitted radiation at an angle between 30° and 50° [20]. The directionality of the emitted light increases with smaller radii resulting in a trade-off with laser gain.

Devices are not limited to lasers. It has also been shown that, by embedding a quantum dot in a nanowire, it is possible to devise a single photon emitter [21, 22] and further work has resulted in a device capable of emitting entangled photon pairs [23]. Such work

has applications in quantum computing where miniaturised sources of single photons are required, the photons acting as a quantum bit (qubit) of information.

1.1.3 Local near field enhancement

A number of applications have arisen from studying the near field effects of metalic nanoparticles. Near field enhancement has been employed in photolithography to focus the energy, thereby allowing for a resolution that is below the diffraction limit [24]. For imaging techniques, near field enhancement from plasmonic nanostructures has been shown to greatly improve the fluoresence of some particles [25, 26]. Other fluoresence markers are quenched in close proximity to metal nanoparticles [27, 28]. This has been used for target specific imaging and detection of proteins in living cells [29].

One of the most common uses of plasmonic near field enhancement is in surface-enhanced Raman spectroscopy (SERS). This spectroscopy technique uses the inelastic (Raman) scattering of photons to identify molecules. The photon energy is shifted by an amount equal to the molecular vibration of the material, producing a unique Raman spectrum. SERS is the result of an enhancement to the Raman emission from molecules bound to a rough metal surface, or film of nanoparticles, through the excitation of localised surface plasmons resonances and subsequent amplification in the near field [30–33].

1.1.4 Biomedical applications

Metallic nanoparticles have also found use in various biomedical applications. Biosensing, for example, can be done by taking advantage of the sensitivity of nanoparticle resonances to the surrounding medium. By attaching binding sites to a gold nanoparticle, such as an appropriate antibody, the presence of a specific biomolocule can be detected by looking for a shift in the nanoparticle's resonance [34–36]. The sensitivity has been further improved by using a Fano resonance produced by interfering modes, a shift in the asymmetric line shape being easier to detect [37].

Tuning of the nanoparticle resonance has proven useful in the treatment of cancer [38, 39]. It has been shown that colloidal gold nanoparticles are readily taken up by certain cancer cells [40]. The resonances of the nanoparticle can be tuned to the infrared, allowing for maximum penetration of light through the tissue. The ability to tune both scattering and absorption of the nanoparticles allows for both tumor imaging and targeted cell destruction.

1.1.5 Metamaterials

An array of closely packed resonant nanostructures can be used to achieve unusual material properties that are not available naturally. Such a structure is known as a metamaterial. Notable properties achieved by metamaterials are negative refractive index and optical cloaking. A three dimensional array of split ring resonators produces a material in which light "bends the wrong way" at an interface, as if it has been reflected by a mirror nearly perpendicular to the surface [41]. Similarly, concentric rings of split ring resonators have been shown experimentally to be able to almost completely mask the presence of a conducting cylinder for a narrow band of microwave frequencies [42]. Two dimensional metasurfaces also show great promise in replacing glass optics with much thinner devices where the active region is on the scale of the free-space wavelength [43].

1.1.6 Optical circuits

Although we have covered a broad range of applications, this is not an exhaustive list. The main application of the work contained in this thesis is in the design of photonic circuits. Photonics has already provided an effective method of data communication via optical fibres, however the integration of photonics and electronics has now become a limiting factor; the exchange of information between the two regimes is inefficient in terms of both time and energy. One solution is to move towards optical signal processing, requiring the design of optical circuits. Of course, the vast majority of technology is based on electronics, necessitating the eventual change of information back into electronic form. Optical circuits thus need to be able to emit light based on electrical excitation, effectively guide the light, and finally detect light and convert it back into an electrical current. Individual components capable of the emission and detection of light have already been mentioned above, however, work still needs to be done in order to be able to efficiently combine these into a single product.

The work in this thesis focuses on two areas. Firstly, an in-depth investigation into the response of low aspect ratio semiconductor nanorods to incident light, particularly focusing on the scattering and extinction of such structures. In this regime, the nanorods take on a two dimensional behaviour rather than the quasi-one dimensional nature of the longer structures typically used. By expanding the knowledge of these nanowire applications, we hope to further the progress of dependent structures, particularly in the use of nanoscale photonic cavities. The second area is looking towards optical switching via hybrid plasmonic devices. The ability to switch one optical path based on the input a second optical input is the basis for signal processing and rerouting. Before we move on to this work, we first introduce some fundamental concepts to aid the understanding of the later chapters.

1.2 Mie Theory

The scattering of light by small particles can be described by a number of formulations. Rayleigh scattering, for example, describes the scattering of light by particles much smaller than the wavelength. In this regime, the scattering is independent of the particle's size and shape. If we wish to achieve resonant scattering with a means of tunability, we must use larger particles with dimensions on the same order as the incident wavelength. In this regime, analytical solutions to Maxwells equations have been developed to describe the scattering of light by a number of different particles. These solutions are collectively referred to as Mie Theory, named after Gustav Mie. In 1908, Mie published the solution for an electromagnetic plane wave scattered by a homogeneous sphere [3], though Ludvig Lorenz and Peter Debye developed their own solutions around the same time. For this reason, the particular Mie Solution sometimes goes by a combination of names.

Over one hundred years later and the Mie solution has been reproduced and adapted many times over. The formulation used in this thesis is taken from Absorption and Scattering of Light by Small Particles by Bohren and Huffman [44], and focuses on two key solutions. These are the extreme cases of the structures studied in Chapters 3 and 4; the solution to the sphere and the solution to the infinite cylinder. These analytical models form the basis of our investigation in these chapters and provide a point of reference as we establishthe nature of the resonances within our structures.

1.2.1 Scattering by a sphere

The scattered field of a sphere consists of a summation of various modes. Each mode is weighted by a coefficient which takes one of two types; a_l and b_l . The most intuitive interpretation of these coefficients is that they represent the contribution from either electric type or magnetic type multipolar resonances. The a_1 coefficient, for example, represents the electric dipolar contribution, while the b_2 coefficient represents the magnetic quadrupolar contribution.

The coefficients allow the scattering and extinction cross sections of a sphere to be defined by two relatively simple equations. The scattering cross section is defined by

$$\sigma_{\text{sca}} = \frac{2\pi}{k^2} \sum_{l=1}^{\infty} (2l+1)(|a_l|^2 + |b_l|^2), \tag{1.1}$$

and the extinction cross section is defined by

$$\sigma_{\text{ext}} = \frac{2\pi}{k^2} \sum_{l=1}^{\infty} (2l+1) \text{Re}\{a_l + b_l\},$$
 (1.2)

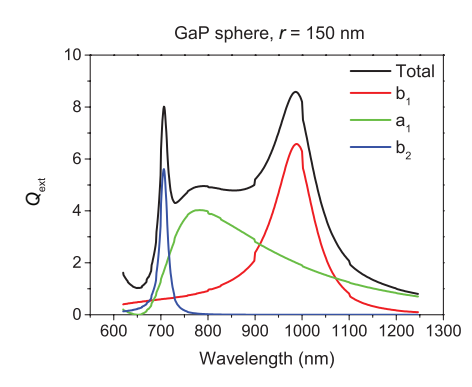


Figure 1.1: Extinction efficiency for a GaP sphere with radius r = 150 nm. Individual resonances, associated with the multipolar modes of the sphere, can be identified. The first three resonances are shown: the magnetic dipole (b_1) , the electric dipole (a_1) and the magnetic quadrupole (b_2) .

These are equations 4.61 and 4.62 in [44]. The a and b coefficients themselves have rather more complicated expressions, based on Bessel and Hankel functions. The variables in the formulation of these coefficients are m and x, which are the relative refractive index and the size parameter, respectively, and are defined as:

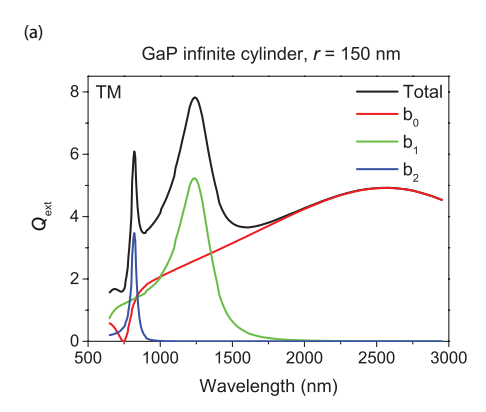
$$m = \frac{k_1}{k} = \frac{N_1}{N}, \quad x = kr = \frac{2\pi Nr}{\lambda}.$$

Here, k_1 is the wavevector within a sphere of refractive index N_1 and radius r, and k is the wavevector in the surrounding medium with refractive index N. The wavevector is defined as $k = 2\pi N/\lambda$, where λ is the free-space wavelength of the incident light.

To facilitate comparison of different geometries, it is useful to express the scattering cross sections in terms of efficiency. By normalising to the geometrical cross section, we obtain the scattering and extinction efficiency, $Q_{\rm sca}$ and $Q_{\rm ext}$. The extinction efficiency is plotted in Figure 1.1 for a gallium phosphide sphere with radius r=150 nm. The total efficiency is shown against the extinction efficiency associated with each of the first three scattering coefficients. Thus, the extinction and scattering spectra of a sphere can be broken down into individual modes. The resonant wavelengths are dependent on the size of the sphere, its refractive index and the refractive index of the surrounding medium. The same can be said for an infinite cylinder with a slight modification.

1.2.2 Scattering by an infinite cylinder

The theory applied to the sphere can be extended to an infinite right circular cylinder. However, an infinite structure would have an infinite extinction cross section. Thus, similar to the scattering efficiency defined above for the sphere, it is meaningful to define the scattering or extinction per unit length rather than an exact cross section. The structure has reduced symmetry, so new a and b coefficients need to be defined. There are two possible polarisations that require solutions; the electric field of the incoming light can either be polarised parallel to the axis of the cylinder or perpendicular, which we define as transverse magnetic (TM) and transverse electric (TE), respectively. Any angles in between are found through a superposition of solutions to both cases. This doubles the number of required coefficients, splitting them into a_{ll} and b_{ll} for TM polarisation, and



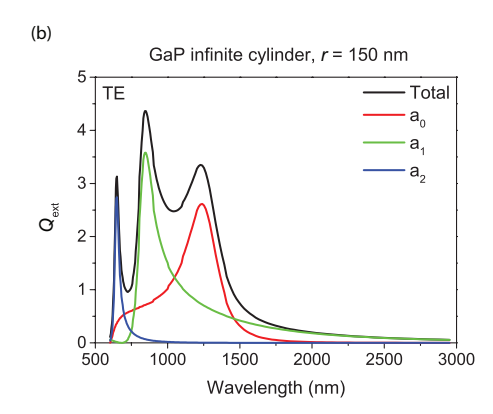


Figure 1.2: Extinction efficiencies for an infinite cylinder of GaP with radius r=150 nm for (a) TM and (b) TE polarisation. Within the spectra, individual resonances can be identified which are associated with the individual scattering coefficients. The first three resonances $(l=0,\,1,\,2)$ are shown for each polarisation.

 $a_{l\text{II}}$ and $b_{l\text{II}}$ for TE polarisation. These coefficients are comprised of cylindrical functions rather than spherical functions. Thus, the overall structure of the solution remains the same, with electrical and magnetic eigenmodes, but the functions change.

The case of light incident perpendicular to the axis of the cylinder (defined as the angle $\zeta = 90^{\circ}$) is a special case, as it greatly simplifies the possible solutions. This is because the definitions of both a_{lI} and b_{lII} are proportional to the cosine of ζ . Therefore, for perpendicular illumination, these coefficients are reduced to zero, leaving b_{lI} and a_{lII} . The solutions, then, for parallel electric field are comprised only of magnetic modes, while the solutions for perpendicular electric field are purely electric modes.

The scattering and extinction efficiencies at normal incidence, are defined by reduced versions of Equations 8.36 and 8.37 in [44]. For TM polarisation the equations are

$$Q_{\text{sca,I}} = \frac{2}{x} \left[|b_{0I}|^2 + 2 \sum_{l=1}^{\infty} |b_{lI}|^2 \right], \tag{1.3}$$

$$Q_{\text{ext,I}} = \frac{2}{x} \text{Re} \left\{ b_{0\text{I}} + 2 \sum_{l=1}^{\infty} b_{l\text{I}} \right\},$$
 (1.4)

and for TE polarisations the equations are

$$Q_{\text{sca,II}} = \frac{2}{x} \left[|a_{\text{0II}}|^2 + 2 \sum_{l=1}^{\infty} |a_{l\text{II}}|^2 \right], \tag{1.5}$$

$$Q_{\text{ext,II}} = \frac{2}{x} \text{Re} \left\{ a_{\text{0II}} + 2 \sum_{l=1}^{\infty} a_{l\text{II}} \right\}.$$
 (1.6)

The extinction efficiencies for TM and TE polarisation are plotted in Figure 1.2 for an infinite cylinder of gallium phosphide with radius r = 150 nm. As with the sphere, the

total extinction efficiency is shown against the extinction associated with each of the scattering coefficients.

The multipolar field analogy breaks down for the infinite cylinder, as is evident from the presence of l=0 modes. Instead, these modes demonstrate similar transverse excitiation to waveguide modes; b_{lI} resembling TM_{l1} and a_{lII} resembling TE_{l1} modes. This will be expanded on in Chapter 3.

1.3 Resonances of metallic nanoparticles

In many respects, a metal nanoparticle behaves much more like a traditional antenna than a semiconductor nanowire. The main reason for this analogy is that both radio and plasmonic antennas rely on materials with a negative permittivity. However, this analogy is only superficial. In the radiowave regime the metals used behave as perfect electrical conductors and fields do not penetrate inside the antenna structure resulting only in surface currents. At optical frequencies, the finite permittivity results in significant penetration of fields, and thus a volume current [45]. Optical antennas are in fact resonators for surface plasmons, which can take one of two forms. In this case we deal with localised surface plasmon resonances, where the coherent oscillation of the electron cloud is confined by the nanoparticle size. Plasmon resonances can also take the form of surface plasmon polaritons (SPPs) which travel along the metal-dielectric interface. Coupling of free-space light into a SPP typically requires phase matching through use of a coupling medium, such as a prism or grating, as a free-space photon will have less momentum than the SPP.

An antenna is a resonant device, meaning that its length is determined by the wavelength for which it is to be used. In the case of TV and radio antennas this is on the order of meters, while the optical and near-infrared wavelengths are much, much smaller. Hence, optical antennas need to be only hundreds of nanometers in length. The resonance condition is given by the simple equation: $L = l\lambda/2n$, where n is the refractive index of the surrounding medium and l is the mode order. This equation assumes perfect conductivity and complete reflection of electromagenetic radiation from the metal surface, however. For macroscopic antennas any radiation penetration is negligile compared to the wavelength, but on the nanoscale this no longer holds true. This results in the required length of the nanoantenna being much shorter than half the resonant wavelength. The precise relation is dependent on the material properties and geometry [46].

The nanoantennas used in this work have a width of comparable size to their length. This results in the devices having a resonance associated with their width as well as their length. Although the results in Chapter 5 are measured along the nanoantennas

longitudinal direction, it is worth noting that these devices have another shorter resonance in the transverse direction. As mentioned earlier, the exact resonant wavelength is dependent not only on the properties of the antenna but also the surrounding medium. This is what makes nanoantennas useful for nanoscale sensing applications.

1.4 Thesis outline

This thesis contains a total of seven chapters. Following this introduction, Chapter 2 will provide an overview of the various techniques used throughout this work. These are split up into simulation, fabrication and measurement techniques. The simulation of light-matter interactions is performed by numerically solving Maxwell's equations using the Boundary Element and Finite Element Methods. Next, the preparation of experimental samples is described focusing on the growth and milling of semiconductor nanorods and the deposition of gold nanorods via electron-beam lithography. Finally, we look at the experimental techniques of dark field, spatial modulation and pump-probe spectroscopy.

Chapter 3 examines the interaction of light with a low aspect ratio semiconductor nanorod. The Boundary Element Method is used to simulate a polarised plane wave incident on a free-standing cylindrical structure with hemispherical end facets. The evolution of the extinction spectrum with length is investigated in detail and the electric and magnetic near field distributions are used to identify the nature of the various modes. The enhancement at the center of a dimer structure is investigated to determine the potential of semiconductor nanorods as a low loss alternative to plasmonic structures. The angular dependence of the nanorod response is also investigated for its suitability for real world applications.

In Chapter 4, we measure experimentally the scattering and extinction of a nanorod on a substrate using dark field and spatial modulation spectroscopy techniques. The simulation does not take into account a number of parameters introduced by the experimental set-up. As a result, there are a number of differences between the measured and simulated spectra. Careful examination of the experimental results in conjunction with further simulations reveals more about the nature of the interaction between the incident light and the nanorods on the substrate.

Chapter 5 moves on to examine how a phase change material, vanadium dioxide (VO₂), influences the measured spectra of gold nanorod structures. The VO₂ phase change is triggered by either heating up a copper plate which the sample is mounted on, or by pumping with a second laser source. Spatial modulation is used to measure how the phase change effects the nanorod's extinction spectrum. Further experiments modify the power of the pump laser to investigate if the transition is continuous, allowing an observed resonance shift to be tuned. In addition, the picosecond time response of the

 VO_2 film is measured to see if the presence of the gold nanorod modifies the phase transition.

In Chapter 6, gold nanoantennas depositied on top of a silicon-on-insulator (SOI) waveguide device are investigated in an attempt to make an all-optical modulator. The device is designed such that two paths interfere and create a standing wave inside a racetrack resonator. The presence of the resonator means that only select wavelengths are transmitted through the device. The gold nanoantenna is positioned at the center of the resonator such that it sits on top of an antinode for all odd harmonics, acting as a coherent absorber. The transmission spectrum through the waveguide is measured before and after the nanoantennas are deposited. When no appreciable difference is measured, the set-up is modified to improve the signal and elimate as much measurement error as possible.

Finally, Chapter 7 summarises the work layed out in this thesis and looks at further work that may improve on the results presented. As is often the case with experimental research, a number of the results were not as expected, indicating that a different approach may be needed in order for this work to move forward.

Chapter 2

Methodology: Simulation, Fabrication, and Measurement Techniques

In this chapter, we take a look at the various techniques used during the research detailed in this thesis. These techniques fall into three categories; simulation, sample fabrication and nanoantenna characterisation. The numerical work presented in the following chapter is performed using the Boundary Element Method (BEM). The calculations are performed using a C++ code provided by J. Aizpurua of the Donostia International Physics Center and Centro de Fisica de Materiales. The code was run on the University of Southampton's high performance computing cluster, Iridis. The other simulation technique, used to examine experimental results, is the Finite Element Method (FEM), performed using Comsol Multiphysics.

Numerous fabrication techniques were used in the preparation of our different samples. This section is split to cover separately the fabrication of GaP nanorod samples, gold nanorod samples and thin-film oxides. For the GaP nanorods, vertical wires were grown, via a chemical vapour deposition (CVD) technique by S. Assali and E. Bakkers at the Eindhoven University of Technology. These were then pressed on to a glass chip, which had been prepared by depositing a chromium marker grid and a thin (20 nm) film of indium tin oxide (ITO). The marker grid, deposited by Y. Wang using photomask lithography, provides reference points to aid in finding appropriate nanowires under SEM and in the optical set-up. The ITO film, deposited by myself using radio frequency (r.f.) sputtering, provides a mildly conductive layer to allow SEM imaging without charge build-up on the substrate. The VO₂ film was prepared by J. Gaskell and D. Sheel of the University of Salford. Gold nanorods were deposited on top of this sample by Y. Wang, using electron beam lithography.

The characterisation techniques include dark field and spatial modulation microscopy and pump-probe spectroscopy. All of the experimental set-ups make use of a Fianium supercontinuum laser. By passing a picosecond scale laser pulse (seed wavelength 1060 nm) through a photonic-crystal fibre, a broadband source is produced ranging from 400 nm to 2300 nm wavelength.

2.1 Simulation

Numerical simulation programs are invaluable to this project. If an experiment can be simplified to a simple model, it is possible to explore a vast range of design parameters with relative ease. From this, it is possible to get a detailed picture of the physics taking place, which aids in selecting some optimum design features to be fabricated for experimental work.

Light travels as an electromagnetic wave. The behaviour of light is thus governed by Maxwell's equations:

$$\nabla \cdot \vec{E} = \frac{\rho}{\epsilon_0},$$

$$\nabla \cdot \vec{B} = 0,$$

$$\nabla \times \vec{E} = -\frac{\partial \vec{B}}{\partial t},$$

$$\nabla \times \vec{B} = \mu_0 \vec{J} + \mu_0 \epsilon_0 \frac{\partial \vec{E}}{\partial t}.$$

The modelling techniques used in this work function by solving these equations in either differential form, as shown above, or in integral form obtained using the divergence and Stokes' theorems.

2.1.1 Boundary Element Method (BEM)

The Boundary Element Method is a technique for solving systems of linear partial differential equations in integral form. By applying this to Maxwell's equations, we can simulate a light wave incident on a nanoparticle. The geometry is divided into domains of homogeneous material. The boundaries between these domains are then discretised. At the points along the boundary, the surface charge density and surface current produced by the incident radiation is calculated, from which far field and near field properties can be found.

An advantage to BEM over other methods is that the system does not need an external boundary. In this way, any waves that are scattered away from the geometry under investigation are lost, making the simulation of an infinite domain possible. This is ideal for the simulation of isolated nanoparticles as any external domain is far, far greater than the geometry under investigation.

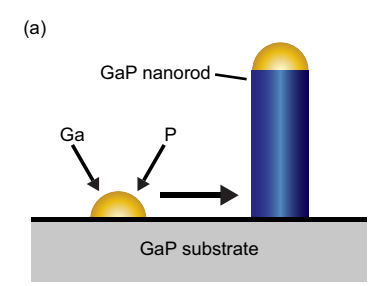
The code uses a 2D axisymmetric geometry making it ideal for cylindrical or spherical structures and, as such, provides a great platform for the initial investigation of such a structure. However, this method does not allow for the inclusion of a substrate and limits the antenna structures that can be investigated. Moving to more complex antenna geometries would require a more versatile program.

2.1.2 Finite Element Method (FEM)

Like the Boundary Element Method, the Finite Element Method is also a technique for solving partial differential equations. In the case of FEM, the entire volume of the defined geometry is discretised into sub-domains forming a mesh of small volume elements. The size of these elements can vary, smaller elements producing a finer mesh. A balance must be found between having a mesh fine enough as to produce an accurate answer but coarse enough so as not to take an unecessarily long time to solve.

The Comsol software, used to perform the FEM calculations, provides a variety of preprogrammed conditions. The disadvantage to volume meshing is that the external boundaries of the geometry need to be defined which, if not treated properly, can lead to unwanted back reflections in the system. There are several ways to handle this. The most complete solution is a Perfectly Matched Layer (PML) domain. The name is derived from the matching of the material properties as closely as possible to the adjacent domain while increasing the absorption, thus creating an absorbing external boundary with close to zero reflection. Surrounding the geometry in PMLs can require a large amount of memory, however.

Rather than using absorbing boundary conditions, highly reflective boundary conditions and periodic boundary conditions can be used to take advantage of symmetries in the geometry. Periodic boundary conditions effectively transfer radiation incident on an external boundary to a paired boundary, usually found on the opposite side of the geometry. This can also be achieved using reflective boundary conditions if the strucutre has a mirror symmetry. In this case, it is possible to reduce the simulation volume by simulating only half of the geometry for each symmetry plane. For electromagnetic radiation, the reflecting boundaries are provided by the mathematical formulations for perfect electric conductors (PEC) and perfect magnetic conductors (PMC). Electric (magnetic) fields incident perpendicular to the PEC (PMC) boundary condition are completely reflected. It is worth noting, however, that this an approximation that should only be used for particularly computer intensive calculations. The PEC and PMC demonstrate reduced reflection when diverging from the case of perpendicular incidence, which may result in errors in the solution.



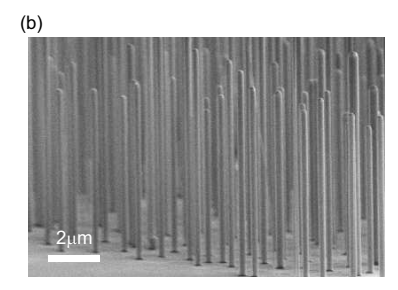


Figure 2.1: (a) The growth process of a GaP nanowire. Gallium and phosphur vapours are absorbed by a gold particle and are deposited below, resulting in the growth of a crystaline pillar. (b) An angled SEM of the resulting nanowires.

2.2 Fabrication

The samples used in this thesis were produced using a number of techniques, depending on the required results. This section gives an overview of the techniques used in the production of both semiconductor and metal nanoantennas as well as the thin films on which they were deposited.

2.2.1 MOVPE growth and FIB milling

To achieve a well defined structure and constant diameter, nanowires were grown by the group of Prof. Erik Bakkers from the Eindhoven University of Technology using Metal-organic Vapour Phase Epitaxy (MOVPE). The process has been illustrated in Figure 2.1. The nanowires are grown vertically on a GaP substrate using a catalytic growth process known as vapour-liquid-solid (VLS) growth, whereby the metal-organic compounds (such as tri-methyl gallium) are selectively decomposed at a gold nanoparticle catalyst. The gallium and phosphorus are dissolved into the droplet and form an eutectic alloy. Precipitation of material at the nanoparticle-substrate interface results in epitaxial growth of a crystalline nanowire with the nanoparticle resting on the top. The growth mode can be switched from catalytic VLS to uniform growth on all surfaces by increasing the temperature of the reactor.

The vertically grown nanowires were mechanically pressed on to a glass slide to deposit a number of nanowires horizontally on its surface. To produce the desired nanoantenna structures, the nanowires were milled using a focused ion beam (FIB). This is an ablation technique whereby charged ions (typically gallium) are accelerated towards the sample with a high energy and result in the ejection of material from the surface. This allows nanorods to be milled to specific lengths and dimers to be created by milling a small gap in the middle. The size of the gap is approximately 40 nm wide.

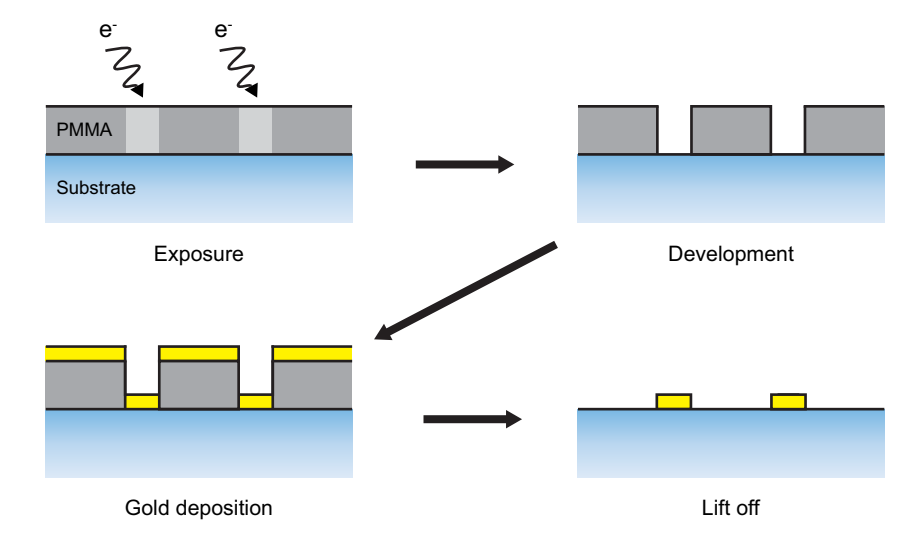


Figure 2.2: Stage by stage deposition of gold nanoantennas by e-beam lithography. A layer of PMMA resist is exposed by an electron beam and then developed in a solution, removing the exposed areas. A layer of gold is deposited on top and then the layer of PMMA is disolved in acetone, leaving gold nanorods.

2.2.2 Electron-beam lithography and gold deposition

The gold nanoantennas used in the later chapters of this thesis were deposited using electron beam (e-beam) lithography. The process uses a positive resist to produce holes in the shape of the desired nanoantennas. In the simplest case, a single layer of resist such as PMMA is deposited on a substrate by spin-coating, producing a thin layer of uniform thickness. The desired structure is then "drawn" in the photoresist using a focused beam of electrons. Exposure to the e-beam breaks the links of the hydrocarbon chain making the exposed areas susceptible to being dissolved by a developer fluid, typically MIBK.

Once the exposed resist has been developed, a layer of gold is deposited using a physical vapour deposition technique; either evaporation or sputtering. With the gold deposited, the rest of the resist layer can be dissolved using acetone. This leaves gold only in the locations where the resist was exposed by the e-beam. A thin (5-10 nm) adhesion layer such as chromium is often included as gold does not typically adhere to glass very well which can result in the nanostructures being removed with the rest of the gold layer. The process has been illustrated in Figure 2.2.

The resolution of this process can be limited by deposition of gold on the side of the resist layer which connects the desired nanostructure with the gold layer on top of the resist. This can result in fine nanostructures being removed with the e-beam resist. To improve the resolution, a bilayer of PMMA on top of MMA can be used. In the development process, the MMA is dissolved faster than the unexposed PMMA producing an undercut. If the MMA layer is suitably thick, the gold deposited in the exposed area is completely

isolated from the rest of the gold film ensuring that the desired nanostructures stay in place.

2.2.3 Thin-film oxide deposition

In addition to the nanoantennas, a number of the samples make use of a thin oxide film. The properties of the oxide films vary depending on a number of variables in the deposition process. These can include temperature, relative gas flow pressures and the substrate onto which the film is deposited. Here we detail the deposition of a film of indium tin oxide (ITO) and vanadium dioxide (VO_2).

For the GaP nanorod samples, a transparent conductive layer of ITO was deposited on top of a square glass chip as a base on which to deposit the GaP nanorods. Insulating samples can be problematic to image under SEM. The incident electron beam can result in a build up of charge on the dielectric surface which then distorts the image. The effect can result in image drift or even saturation. The ITO film counteracts this by acting as a mildly conducting layer, preventing any significant charge build-up.

The ITO layer is deposited using r.f. sputtering. An ITO disc, called a target, is bombarded with a high pressure jet of argon ions. This results in the ejection of material from the target towards the substrate. The use of strong electromagnetic fields confines the plasma close to the surface of the target, increasing the deposition rate, and also trapping any charged particles ejected from the target, ensuring that the deposited material is neutral. While highly conductive ITO films can be produced, the layer need only be mildly conductive. To achieve this, a small amount of oxygen is included in the argon jet and the sputtering is performed without any additional heating (the process itself is a source of heat and the chamber will reach a temperature around 60° over the course of the depostion).

In Chapter 5, gold nanoantennas are deposited on top of a layer of VO₂ to investigate the possibility of antenna switching. More information on the properties of VO₂ can be found in said chapter; for now we describe the deposition process. The VO₂ layer used is a high quality film produced in collaboration with D. Sheel and H. Yates from the University of Salford [47]. To ensure a smooth film with the required transition temperature, a precursor layer of fluorine doped tin oxide (FTO) was used. Both were deposited using atmospheric pressure chemical vapour deposition (APCVD).

As the name suggests, precursor chemicals are passed over the substrate as vapours under atmospheric pressure. These vapours react and deposit the desired material on top of the substrate. To prevent unwanted oxidation of the films, the system was first purged with nitrogen gas. For the FTO layer, the reactants were monobutyltin trichloride (MBTC), trifluoroacetic acid (TFAA) and water. The deposition was performed at 600 °C. The reactants were then purged from the system and replaced with vanadium(IV) chloride

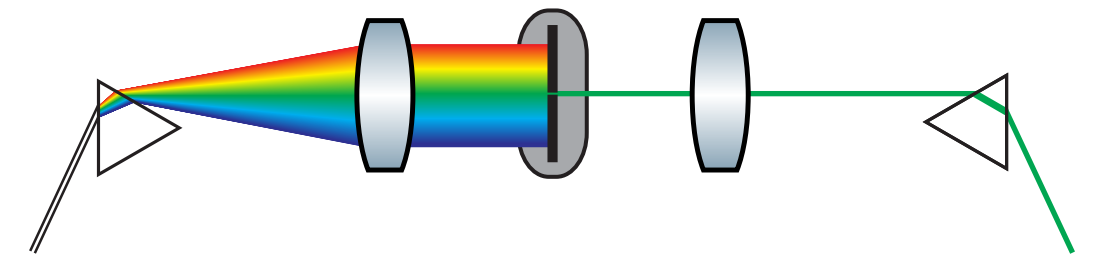


Figure 2.3: Illustration of a monochromator. The super-continuum source is passed through a glass prism resulting in the spatial separation of the composite wavelengths. This is collimated and then filtered by a thin slit which can be moved via a motorised stage, effectively selecting a single wavelength. The light is then refocused and passed through a second prism to recombine all wavelengths into a single beam path.

 (VCl_4) and water. This deposition was performed at 375 °C. The resulting film has a surface roughness of <10 nm and shows a thermochromic transition around 68 °C.

2.3 Spectroscopic characterisation

This section comprises the measurement techniques used to spectrally characterise our nanoantennas. To measure the particle's scattering spectrum we use dark field spectroscopy, and to measure the particle's extinction spectrum we use spatial modulation spectroscopy. A pump-probe technique is also employed to optically induce a material transition in a VO_2 film. In this section we describe the concept behind each measurement technique. Experimental set-ups will be described in their respective chapters.

The laser source for each set-up is a Fianium supercontinuum pulsed laser. The pulse duration is approximately 11 ps and the repetition rate can be modified between 100 kHz and 20MHz by an internal pulse picker. The output from the laser is broadband light generated by passing a near-infrared seed laser through a photonic-crystal fibre, producing light ranging from 400 nm to 2300 nm.

For spatial modulation this laser source is directed through a double-prism subtractive mode monochromator, shown diagramatically in Figure 2.3. The light is dispersed by the first prism, collimated and then incident onto a 100 μ m slit, allowing light of only a selected narrow bandwidth (typically 2.5% of the central wavelength) through. The transmitted light is then refocused, after which it passes through the second prism, thus recombining the varying spectral components into a single beam path. Translation of the slit across the spectrum via a motorised stage allows the source wavelength to be selected and varied remotely.

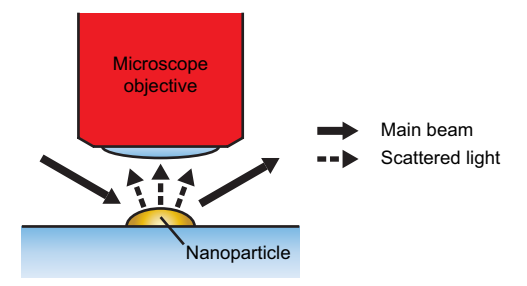


Figure 2.4: A simple dark field microscopy set-up. The light source is incident at an angle large enough such that the reflected beam does not enter the imaging objective.

2.3.1 Dark field spectroscopy

Dark field microscopy is a useful technique for imaging nanoscale particles by taking advantage of their highly scattering nature. By using a light source that is incident at a large angle in conjunction with a low numerical aperture imaging system, it is possible to detect only the scattered light. A simple set-up is illustrated in Figure 2.4. The result is an image of bright particles on a dark background. Both metal and dielectric particles both have scattering cross sections many times their geometrical cross section, allowing this technique to overcome the limits of optical resolution.

Using a dark field imaging system in conjunction with a spectrometer allows us to measure the scattering spectrum of the nanoparticle. A single particle can be isolated with a spatial filter, such as a confocal pinhole aperture. Comparing this scattering spectrum with a broadband scatterer reveals information about the particles scattering cross section, $\sigma_{sca}(\lambda)$.

Dark field spectroscopy is a highly sensitive technique as it is essentially background free, the only source of background being ambient lighting which can easily be controlled or removed. The technique also allows the separation of scattering from absorption effects. However, due to a limited aperture, we are only able to capture light scattered in a small cone from the nanoparticle at roughly 70° to the incident beam. Compared to spatial modulation, dark field measurements benefit from a well defined angle of incidence which allows for the selection of specific resonance conditions.

2.3.2 Spatial modulation spectroscopy

Spatial modulation is a technique with which one can characterise the linear response of a particle as small as 5 nm. The particle is moved rapidly with respect to the beam focus, as seen in Figure 4.8, and a lock-in amplifier allows the change in reflection or transmission caused by the presence of the particle to be measured directly. By varying the wavelength of incident light, we are thus able to measure a signal directly related to the particle's extinction cross section, $\sigma_{ext}(\lambda)$.

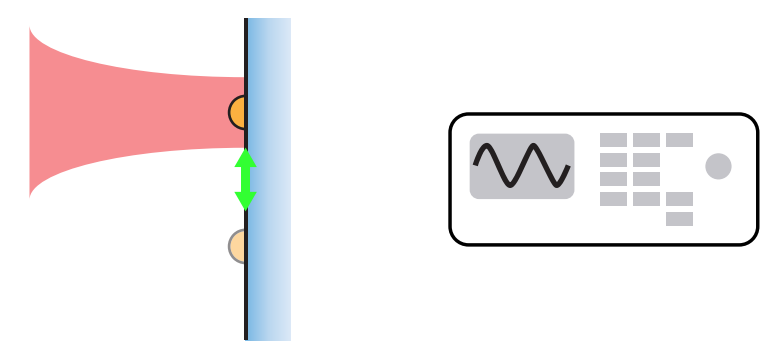


Figure 2.5: The principle of the spatial modulation technique. The position of the particle is moved rapidly with respect to the focal position producing a modulated signal that can be detected by a lock-in amplifier.

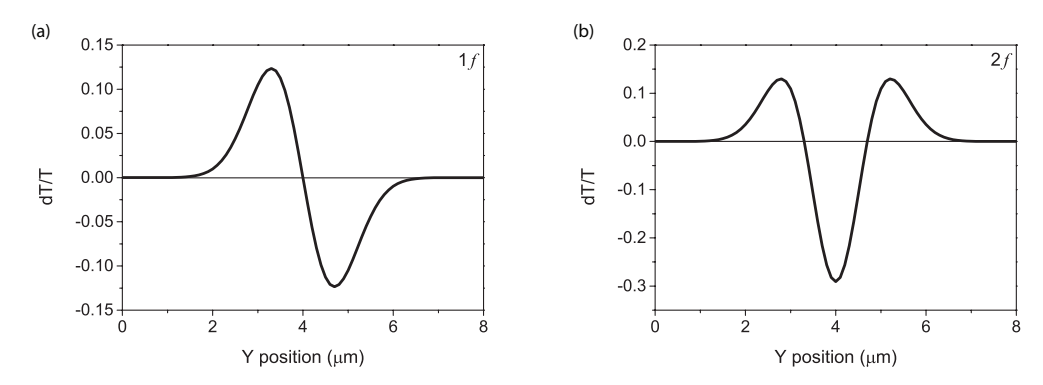


Figure 2.6: Calculated examples of position scans measured with the spatial modulation set-up at the 1f and 2f frequencies, based on a fit to experimental data.

The lock-in amplifier allows the differential signal to be measured at its fundamental frequency (1f), or higher harmonics (e.g. 2f). Typical scans in the direction of modulation are shown in Figure 2.6. The resultant profiles for the 1f and 2f signals take the form of the 1st and 2nd derivatives, respectively, of a Gaussian profile. This illustrates why the 2f signal is used for spectral measurements; to centre the particle in the beam simply requires maximising the measured signal rather than looking for a null-point. The peak of this signal is representative of the extinction cross section.

Spatial modulation is clearly a powerful tool for measuring a particles extinction spectrum in a non-invasive way, unlike SNOM (scanning near field microscopy) for example. Measurements taken in reflection are typically better than those taken in transmission due to reduced background light from most substrates. This gives a better signal to noise ratio, however, the process is flawed for samples that show strong directional scattering. As will be seen later, a particle that demonstrates preferential back scattering, for example, can make the measurement harder to interpret, demonstrating both increases and decreases to the reflected light, depending on the wavelength.

Compared to dark field spectroscopy, spatial modulation allows measuring cross sections of different segments of a nanowire along its length. However, the angle of incidence is

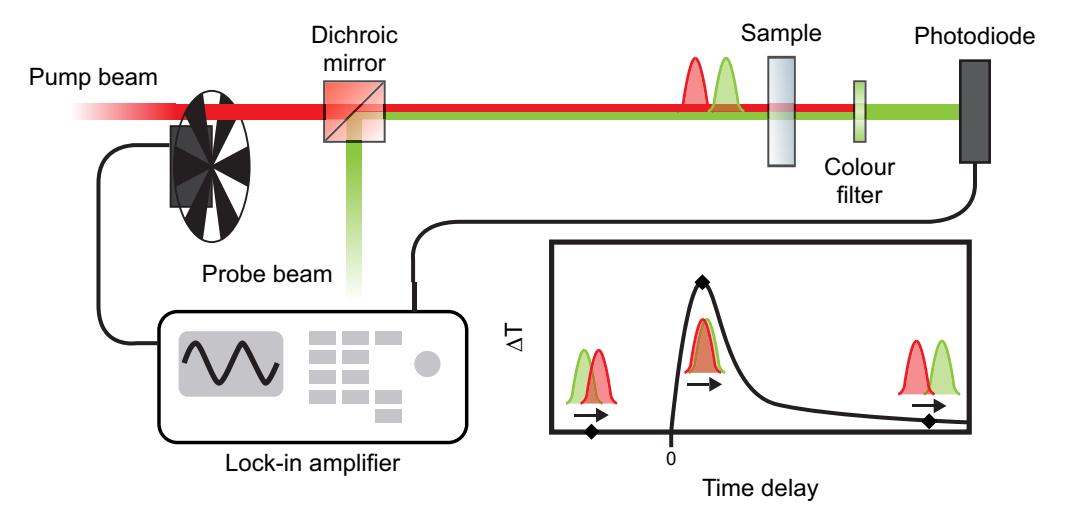


Figure 2.7: The principle of the pump-probe measurement. Two synchronised pulsed sources are directed at a sample such that the pulses arrive at the same spot close in time. One pulse is the pump, which should put the sample into some excited state. The other is the probe, which measures some property of the sample, such as the transmission. The pump pulse is filtered out before it reaches the measurement device. By modulating the pump beam and measuring the probe beam, we can study how the sample is affected. The inset demonstrates how changing the relative arrival of the pulses allows us to study how the effect of the pump evolves with time.

very broad as it is given by the numerical aperture of the objective used. Unlike dark field, the spacial modutlation technique is sensitive both to absorption and scattering cross sections.

2.3.3 Pump-probe spectroscopy

For nonlinear characterisation, we employ a picosecond pump-probe measurement technique. This requires two synchronised laser pulses to be incident on the same point of the sample and to be closely spaced in time. One laser is the probe pulse, used to measure a property of the system, and the other is a pump pulse, used to effect some nonlinear response. In order to measure this response, the pump pulse needs to be filtered from the detection system, usually by spectral filtering. In this way, a modification of the probe signal, as caused by the pump pulse, can be detected. A schematic is provided in Figure 2.7.

Information on how the system evolves with time can be extracted by varying the relative arrivals of the pump and probe pulse. This is achieved by including a delay line in one of the beam paths; a linear stage with a retroreflector that changes the path length without effecting the beam position on the sample. Having the pump arrive first allows us to measure how the modification by the pump develops and how quickly the material responds, as is illustrated in the inset of Figure 2.7. Having the probe pulse arrive first

allows for lifetime measurements to be taken, investigating how long the probe pulse is contained within the device.

In this thesis, pump-probe measurements are used to induce a thermochromic transition in a VO_2 film. The technique is combined with spatial modulation to detect how the change in the film affects the response of a gold nanoantenna. The temporal response of the VO_2 film can be measured with a resolution of tens of picoseconds. A better resolution would require a shorter pulse length.

Chapter 3

Antenna Resonances in Low Aspect Ratio Semiconductor Nanorods

3.1 Introduction

Semiconductor nanowires form an important building block for nanophotonic devices, as their growth is well controlled using a variety of top-down and bottom-up techniques [48, 49]. Not only that but semiconductors typically show very little absorption in the visible and near-infrared regions of the electromagnetic spectrum. This makes them a potential alternative to plasmonic devices, which can be inherently lossy. The movement of electrons within a plasmonic device results in greater absorption than most dielectric devices, as heat is generated through electron-electron interactions.

The quasi-one dimensional geometry of a nanowire enables their use as antennas and cavities for light [50–57], and offers many advantages for applications such as photodetectors [11, 12, 58–60], solar cells [6, 7, 61], and single photon sources [21]. Optimization of such devices requires knowledge of the nanostructured materials at a more fundamental level. For nanowires, the presence of guided and leaky mode resonances has been shown to result in strong light trapping phenomena and scattering of incident light [12, 60, 62–64]. A resonant nanowire mode can also be designed to form an effective cavity for spontaneous emission and lasing [21, 48, 65].

As mentioned in Chapter 1, there are two limiting cases that are particularly well understood. The surface modes of the sphere and the infinite cylinder are well expressed by analytical models. The modes present in the dielectric sphere arise from multipolar electric and magnetic excitations within the nanoparticle. The lowest energy modes observed in the far field are, thus, primarily the result of the magnetic dipolar resonance

and the electric dipolar resonance, followed by the magnetic quadrupolar resonance and so on. Similarly, the modes present in the infinite cylinder can be associated with a resonance of the transverse field, typically referred to as TM_{lm} or TE_{lm} modes. Recent years have seen a renewed interest in the lowest-order modes of submicron dielectric resonators for their potential to enhance magneto-electric light-matter interactions [57, 66–70], to induce exotic scattering properties of their solutions [71, 72] or as building blocks for dielectric metasurfaces [73–76].

Much work has also been done on the transverse modes of long (semi-infinite) nanowire structures. Of particular interest are the nanoantenna properties of these devices for light harvesting [12, 13, 62] and directional emission [77]. The polarisation dependence of the scattering and absorption efficiencies of infinite wires was investigated by Brönstrup et al. [78]. Evidence of the role of longitudinal cavity modes and optical antenna effects and their relation to photon confinement within the wire was investigated in several works related to enhancement of Raman scattering [79, 80] and to realisations of photonic and plasmonic lasing [81, 82]. Recently, the relation between Mie resonances and leaky modes was numerically investigated in the limit of optically thin nanowires [83]. It was determined that cylindrical Mie resonances and leaky mode solutions are yielded by formally equivalent formulas. For finite nanowires, the extinction spectra are dominated by Mie resonances for perpendicular and oblique incidence, while leaky/guided modes are prevalent at grazing incidence.

In most studies, the nanowire is modelled either as an infinite cylindrical waveguide supporting a number of radially guided or leaky modes, or as a one-dimensional Fabry-Pérot cavity. A general classification of radial and longitudinal modes and their interplay in nonspherical resonant structures was considered based on the ratio of the short to long axes [84]. Resonances of nanorods which have a length comparable to the diameter have been considered for specific geometries. Van de Groep et al. studied the effect of the height in cylindrical structures [85]. They observed a red-shift with longer cylinders for the magnetic dipole, electric dipole and magnetic quadrupole modes, which saturates as the height exceeds twice the diameter. Cai et al. established the profile for hybrid electromagnetic modes in nanodisk structures, and compared these to waveguiding modes [86]. Recently, Ee et al. investigated the dependence of the TM_{01} and TM_{11} waveguiding modes on the length of silicon nanoblocks under normally incident light [87]. They established that the TM_{01} mode is widely tuneable via changing the length of the nanoblock, whereas the resonant wavelength of the TM_{11} mode is mostly indepent of the nanoblock length.

In this chapter, we thoroughly investigate the interaction of low aspect ratio dielectric nanorods with an incident light wave using boundary element simulations. Despite recent efforts, a gap in the knowledge of mode scaling in finite-length nanowires still exists and a detailed analysis is of substantial interest for optimising devices and applications based on semiconductor nanowires. Using numerical calculations, we are able to address the

intermediate regime between Mie scattering and leaky mode resonances. Compared to the case of spherical nanoparticles, finite length nanorods offer additional degrees of freedom associated with the reduced symmetry and splitting of longitudinal and radial eigenmodes.

The nanorods are described as cylindrical particles with hemispherical end caps. The cylindrical geometry of a free-standing nanorod is chosen as a simplification of real crystalline nanowire morphologies and nanowires on a substrate, as it allows great simplification of calculations and provides an intuitive insight into the general behavior of modes. As an example of a high refractive index dielectric material, we consider gallium phosphide (GaP), although the models discussed here can be extended to any high-index dielectric such as silicon or cadmium telluride. By varying the length of the cylindrical rod segment, the continuous transition from a sphere towards an infinite cylindrical nanowire can be traced and addressed. This continuous transition is of particular interest as it reveals the direct relationship between the different magnetic and electric modes and their gradual transformation into mixed longitudinal and radial cavity modes. Compared to the relative simplicity of the two limiting cases, the mode structure at the intermediate regime is highly complex and is shown to consist of hybrid magneto-electric states combining longitudinal and radial resonant characters. Several features of the intermediate regime are identified, which are not present in either the case of the sphere or infinite cylinder. These hybrid resonances of dielectric nanowires may be exploited in the rational design of nanophotonic devices and metasurfaces.

3.2 Single nanorod simulations

The interaction of a semiconductor nanorod with an external light source is simulated using the boundary element method (BEM) [88, 89], allowing us to calculate both its far and near field response. Both the dielectric nanorods and the surrounding media are assumed to be homogeneous and the calculations do not take into account any nonlinear effects. While matierials like GaP can demonstrate a strong nonlinear response, this typically requires intense incident radiation. To include these effects would increase the complexity of the simultaiton and make the results more difficult to interpret. Thus, it is better to first understand the linear response of our devices.

Figure 3.1 shows a schematic of the geometry used: a cylindrical nanorod with hemispherical end caps, radius r and total length L. For the dielectric material of the nanowire we have chosen the high-index semiconductor GaP [90], as this material combines a very high refractive index of around 3.4 with a bandgap in the visible at a wavelength of 548 nm. The surrounding medium is set as air. Light is incident onto the nanorod as a plane wave polarised with the electric field oscillation either parallel

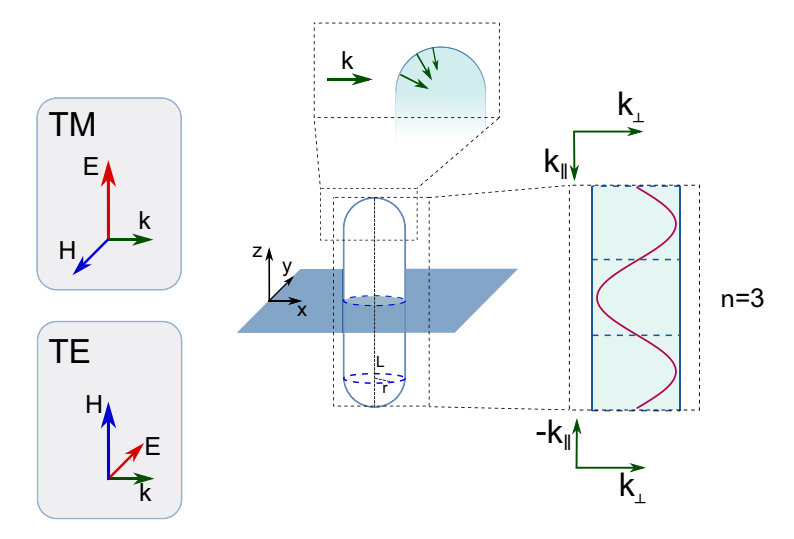


Figure 3.1: Schematic of the dielectric nanorod with normally incident TM or TE polarised illuminations. The nanorod is modeled as a cylinder with hemispherical caps of total length L and radius r. The endcaps provide a continous distribution of longitudinal wavevectors k_{\parallel} .

or perpendicular to the long axis of the rod, denoted as transverse magnetic (TM) and transverse electric (TE), respectively.

Extinction spectra of the nanowires were numerically calculated for a range of lengths from L=300 nm to L=1400 nm. The spectra were combined into the contour plots shown in Figures 3.2(a) and 3.2(b) for TM and TE illumination, respectively. A large number of modes are identified and are labeled on the basis of their near field profiles, as will be discussed in the next pages. Two distinct behaviours can be observed as the nanorod is made longer. Some modes, marked in red, show no variation in wavelength once the nanorod reaches a certain length. This length becomes shorter with higher mode orders. This set of modes is found to be equivalent to the infinite cylinder modes predicted by the extended Mie theory. Other modes continue to redshift beyond the parameter space investigated, but appear to still show an asymptotic behaviour. This set of modes can be divided further based on their near field profiles. As will be demonstrated later, these are cavity modes.

For the purposes of labeling these modes, two main types of resonances are identified, denoted as a_l^n and b_l^n , depending on the nature of the underlying electric and magnetic multipoles, in resemblance to the typical labels commonly used in Mie theory [44]. The spherical Mie modes are denoted as a_l^s and b_l^s respectively in Figures 3.2(a) and 3.2(b), for the case of L=300 nm. To determine the mode orders, we need to examine the electric and magnetic field distributions within the nanorod.

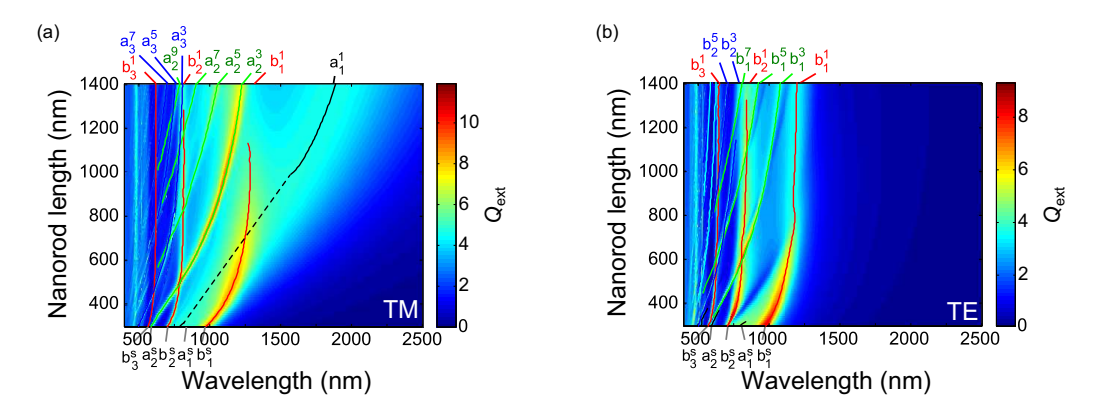


Figure 3.2: Maps showing calculated extinction efficiency, $Q_{\rm ext}$, obtained under (a) TM and (b) TE polarised light for a nanorod with a constant diameter of 300 nm and a length varied between 300 nm and 1400 nm.

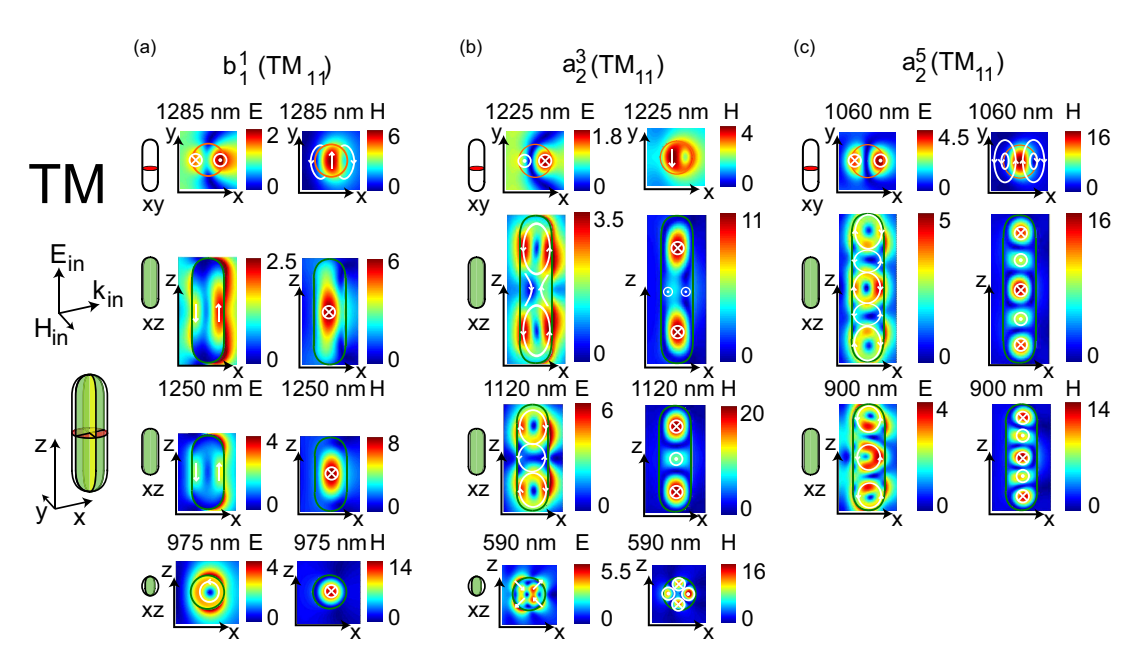


Figure 3.3: Evolution of the cylindrical mode b_1^1 and the first family of FP modes a_2^n under TM polarisation as the length is increased from 300 nm to 1400 nm. The number of nodes of the E- and H-fields in the z-direction are preserved as the length is increased.

3.2.1 Identification of nanorod modes from near field maps

In order to better understand the nature of the different modes and their evolution with the total length of the nanorod, we have analysed the near field maps of both the E- and H-field for particular values of the rod length, L. Figures 3.3 and 3.4 show a selection of these near field maps for TM and TE polarised light, respectively. The xy and xz maps show the cross section through the center of the scatterer. The xy-plane reveals the radial distribution, which can be directly compared to the waveguide theory for the infinite wire. The corresponding TE/TM resonances are shown in brackets for each of the mode families.

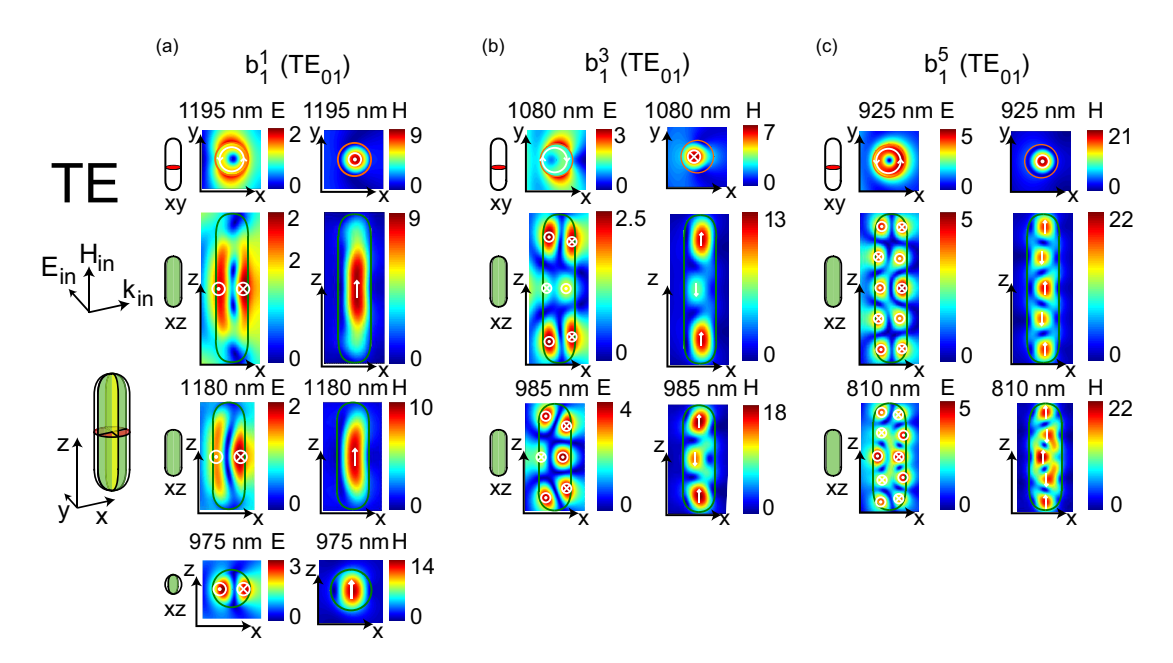


Figure 3.4: Evolution of the cylindrical mode b_1^1 and the first family of FP modes b_1^n under TE polarisation as the length is increased from 300 nm to 1400 nm. The number of nodes of the E- and H-fields in the z-direction are preserved as the length is increased.

In Figure 3.3, three modes are selected to illustrate the evolution of the cylindrical and cavity modes. At the top of each panel, the xy cross section shows roughly equivalent E-and H- field distributions for all modes. This distribution is typical of the TM_{11} waveguiding mode, with the electric field dominated by out-of-plane anti-parallel currents and the magnetic field exhibiting dipolar polarisation along the y-axis. In Figure 3.3(a) we look at the evolution of the b_1^1 mode. The near field maps of this mode reveal a central magnetic dipole along the y-axis for all the lengths considered. Due to this purely radial character of the mode, the resonant wavelength shows only a weak dependence on the length of the wire. In Figure 3.2(a), this mode can be traced back to the spherical particle where it becomes the b_1^s mode.

Figures 3.3(b) and 3.3(c) show the evolution of the electric-type cavity modes, a_2^3 and a_2^5 . Initially, these would appear to be of the same character as the b_1^1 mode as they are composed of a number of magnetic dipoles along the length of the nanorod, which are oriented in alternating directions along the y-axis. In addition, all three modes illustrated in Figure 3.3 converge to the TM_{11} waveguiding mode in the limit $L \to \infty$. However, the a_2^3 mode can be traced back to the spherical quadrupolar electric Mie mode, a_2^s . It is somewhat surprising that the excitations change their character from the electric a_2 to magnetic TM_{11} , but the near field maps reveal that as the sphere is elongated along the z-axis, the polarisation loops in the xz-plane rearrange, inducing the magnetic dipoles observed.

In Figure 3.4, we see three more exemplary modes. In this instance, all three modes

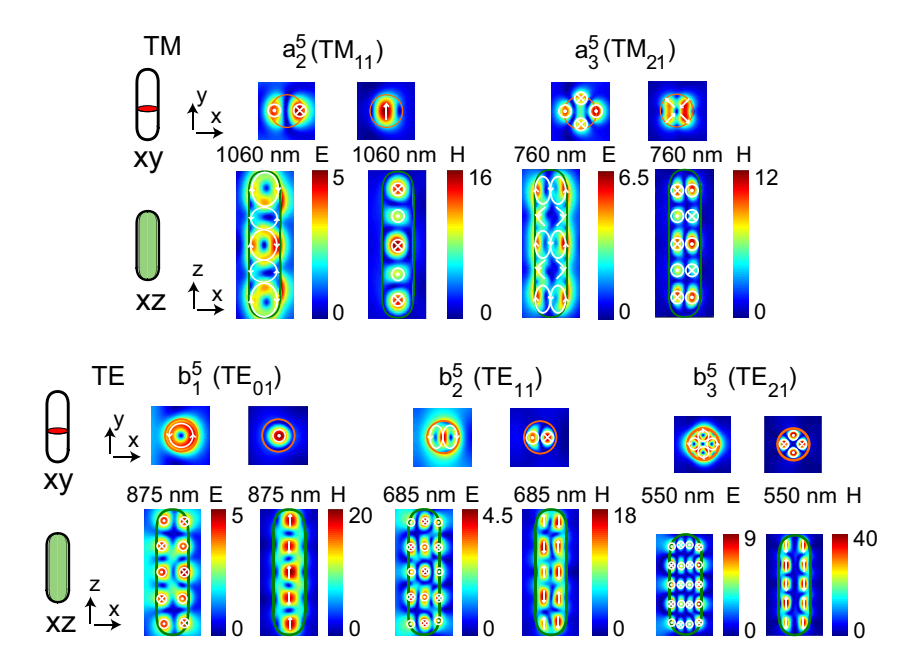


Figure 3.5: Examples of higher order TM and TE modes for n = 5. The a_2^5 and a_3^5 modes were calculated for a nanowire length of 1400 nm, the b_1^5 and b_2^5 for a nanowire length of 1200 nm and the b_3^5 for a length of 980 nm. The different dimensions are necessary due to the density of resonances for shorter wavelengths.

converge to the TE_{01} mode in the limit $L \to \infty$. This waveguiding mode is characterised by an electric current loop in the xy-plane, forming a magnetic dipole along the z-axis. These modes are identified as b_1^1 , b_1^3 and b_1^5 , based on the number of dipoles along the nanorod length. These are so named as both b_1^1 and b_1^3 can be traced back to the b_1^s spherical Mie mode. It is worth noting that we observe the presence of b_l^1 modes for both TE and TM polarisation. These modes are identical for both polarisations in a spherical particle except for the direction of electric and magnetic fields. These field orientations are retained when going to elongated nanowires, which eventually results in similar field profiles, but with different field orientations.

In the maps of extinction cross sections shown in Figure 3.2 we can identify numerous other modes converging towards higher order TM and TE modes. Examples of these modes are shown in Figure 3.5 for the case n=5. Careful selection of nanowire lengths was done to avoid spectral overlap of multiple modes. The higher order modes are characterised by more complex, multipolar transverse excitations, following the symmetry of the corresponding infinite wire leaky mode resonances, $TM_{(l-1)1}$ and TE_{l1} . The complexity of the mode spectrum and large spectral shift of these higher order modes with decreasing wire length prevents tracing them back to particular resonances of the Mie sphere, as could be done, for example, with the a_2^3 resonance. Given the strong spectral shift with reducing wire length for these higher order modes, it is clear that the higher order FP modes do not derive from spherical Mie modes of the same radial multipole order. A more complete catalogue of near field profiles can be found in the appendix.

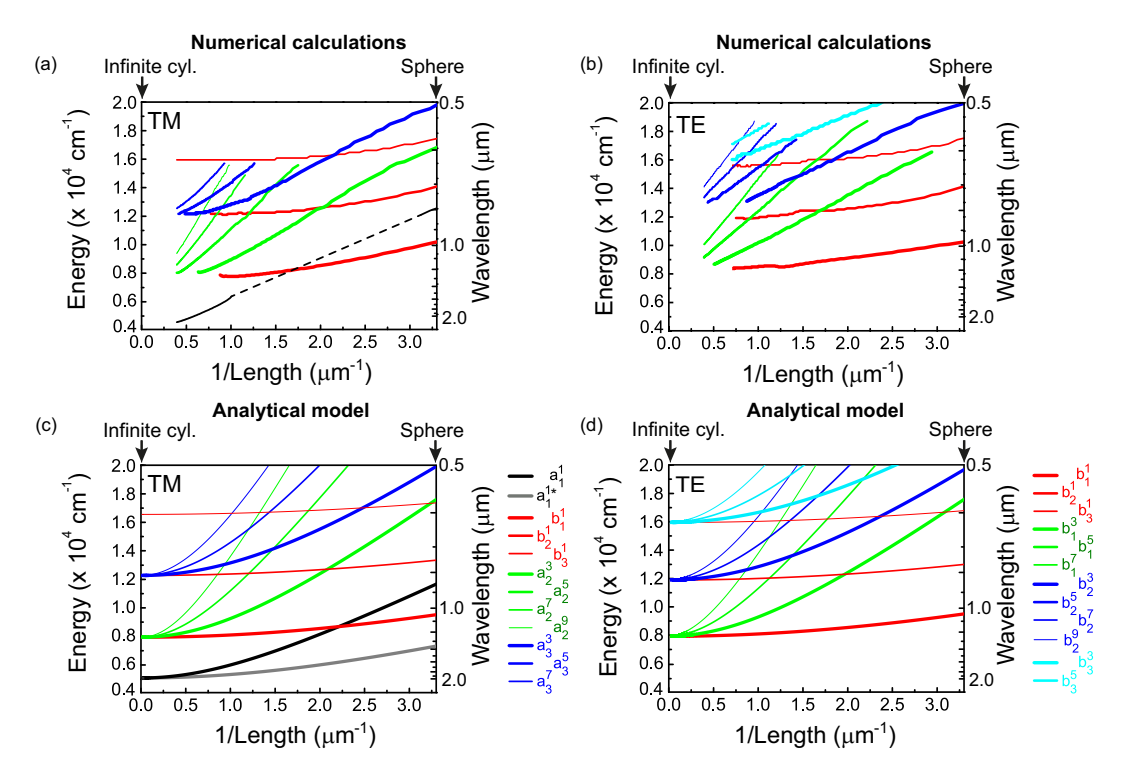


Figure 3.6: Resonance positions plotted as energy against reciprocal wire length 1/L. (a, b) Data extracted from the peaks in Figure 3.2 (c, d) Peak positions calculated by Equation 3.4.

To summarise what we have seen so far, the modes of the nanorod can be divided into two types of mode that are either electric (a_l^n) or magnetic (b_l^n) in nature. As the nanorod is made longer, this nature becomes more mixed and difficult to discern, particularly for the higher order modes. However, the lowest order of each set of modes (different l value) can be traced back to a spherical Mie resonance. For the case of the infinite cylindrical mode equivalent this is the n=1 mode, whereas for the cavity modes this is the n=3 mode. Having established the nature of the different resonances in the near field, we can now consider how this determines the resonant wavelength changes with the nanorod length, i.e. the dispersion relation of the resonances.

3.2.2 Scaling of modes with nanorod length

To get a better picture of how the different modes scale with length, the peak positions were extracted from Figure 3.2 and plotted in Figures 3.6(a) and 3.6(b) as a function of inverse length 1/L and energy $\propto 1/\lambda$. These dispersion plots reveal how the modes of the dielectric sphere evolve towards the modes of an infinite cylinder.

It was observed by M. Schmidt that the near field features are similar to those of a Fabry-Pérot (FP) resonator. To understand how the resonances shift with nanorod length, Schmidt developed an extended FP model, in which the energies of modes are given by a combination of the longitudinal and transverse components. The longitudinal

component is simply defined by the length of the nanorod, acting as a resonant cavity. For a one-dimensional FP cavity of length L, the longitudinal wavevector associated with the n^{th} order resonance is given by

$$k_{\parallel}^{n} = \frac{\pi n}{L}.\tag{3.1}$$

The longitudinal wavevector thus determines the resonant frequency of such oscillations through the relation

$$E^n = \frac{ck_{\parallel}^n}{m},\tag{3.2}$$

where m is the relative refractive index of the cavity medium. This longitudinal wavevector component is generally not present in the incident wave, but is introduced by diffraction of light at the finite wire length, i.e. through scattering of light at the tips of the nanorod as illustrated in the schematic in Figure 3.1.

It was demonstrated in Figure 3.5 that the resonances are differentiated based on not only the longitudinal field distribution but the transverse field distribution as well. To account for this, we can extend our simple one-dimensional model by introducing a second orthogonal mode order. To find the energy of these excitations, we return to the solutions of the infinite cylinder, calculated analytically using the extended Mie theory. The transverse wavevector is then given by

$$k_{\perp,l} = \frac{2\pi}{\lambda_l},\tag{3.3}$$

where λ_l is given by the resonant wavelength of the $a_{l \text{ II}}$ and $b_{l \text{ I}}$ 2D Mie coefficients (following the notation of Bohren and Huffman [44]), for the TE and TM polarisations, respectively.

The expression for the energy of the n^{th} Fabry-Pérot mode with l^{th} order transverse excitation thus becomes a simple combination of these orthogonal components:

$$\frac{E_l^n}{c} = \sqrt{k_{\perp,l}^2 + (k_{\parallel}^n)^2} = 2\pi \sqrt{\frac{1}{\lambda_l^2} + \left(\frac{n}{2Lm}\right)^2}.$$
 (3.4)

As illustrated in Figures 3.6(c) and 3.6(d), this formula predicts correctly the evolution with nanorod length of the lowest order modes highlighted in Figures 3.6(a) and 3.6(b). In particular, we show how each family of modes, b_l^1 , a_{l+1}^n , and b_l^n , converge towards the TM_{l1} and TE_{l1} waveguiding mode.

Earlier, it was determined that certain modes could be traced back to the Mie resonances of the spherical nanoparticles: the transverse electric (a_l^s) and magnetic (b_l^s) modes. This limit is not covered exactly by our extended Fabry-Pérot formalism, since the boundary conditions for the sphere and for a section of a cylindrical waveguide with perfectly

reflecting flat endcaps are very different. Thus, the numerical calculation deviates from the analytical model for short wires where the precise endcap morphology plays a role.

This shortcoming becomes particularly significant for the purely longitudinal electric mode TM_{01} , as illustrated in Figure 3.6(c), where the grey line (a_1^{1*}) shows the dispersion of the a_1^1 mode as calculated with Equation 3.4; clearly very different from the respective black line in Figure 3.6(a). This problem was previously considered for plasmonic nanorods [46] modelled as FP cavities, where TM_{01} is the dominant mode. To mimic the solution applied to the plasmonic system we can introduce an arbitrary phase pickup by the field due to the reflection from either of the ends of the nanorod. The resulting dispersion relation, shown in Figure 3.6(c) with the black line (a_1^1) , was obtained by assuming a π phase pickup at each reflection from the endcaps and shows a much better agreement with the numerical result. This arbitrary phase pickup is dependent on the transverse nature of the excitation, however, with the l=1 dipolar modes experiencing much larger phase change on reflection (π) than the higher order modes (l>1). Therefore, this correction has only been included for the transverse dipolar excitations.

Thus, a continuous transition from spherical Mie resonances to Fabry-Pérot modes and then to the leaky mode resonances of an infinite cylinder has been demonstrated. The FP modes are defined by a transverse (l) and a longitudinal (n) resonance condition, which can be identified by observing the near field distribution through the center of the nanorod. As the nanorod is extended, new modes appear with the same l value but with n taking increasing odd values. Each family of FP modes (l = 1, 2, 3 etc.) converges to a corresponding waveguide mode.

3.3 Near field enhancement

Combining two or more nanoparticles to form more complex assemblies is a common avenue of investigation in plasmonics and nanophotonics research. A desirable feature of plasmonic devices is their ability to enhance electromagnetic radiation in nanoscale volumes. Often, the field enhancement from a single nanoparticle can be further improved by placing a second complementary structure in close proximity, with interparticle separation on the order of tens of nanometers. In the simplest case, this is a mirrored version of the same particle. Such plasmonic dimers have already been shown to greatly magnify the local electric field [91–94]. Metal based structures are inherently lossy, however. In order to circumvent this, we explore the near field enhancement in the center of the gap between two GaP nanorods of equal length and with a separation distance of 20 nm.

We simulated a number of dimer structures with nanorod lengths between 300 nm and 1400 nm. In terms of the far field, the introduction of a second nanorod results in mostly small changes to the extinction spectra, such as the broadening of some resonances. In fact, the greatest modification to the extinction was found to be for the case of a dimer

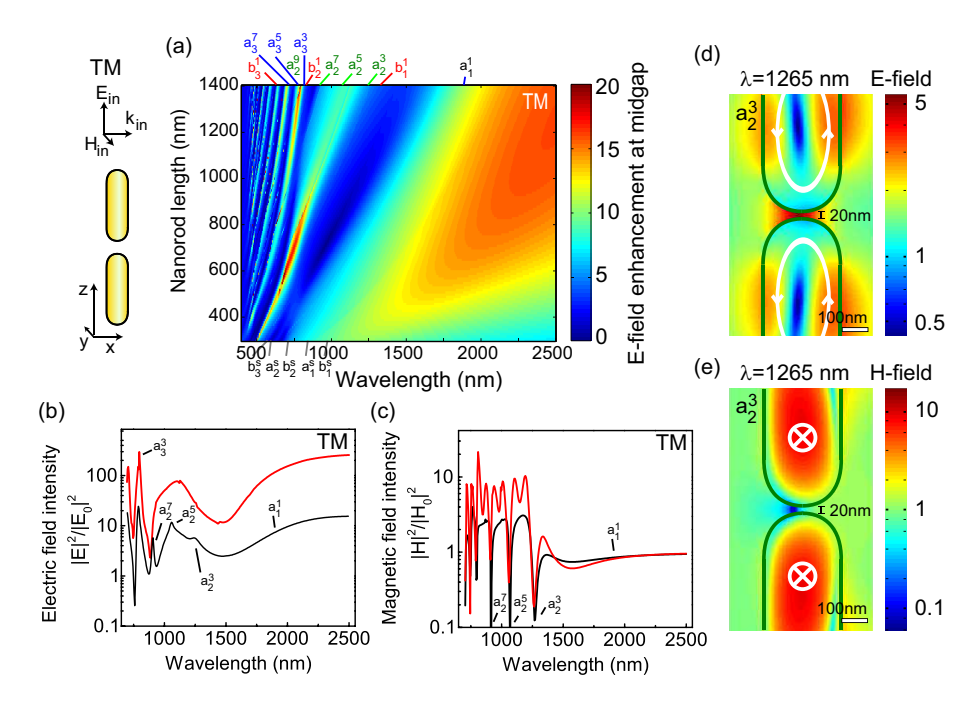


Figure 3.7: (a) Electric near field enhancement at the midgap of a 300 nm diameter nanorod dimer, as a function of nanorod length. (b,c) The electric and magnetic near field intensity enhancement at the midgap of the same dimer structure (red) and 10 nm away from the tip of a single L=1400 nm nanorod (black). (d,e) Colour maps showing the magnitude of the electric and magnetic field, relative to the incident field, through the center of the structure in the xz-plane. The a_2^3 mode simultaneously demonstrates electric field enhancement and significant magnetic field suppression. All results are for TM polarised incident light.

comprised of spherical particles, where the l=1 and l=2 modes shift significantly. The electric and magnetic dipole modes even appear to be suppressed under TE polarised illumination [52]. Departure from spherical geometry reduces the extent of these coupling effects. For those that are interested, the far field spectra of the dimer are included in the appendix.

Turning our attention to the near field we find much more evidence of interaction between the two nanorods. Figures 3.7(a) and 3.7(b) show that, for TM polarisation, electric field enhancement is achieved for a broad range of wavelengths. This would appear to be linked to the a_1^n mode. Strong enhancement is also obtained for the a_3^n FP modes. For these sets of modes, we can expect to see constructive coupling as they were found to have E-fields that flowed in the same direction at both ends of the nanorod. On the other hand, the a_2^n modes, were found to have opposing E-fields at tips of the nanorod. In this case, we still see E-field enhancement, but not to the same extent (see Figure 3.7(d)). Of particular interest is the region where the a_3^n and a_2^n modes overlap. The stongest E-field enhancement is obtained between the nanorod lengths of 500 nm and 800 nm, at a wavelength around 750 nm. Thus, it appears that local field enhancement can be optimised by careful design of overlapping resonances.

In Figures 3.7(b) and 3.7(c) we compare the results for the nanorod dimers with the single nanorod. It is found that, for TM polarisation, the electric field intensity is more than an order of magnitude greater at the center of the dimer than for an eqivalent distance from the single rod. Thus, semiconductor antennas have the capacity to concentrate optical fields in a nanoscale gap, much like their plasmonic counterparts. For the case of TE polarisation, similarly large enhancements are found for the magnetic field. This is associated with the b_1^n FP modes as well as for the b_1^1 cylindrical mode. While most magnetic resonances are strongly contained inside the high-index semiconductor, the evanescent coupling between adjacent wires can still lead to a significant enhancement [52].

A rather remarkable feature that becomes apparent from this investigation is the ability of the semiconductor nanorods to suppress the magnetic field at their tips. In Figures 3.7(c) and 3.7(e), we see that the magnetic field in a minute volume close to the nanorod tip is strongly suppressed for the a_2^n modes. It is clear from the near field maps of Figure 3.3 that this effect is not due to a particular radial symmetry point (node) in the mode distribution, nor destructive interference between the two nanorod modes. The magnetic mode profile of the a_2^n modes consists of pronounced magnetic field poles perpendicular to the nanorod axis, resulting in dipoles in each tip that are parallel and side-by-side. In fact, the introduction of a second nanorod actually reduces the extent of this magnetic field suppression, as indicated in Figure 3.7(c). The concentration of magnetic fields inside the nanorod causes a resonant suppression of field strength at the wire tips below that of the incident light field, with a pronounced dip in the field strength in a small volume. Such a resonant magnetic field 'void' may be of interest for applications in decoupling of magnetic emitters to radiation and thus, suppressing their decay rates [52, 68]. The electric and magnetic near field enhancement or suppression for both polarisations is explored further in the appendix.

Next to possible applications in nonlinear optics, tuning of near field properties is of interest for optical forces. In related works, Xifré-Pérez et al. showed that the bonding or antibonding of low order Mie resonances allows the control of the particles' position relative to each other; the force of the coupling overcoming gravity and van der Waals forces [95]. While we studied here the effect of end-to-end coupling, other coupling configurations may be of interest. Cao et al. investigated the coupling for adjacent nanowires, placed so that their long sides were in close proximity [96]. Their work demonstrated how the far field scattering can be modified by the coupling of leaky mode resonances for infinite wires. In general, the dielectric nanoantenna is unlikely to match its metallic counterparts in terms of near field enhancement, however, the absence of absorption at wavelengths well into the visible range makes the dielectric antenna a potential alternative for applications in nonlinear optics and field enhanced spectroscopies [97, 98].

3.4 Varying the angle of incidence

So far, our simulations have focused on the special case of normal incidence. For real world applications, however, this will not always be the case; we also need to know how the response changes with the angle of incidence. A number of simulations were run for both an infinite cylinder and a finite nanorod of length L=1400 nm for TM and TE polarised light. The angle of incidence, ϕ , was varied from nearly 0° (grazing incidence) to 90° (normal incidence), as measured from the nanorod axis. For the case of the infinite wire, the modes become increasingly narrow as the angle approaches zero. This is due to the conversion of the cylindrical modes into weakly-damped guided modes [78, 83]. As the cylindrical Mie resonances are a function of the angle of incidence [44], we see a continuous evolution of the mode positions across the spectrum (angular dispersion).

In contrast, we observe no such angular dispersion for the finite length nanorods. There is no spectral narrowing, consistent with the absence of true guided modes in a finite length structure. Instead of a continuous evolution, the mode spectrum for a nanorod is composed of localised modes with fixed resonant wavelengths. The angle of incidence determines which modes are excited based on their symmetry and phase matching requirements. Moving towards small angles, the difference between TE and TM polarisations becomes indistinguishable. At grazing incidence, select modes from both the original TE and TM spectra can be excited, such as the a_2^3 and b_2^9 modes shown in Figures 3.8(g) and 3.8(h).

If we consider specific wavelengths, we see that the scattering spectrum shows oscillations as a function of angle as well as wavelength. These oscillations are shown in Figures 3.8(e) and 3.8(f) for a number of different modes. Higher order modes show several oscillations as the angle is varied, due to their excitation being dependent on phase matching. Lower order modes, on the other hand, are seen to fade in and out only once over the angular range. Varying the angle of incidence also allows other modes to be excited, as indicated by stars in Figures 3.8(c) and 3.8(d). These modes are attributed to even-order FP modes and are resonant at angles between those that excite odd-order modes. These even-order modes cannot be excited at normal incidence due to their lack of mirror symmetry, but are effectively excited for certain oblique incidence conditions. This is the result of phase retardation, similar to the case of plasmonic nanorod antennas [99, 100].

3.5 Conclusions

In this chapter we investigated the optical response of low aspect ratio semiconductor nanorods. We established the nature of the intermediate regime between the fundamental Mie resonances of a sphere and the radial Mie/leaky mode resonances of an infinite

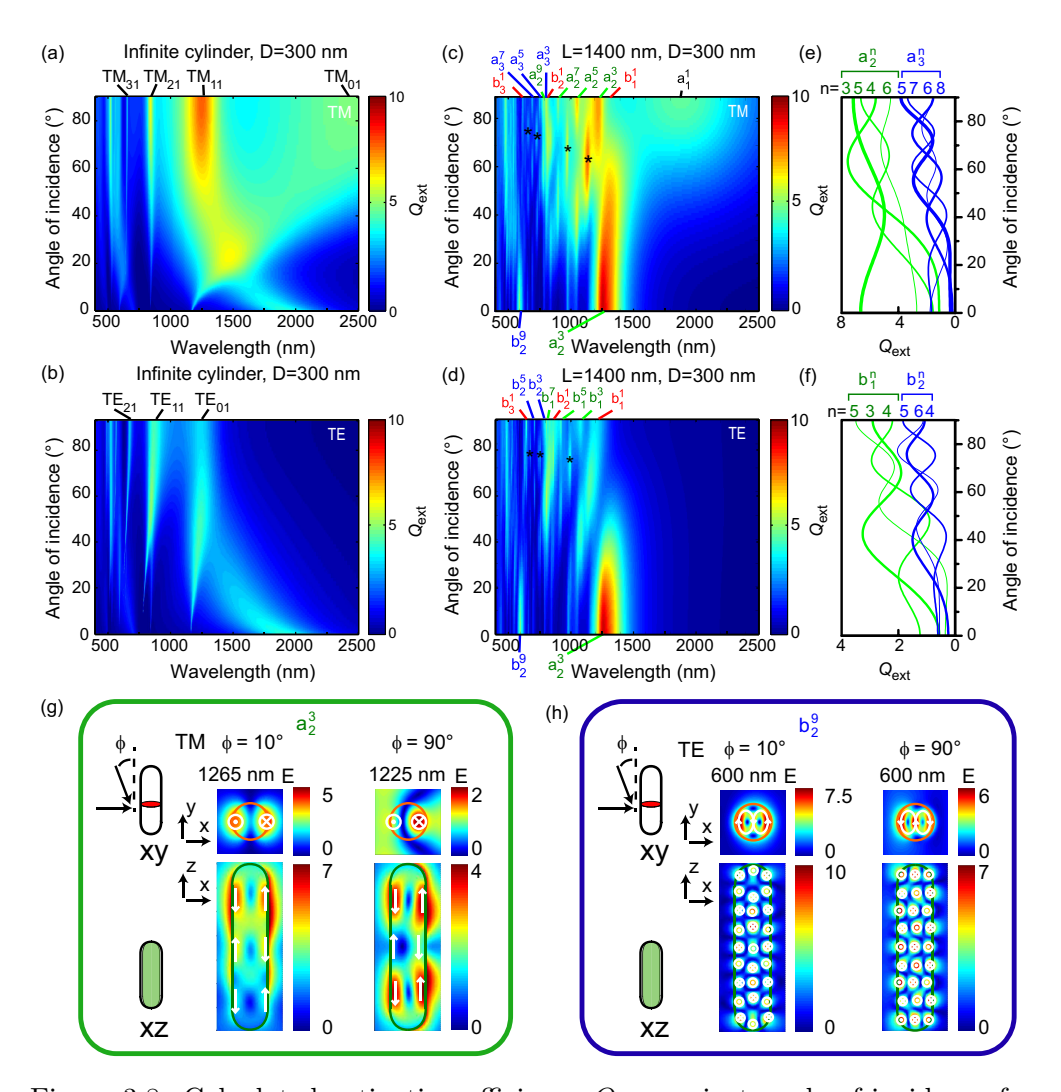


Figure 3.8: Calculated extinction efficiency $Q_{\rm ext}$ against angle of incidence for an infinite cylinder (a,b) and for finite rods with length L=1400 nm (c,d), both with a 300 nm diameter. Polarisations correspond to TM (a,c) and TE (b,d). Stars indicate even-order FP modes excited at oblique angles of incidence. (e,f) Line graphs showing the angle dependence of $Q_{\rm ext}$ (i.e. taken from maps (c) and (d) at selected wavelengths) for modes a_2^n and a_3^n for TM and b_1^n and b_2^n for TE. (g,h) Calculated mode profiles (both E and H fields) for selected modes a_2^3 for TM and b_2^9 for TE polarisations, for angles of incidence of 10° and 90°. A small shift in the resonance wavelength for a_2^3 is attributed to changes in mode distribution for different incident angles.

cylindrical wire. The longitudinal-field Mie resonances (a-type for TM and b-type for TE) evolve into antenna modes described by a two dimensional Fabry-Pérot model. We are able to classify different families of antenna modes based on their scaling with antenna length, which is determined by combining longitudinal and transverse mode components. Furthermore, it is found that the magnetic b-type Mie resonances undergo a continuous transition into either the electric (TE) or magnetic (TM) radial eigenmodes of the infinite wire.

When two nanorods are placed end-to-end to form a dimer, a notable electric field enhancement in the gap can be achieved. Depending on the dimensions of the nanorod, a narrow- or broad-band effect can be realised. Such characteristics make semiconductor structures a potential alternative to plasmonic devices in cases where losses due to absorption are unacceptable. In addition to large enhancements of the electric field intensity, semiconductor nanorods are capable of almost complete quenching of the magnetic field in the center of the gap, allowing for engineering of vacuum fluctuations.

Finally, we studied the optical response as a function of the angle of incidence. For an infinite wire, we see a continuous angular dispersion as the cylinder modes transition to leaky waveguide modes. For the low aspect ratio nanorod, we instead observe a discrete spectrum with individual modes that are excited with different efficiencies depending on phase matching with the incident wavefront. The pronounced differences between the angle-dependent spectra of the infinite wire and finite nanorod emphasises the need for thorough simulation of such structures for applications in photonic devices.

Chapter 4

Light Scattering and Extinction of Single and Dimer GaP Nanorods

4.1 Introduction

In the previous chapter, we took an in depth look at the response of semiconductor nanorods to an incident electromagnetic wave. This discussion was purely theoretical. The simulation only considers the ideal case; a free-standing stucture with a precise geometry. If we are to use these semiconductor nanorods for photonic devices, we must experimentally explore the scattering and extinction from a single nanorod. In addition to confirming the model description, we look to establish new properties of isolated nanowires for application in photonic circuits.

In this chapter, we use a number of approaches aimed at investigating cavity resonances in a GaP nanorod. Comparison with numerical calculations provides global trends and reveals disagreements between theory and experiment. This chapter explores the capabilities of the experimental techniques in detecting the single-antenna response and investigates the physics behind some unexpected results. To aid in this, Comsol simulations are employed to probe the system further by including the substrate, and by considering the reflection and transmission rather than absolute extinction cross sections.

4.2 Methods

4.2.1 Sample preparation

To achieve a well defined structure and constant diameter, the nanorods were grown vertically as wires on a GaP substrate. This was done by the group of Prof. Erik Bakkers using Metal-organic Vapour Phase Epitaxy (MOVPE, see Chapter 2). To serve

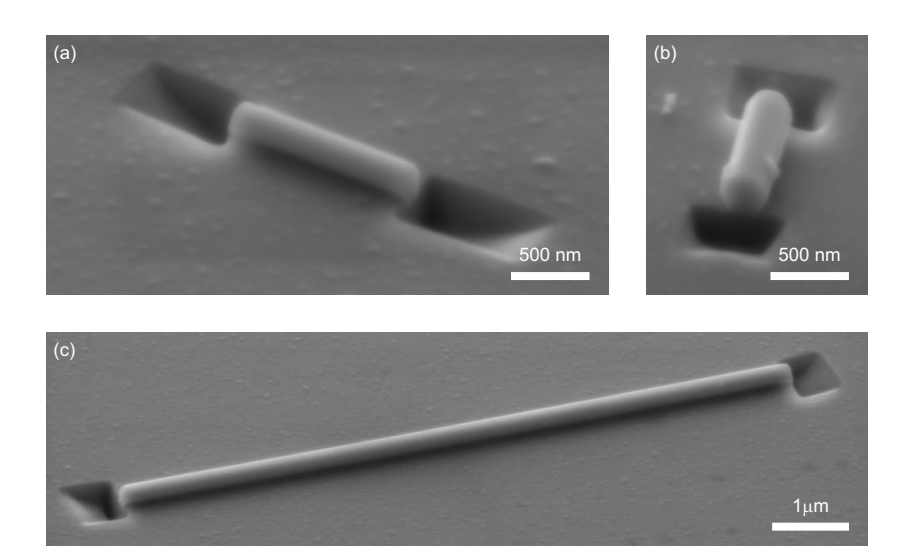


Figure 4.1: SEM images of the nanorods milled to various lengths using FIB. (a) Length: 1.25 μ m, diameter: 220 nm. (b) Length: 1 μ m, diameter: 290 nm. (c) Length: 8.65 μ m, diameter: 250 nm. This nanorod was used for comparison to the analytical model for an infinite cylinder.

as the sample base, a square glass chip was prepared with a marker grid to help locate appropriate nanowires. A 20 nm layer of indium tin oxide (ITO) was sputtered on top of this chip to act as a transparent conductive layer in order to reduce charge build-up when imaging with a SEM. The GaP nanowires were pressed onto this glass sample, transfering a large number of nanowires.

With a random sample of nanowires, the next step was to create nanorods of an appropriate length. This was achieved using focused ion beam (FIB) milling with the assistance of Dr. Stuart Boden. Both ends of suitably isolated nanowires were milled, creating nanorods with a well defined shape but varying lengths and diameters. Examples can be seen in Figure 4.1. It should be noted that the milling process results in trenches at the ends of the nanorod which may effect its scattering. Due to the nature of the deposition, the nanorods are randomly oriented. To ensure correct polarisation of incident light in our experiments, the sample was mounted on a rotating stage.

4.2.2 Dark field set-up

The first experiment was designed to measure the scattering spectrum of each nanorod. The set-up can be seen in Figure 4.2. A polarised white super-continuum laser source is directed onto the nanorod at a wide angle and the light scattered by the nanorod is collected by a focusing objective with low numerical aperture. The collimated light is then passed through a confocal pinhole in order to remove all light not scattered by the nanorod under investigation. From there, the light is either focused on to a camera or the spectrometer. The pinhole is attached to a magnetic mount so that it may be removed when imaging the sample.

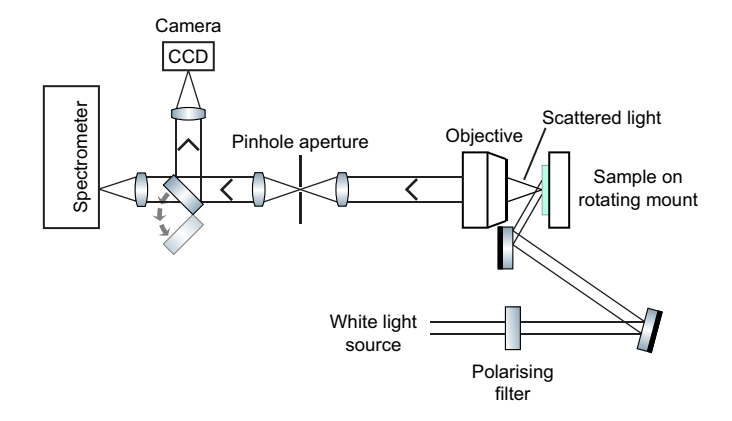


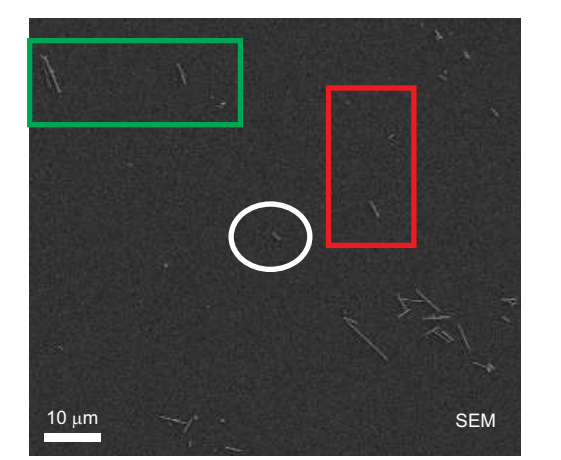
Figure 4.2: The dark field spectroscopy set-up. A focusing objective is positioned in front of the sample such that only scattered light is captured and collimated. A pinhole aperture is used to remove light that is not scattered by the nanorod. A flipping mirror allows for either imaging the nanorod or measuring with the spectrometer.

The sample and rotating stage are mounted on top of a 3-axis translation stage, with micrometer screws. When a nanowire is initially selected under the SEM, its coordinates are recorded along with the coordinates of the nearest marking structure. This marking structure is large enough to be easily identifiable when imaging with the dark field setup. From there, the translation calculated from the SEM coordinates can be followed back to the desired nanorod. A SEM and dark field image of the same nanorod are shown in Figure 4.3, highlighting how unique features of the sample aid in locating the required nanowire once in the correct area of the sample. Once identified, the nanorod then needs to be rotated, such that the white-light source is incident perpendicular to the nanorod axis. The white light source is aligned horizontally to the optical bench so the nanorod axis need simply be aligned vertically. Finally, the nanorod needs to be aligned so that it is visible through the pinhole aperture. Once the nanorod is in position, the scattering spectrum can be measured.

For each set of measurements, a reference spectrum was taken using a sample of zinc oxide (ZnO) paint. The scattering from the surface of this paint should be uniform across the measurement range, allowing us to detect how the source power and the sensitivity of the spectrometer varies with wavelength. The nanorod spectra are divided by this reference spectrum, eliminating any wavelength dependent variation in the source power.

4.2.3 Spatial modulation set-up

Spatial modulation was employed to measure the particles extinction spectrum. This technique should reduce the effects of the substrate as it is able to isolate the contribution of the nanorod to the measured spectra. The set-up used for this experiment can be seen in Figure 4.4. A polarised, variable wavelength source is focused onto the sample using a reflective objective. The position of the focus is modulated by a piezo actuated



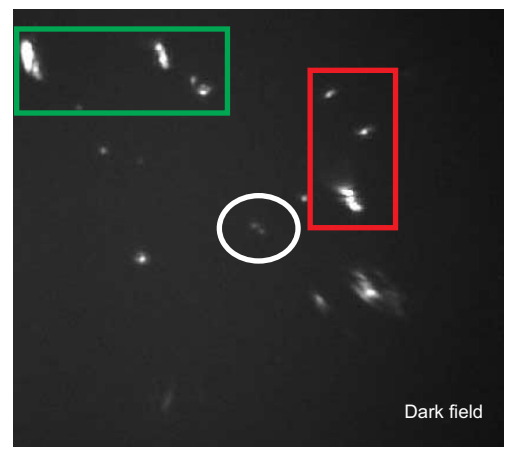


Figure 4.3: The required nanorod (white ellipse) is located by translating the stage a measured distance from an easily identifiable marker. Features of the sample, such as the unique arrangements highlighted in the red and green rectangles, are then used to find the exact position of the nanorod.

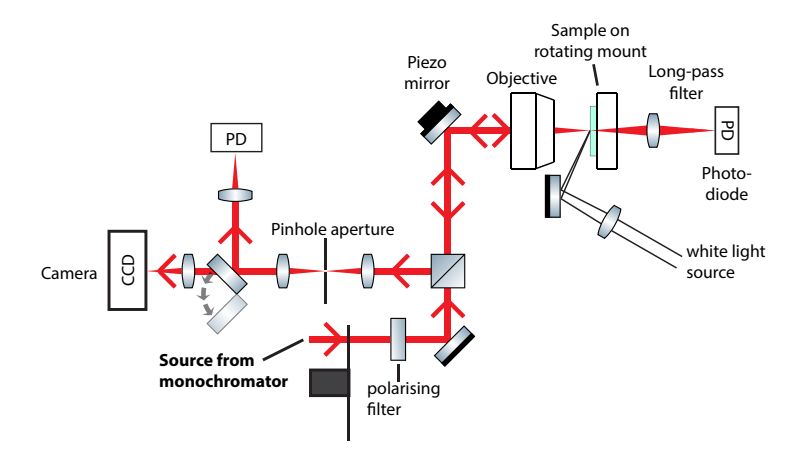


Figure 4.4: Spatial modulation set-up. A wavelength variable source is passed through a linear polariser before being focused by a reflective objective. A piezo actuated mirror is used to modulate the position of the beam focus relative to the nanorod on the sample. Two photodiodes, used in conjunction with a lockin amplifier, allow the measurement of nanorod extinction in either reflection or transmission. A chopper provides a second source of modulation to allow for the measurement to be normalised to the wavelength dependent source power.

mirror. A second white light source is used in a dark field configuration to allow the sample to be imaged.

As with the dark field set-up, a confocal pinhole aperture is used to isolate the contribution from the nanorod in question, however, this is less critical given the tight focusing of the light. A photodiode is used, in conjunction with a lock-in amplifier and the reference from the piezo controller, to allow the light directly reflected from the nanorod to be measured. This provides the differential signal, dR. A second photodiode was included later so that spatial modulation measurements could also be taken in transmission, the modulated signal referred to as dT in this case. As the intensity of the laser is not

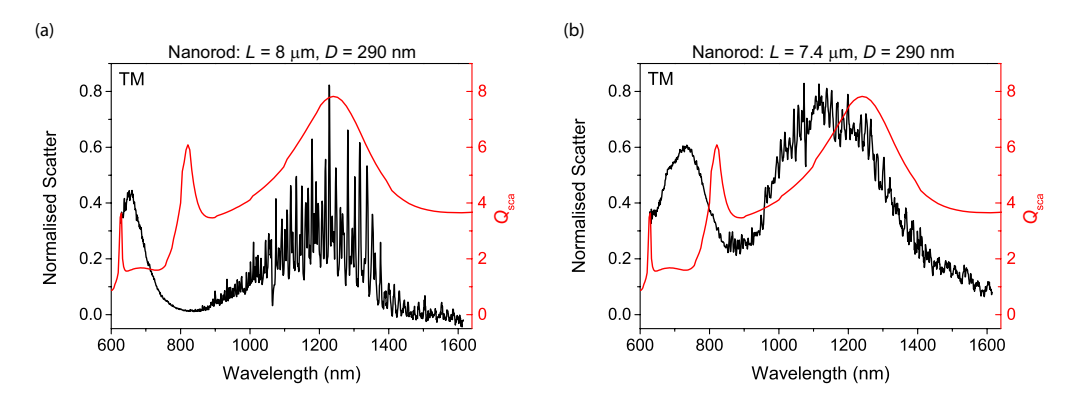


Figure 4.5: Comparison of the measured scattering spectra (black) of a "long" nanowire of diameter 290 nm and simulated scattering spectra (red) of an infinite cylinder of the same diameter. (a) Scatter of a nanowire with a length of 8 μ m before improvements were made to the set-up. (b) Measured scatter of the same nanowire after improvements were made. The ends of the nanowire were milled to produce a cylindrical structure, reducing the length to 7.4 μ m. These results are for TM polarised light.

uniform across its spectrum, a chopper is included in the input path so that the differential signal can be normalised. The modulated signal induced by the chopper gives the overall light reflected from or transmitted through the sample, referred to as R and R, respectively. Henceforth, the normalised spatial modulation signal is referred to as R and R or R or R.

4.3 Results

4.3.1 Dark field spectroscopy

Initial measurements from the dark field set-up showed a substantial amount of noise. In Figure 4.5(a), we can see that the signal between 1000 nm and 1400 nm shows an unusual number or sharp peaks, resembling a speckle pattern. Many of the resonances that appeared in the simulations are spectrally narrow and would not be distinguishable from the speckle apparent in these measurements. It seems likely that this speckle was caused by scatter from the substrate as there is no reason why the noise of the system would increase in this wavelength range. To check for this, and to make sure that we were measuring the strongest signal from the nanowire, the translation stage was used to measure the scattering spectrum along its length. Example results can be seen in Figure 4.6.

Due to the low numerical aperture of the objective and the presence of the pinhole, it is likely that only a small portion of scattered light is measured by the set-up. It was also necessary, therefore, to ensure that the spectrum of the nanorod did not vary with its length. The strongest signal is found to be at the center of the structures for both single

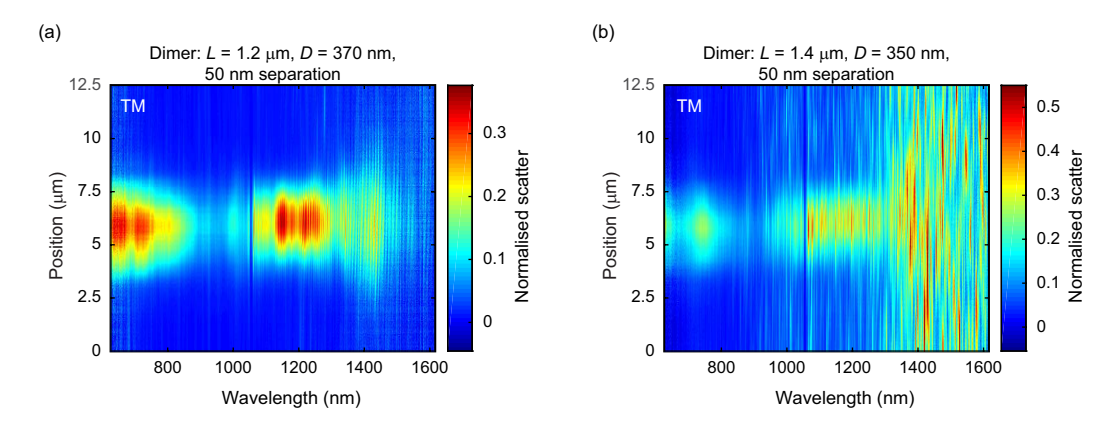


Figure 4.6: Scattering spectra as measured along the length of a nanorod dimer. (a) A dimer with an arm length of 1.2 μ m, diameter of 370 nm and a separation of 50 nm. (b) A nanorod dimer, with an arm length of 1.4 μ m, diameter of 350 nm and a separation of 50 nm. Both measurements are for TM polarised illumination.

nanorods and dimers, and there is no evidence of unique scattering at the tips. The speckle pattern, however, varies with position along the nanorod and persists beyond its length. This can therefore be ruled out as being part of the nanorod scattering signal. In order to detect narrower resonances, as seen in the simulations, actions needed to be taken to improve the measurement system.

In order to reduce the speckle, a rotating ground glass diffuser was placed in the input channel. This reduces coherence in the beam, allowing the speckle to be averaged out. However, adding such a device also reduces the beam power, so a 30 cm focal length lens was added to weakly focus the beam on the sample and boost the signal strength.

With these modifications, we see a definite improvement in the spectra. This is evident in Figure 4.5(b), where the measured scatter from the same nanowire shows greatly reduced noise. We are able to see some qualitative agreement between the shapes of the simulated and measured results. Two peaks are present that roughly line up with resonances in the simulated data, albeit slightly blue-shifted; one at 730 nm and a broader resonance at 1140 nm. The remaining resonance in the infinite wire, the b_3 mode at 630 nm, has likely shifted outside the measurement range.

Further results can be seen in Figure 4.7. Each spectrum has a sharp feature at around 1070 nm. This is an artefact of the set-up and normalisation caused by a minute drift of the intense peak from source's seed laser. Overall, there is definitely some qualitative agreement with a number of the features from the simulations. Figures 4.7(a) and 4.7(c), in particular, show a good match in the overall shape, with peaks at around 1070 nm and another between 600 nm and 700 nm that match the broader resonances from the BEM calculations, the b_1^1 and b_2^1 modes. There is also a small feature at 925 nm for the 1.2 μ m nanorod and at 825 nm for the 1.35 μ m nanorod that could be one of the sharper resonances in the simulated spectra, being the a_2^3 and a_2^5 modes respectively.

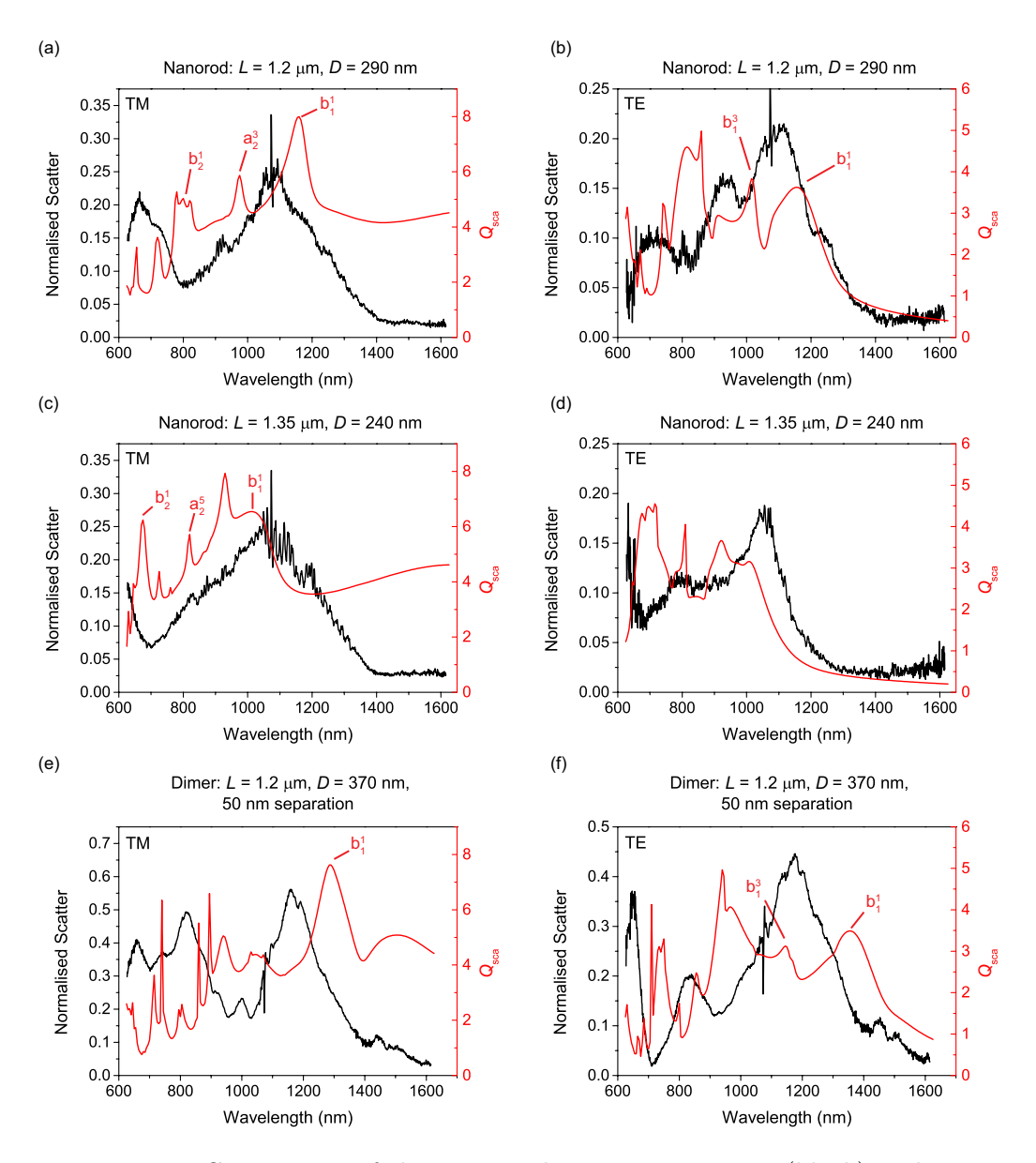


Figure 4.7: Comparison of the measured scattering spectra (black) and simulated scattering spectra (red), using a ground glass diffuser in the input channel. (a, b) A single nanorod with a length of 1.2 μ m and a diameter of 290 nm. (c, d) A single nanorod with a length of 1.35 μ m and a diameter of 240 nm. (e, f) A nanorod dimer with an arm length of 1.2 μ m and diameter of 350 nm. Results are shown for (a, c, e) TM and (b, d, f) TE polarised light.

The TE modes of the single nanorods (Figures 4.7(b) and 4.7(d)) do not match as well. Unlike for TM polarisation, the two nanorods show little resemblance in their spectra, for both the measured and simulated case. This suggests that the TE modes of the nanorod are much more sensitive to the diameter of the nanorod. The comparison of the two does highlight how the measured spectra broadly match up to the numerical results. The scattering of the thicker nanorod, for example, persists further into the infrared. The measured and simulated spectra in Figure 4.7(b) both show a number of individual peaks, whereas the spectra in Figure 4.7(d) have fewer but broader resonances. In this case, the simulated spectrum indicates that several of the nanorod resonances overlap.

The nanorod dimer is milled from a thicker nanowire and, as a result, the spectra in Figures 4.7(e) and 4.7(f) are much more complicated. With the overall spectrum significantly red-shifted, the simulated spectra contain many more resonances, making it difficult to draw comparisons to the measurements. It was noted in Chapter 3 that the extinction spectrum of a nanorod and a dimer with the same component dimensions were almost identical (evidence of this can be seen in the Appendix). The spectra of the dimer should thus be comparable to the 1.2 μ m single nanorod, their diameters being the only differing factor in defining the scattering spectra.

Comparison of the simulated results for the single nanorod and dimer under TM polarised illumination does not reveal much in the way of similarities. The only resonance that would appear to be comparable is the b_1^1 mode at 1160 nm in the single nanorod. In the simulated data, this resonance shifts to 1290 nm in the thicker dimer. Such a shift is also evident in the measured spectra, the longest wavelength peak shifting from 1070 nm to 1160 nm. The TE spectra are slightly more comparable, particularly the first and second peak corresponding to the b_1^1 and b_1^3 modes. The former shifts from 1160 nm to 1360 nm, while the latter only shifts from 1015 nm to 1145 nm. This smaller shift may be reflected in the measured spectra with the largest peak shifting from 1095 nm to 1175 nm. This does not necessarily mean that the b_1^1 mode is not present in the measured spectra, however. A smaller feature is identifiable at 1230 nm in the single nanorod measurement and again at 1445 nm in the dimer measurement.

A common feature of all three TM measurements is the absence of the electric dipolar mode, a_1^1 . This is expected to be the lowest energy mode in any nanorod with a length that is three or more times its diameter. The presence of this resonance is the reason the simulated scattering for TM polarisation doesn't drop to zero at the infrared end of the spectra. The measured spectra invariably fall to a minimum at this point, indicating that the set-up is not detecting the scattering of the electric dipolar mode.

Thus, we see that dark field spectroscopy is capable of detecting only some of the resonances seen in the BEM simulations. Quantitatively speaking, the measurements and simulations are not a good match. The exact resonance positions are shifted and the relative size of the features are different, making it difficult to determine the nature of

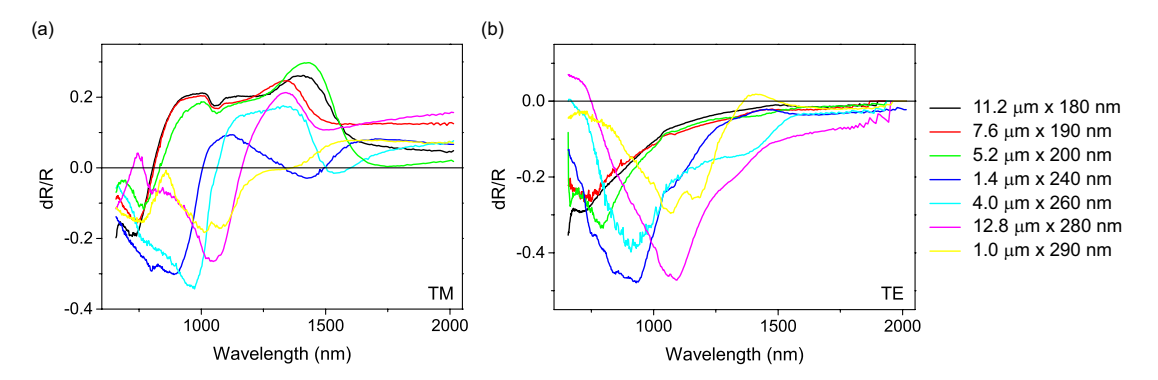


Figure 4.8: Spectra of a number of nanorods taken using the spatial modulation set-up in reflection, under TM (a) and TE (b) polarised illumination. The nanorods are of varying length, however, the broader features are expected to be much more sensitive to the nanorod diameter.

the measured resonances with any certainty. This is to be expected due to the sensitivity to the size and shape of the particle and the materials involved. There is also the angular dependence to consider. This will be discussed in detail later in this chapter.

4.3.2 Spatial modulation spectroscopy

Nanorods of various lengths and diameters were measured using the spatial modulation set-up, the results of which can be seen in Figure 4.8. The results obtained for TM polarised light are clearly not representative of the particles' absolute extinction cross section. The measured spectra have both negative and positive regions. This indicates that the nanorod is capable of both reducing and increasing the reflected light, depending on the incident wavelength. For TE polarised light, the measured spectra remain almost entirely negative.

The spectra of Figure 4.8 are considered based on the diameters of the nanorods. For the different nanorods we see similar features that shift with nanorod diameter. The features for TM polarisation show evidence of modes extending further into the infrared than those observed for TE polarisation. This is in contrast to the dark field measurements which showed no such longer wavelength features for either polarisation.

For both TM and TE polarised illumination, we see a red-shift in spectral features as the diameter of the nanorod is increased. This is clear for the TE spectra as they all show only a single negative peak, but the same is true of the TM spectra. The initial negative peak at $\lambda = 750$ nm for a diameter of 180 nm (black), shifts to around $\lambda = 1050$ nm for a diameter of 290 nm (yellow). The intersection where dR/R = 0 also red-shifts as the diameter increases, moving from around $\lambda = 800$ nm to $\lambda = 1250$ nm.

The fact that the spectra shift depending on the diameter of the nanorod is a strong indicator that this is not simply an artefact of the set-up. Measurements were also

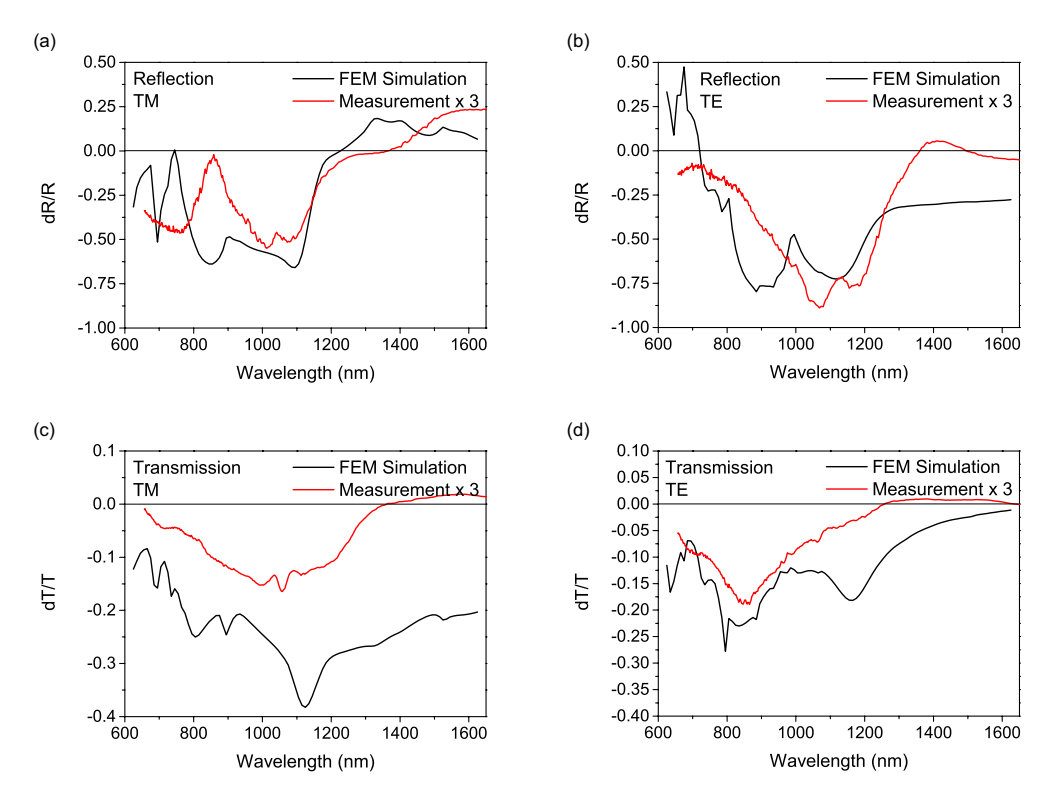


Figure 4.9: Comparison of the spatial modulation signal for reflection and transmission from a selected nanorod. Comsol simulation results (black) are plotted against the spatial modulation results (red) obtained for a nanorod with a length of 990 nm and diameter of 290 nm. Results are obtained for both (a,b) reflection and (c,d) transmission. The simulation and measurements are performed for both (a,c) TM and (b,d) TE polarised illumination.

taken in transmission to see if a similar behaviour would be measured. In this case, the measured dT/T signal was almost entirely negative for both polarisations. This indicates that, in a certain wavelength range, we are measuring simultaneous reductions of the reflected and transmitted light.

To further investigate the origin of this signal, a Comsol model was devised to simulate the experimental results. This comprised of a cylindrical nanorod on top of an airglass interface. As was the case of the BEM simulation, light is inserted as a plane wave perpendicular to the nanowire with either TM or TE polarisation. Light is then extracted from the the simulation volume via a port located some distance below the air-glass interface. The model was designed to run twice for each polarisation; once with a nanorod present, and once with the nanorod volume set to air. This allowed back-to-back simulations that give the transmission and reflection of the nanorod and bare glass surface. Subtracting the two and dividing by the result for the bare glass gives the equivalent dR/R or dT/T result.

The simulation was run for a number of different nanorod sizes. The results of one such nanorod are shown in Figure 4.9. The simulation results share several features with the

measured spectra. In Figure 4.9(a) both the measured and simulated spectra show a point where the negative signal is reduced to zero. This is at 745 nm in the simulation and 860 nm in the measurement. At lower wavelengths we see a single resonance in both the simulated and measured spectra. Moving to higher wavelengths, both spectra show a double peak, however the measurement shows these peaks to be much closer together. Beyond this the signal becomes positive, the separation in the crossing point being similar to the zero point mentioned earlier.

Similar qualitative comparisons can be made for the other spectra. For Figure 4.9(b), both spectra are dominated by a double peak but, once again, the measurements show the two peaks to be closer together. In Figure 4.9(c), we see a single peak at the center of a much broader signal. In this case the simulation shows a number of shorter peaks towards the visible end of the spectrum which are not replicated in the measurement. For Figure 4.9(d), we see only a single peak at 850 nm, matching a broader resonance from the simulation. The second broader resonance, at 1160 nm in the simulation, is not reproduced, however. Once again, a number of small peaks can be seen in the simulation towards the visible range which are not present in the measurement.

A common feature across all four measurements is a positive tail at the infrared end of the spectrum. This is only seen in the simulation for reflection under TM illumination. While this is the only case for which the measurement is positive by a significant amount, this indicates a potential offset in the dR and dT signals.

As mentioned, a number of small features in the simulations are not replicated in the experiment. In addition to this, the comparison shows some features of the measurements to be red-shifted (zero crossings in Figure 4.9(a)) while others are blue-shifted (features of Figure 4.9(c)), compared to the simulation. The reason for this may lie in the simplification of the sample for the purposes of the simulation. The ITO layer, for example, was not included in the simulation geometry. The surface of the glass was also assumed to be flat, ignoring the trenches created by the FIB milling. The overall shape of the spectra do, however, roughly match the measured results and we see good agreement of the positive and negative features. It is enough to indicate that our measurements are of the nanorod response and not some other aspect of the set-up.

The simulations confirm that it is possible for both the transmitted and reflected light to be reduced by the presence of the nanorod. This is most likely due to large angle scattering that is not detected by the set-up due to the limited numerical aperture. To test this theory and also determine the source of the positive signal in reflection, the near field data from the Comsol simulation was used. The diagrams of Figure 4.10 are divided into two vertical halves. The left half of each panel shows the electric field, E_y , of the light as it is reflected from and transmitted through the air-glass interface. The right half of each panel shows the electric field of the light scattered by the nanorod.

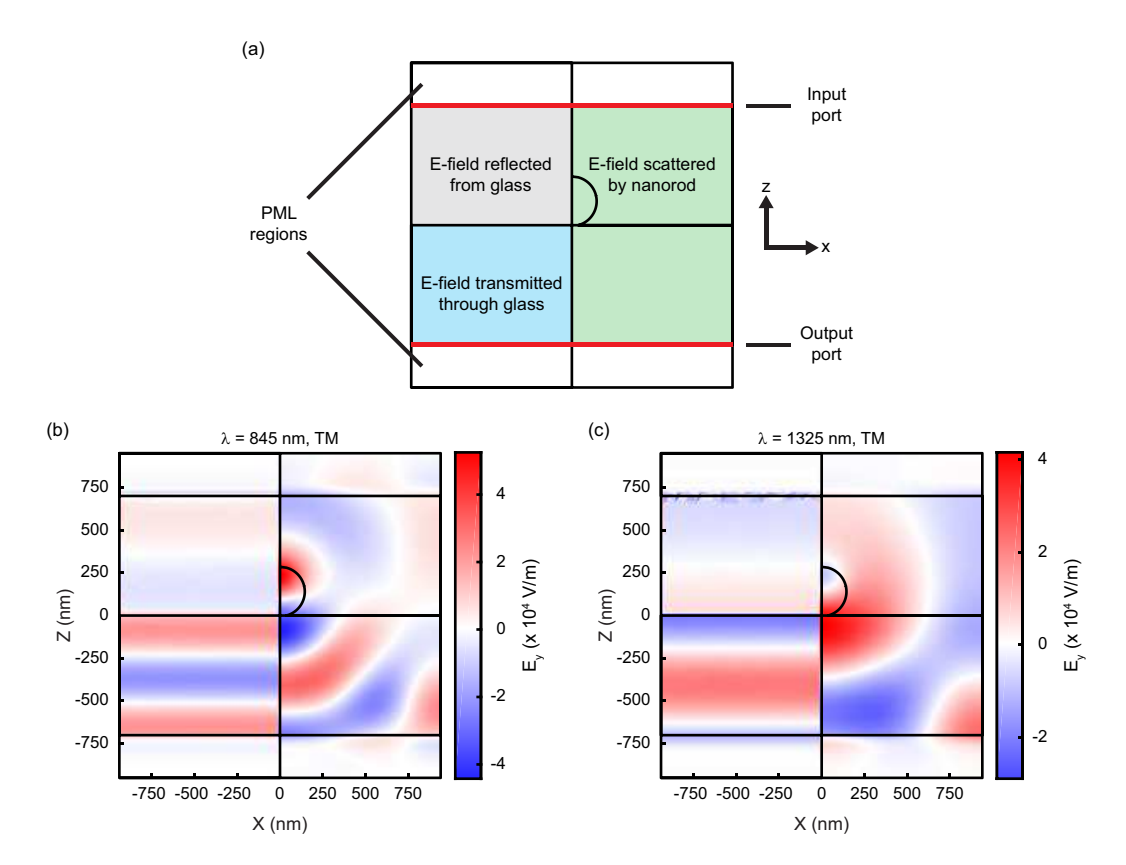


Figure 4.10: Near field data from the Comsol simulations. (a) An illustration of how the E_y plots are divided. (b) Distribution of E_y at $\lambda = 845$ nm. (c) Distribution of E_y at $\lambda = 1325$ nm.

This information was found by subtracting the E_y data of the bare glass simulation from the E_y data of the simulation with nanorod. This is further illustrated in Figure 4.10(a).

Figure 4.10(b) shows that the electric field oscillates radially outwards from the nanorod, indicating that light is scattered in all directions at a wavelength of 845 nm. This is not always expected to be the case, as will be discussed further below, but this demonstrates that light can easily be scattered outside of the experimental set-up. Figure 4.10 also shows that the phase of the scattered light compared to the background wave can be very different, depending on the wavelength. Generally speaking, we would expect a π phaseshift in the radiated wave when going across a resonance. For a Mie scatterer, however, this is not the case as a phase shift is also accumulated inside the scatterer. This will differ depending on the near field distribution inside the nanorod. This was touched upon in Chapter 3 when determining why the dispersion of the a_1^1 mode did not match our analytical model. The absolute phaseshift will vary across the spectrum, allowing the scattered and reflected light to interfere constructively for some wavelengths.

Thus, in terms of measuring the extinction cross section of a nanorod, the best representation is found in transmission. However, there are a number of issues that need to

be considered when using this technique to measure the spectrum of a highly scattering sample. The advantages and disadvantages of both measurement techniques will be discussed in the next section.

4.4 Discussion

The two techniques examined have the capability to measure very different things. The dark field measurement detects only scattered light from the nanoparticle, while spatial modulation would also be affected by the nanoparticle's absorption. At first glance, the glass substrate would appear to be irrelevent in either case. For the dark field set-up, the light is incident on a relatively flat surface at a large angle. Any light scattered by the substrate in this configuration would be negligible were it not for the trenches milled into the glass surface. Spatial modulation, is intended as a measurement of the nanoparticles' extinction. The extinction of a particle is defined as the amount of light removed from a defined beam, and the modulation allows this precise signal to be extracted. However, what is actually detected is the difference between signal from a bare substrate and signal from a particle on a substrate. This would normally be simple to accommodate for but the varying phase pickup inside the nanoparticle means that the scattered light interferes constructively or destructively with the reflected/transmitted light, depending on the wavelength.

It should be noted, of course, that the presence of the substrate will produce a small wavelength shift in the nanoantenna resonances. As has been previously stated, the nanoantenna resonance is determined by not only the properties of the nanorod but also its surrounding media. This effect has been investigated using Comsol. Overall it was found that the presence of the substrate produces a red-shift of the resonances, however the exact nature of this shift will depend on the resonance itself, the electric field of some modes extending further into the glass than others.

GaP has a large band gap, meaning that absorption is expected to be minimal for light above a wavelength of 548 nm. Thus, the dark field and spatial modulation set-ups are, in principle, measuring the same effect. The results obtained, however, can be very different. By comparing the results to each other, and to the simulation, we can understand more about the measurement techniques and how the substrate affects the nanoparticle measurements. In Figure 4.11, we directly compare the two measurement techniques for two nanorod structures. The TE polarisation and spatial modulation measurements in transmission were selected as these provided the best comparison.

Let us first attempt to identify the features of the measurements by comparing them to the BEM simulation. For the single nanorod, the dark field spectrum in Figure 4.11(a) shows a clear peak at 1060 nm which matches nicely with the b_1^1 mode. Moving to shorter wavelengths, the spectrum is fairly level between 770 and 940 nm. This may be

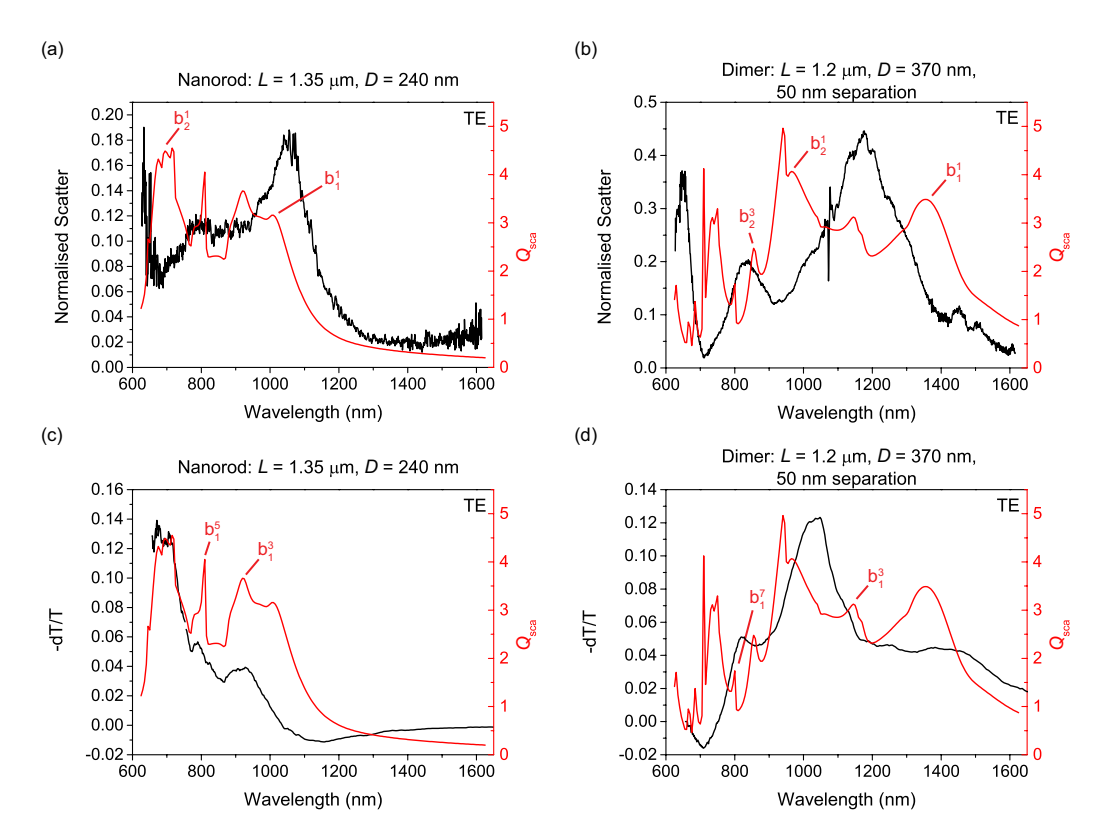


Figure 4.11: The results of the dark field (a, b) and spatial modulation (c, d) measurements (black) are directly compared to the BEM simulated scattering efficiency (red) for two GaP nanorods. (a, c) A single nanorod with a length of 1.35 μm and diameter of 240 nm. (b, d) A dimer with a component length of 1.2 μm and diameter of 370 nm with a separation of 50 nm. All results are obtained for TE polarised light.

the presence of the b_1^3 and b_1^5 modes, however, the two cannot be distinguished. The b_2^1 mode is either very much blue-shifted or, more likely, absent from the sprectrum. The spatial modulation spectrum in Figure 4.11(d), on the other hand, shows two distinct peaks at 790 and 915 nm, albeit with a reduced magnitude, that match well with the b_1^3 and b_1^5 modes. We also see a very strong signal that matches the b_2^1 mode very closely.

We have already examined the dark field spectrum of the dimer in Figure 4.11(b). We determined that the small feature at 1450 nm was likely to be the b_1^1 mode and the much larger peak at 1175 nm corresponds to the b_1^3 mode. The remaining two peaks in this spectrum are likely to be a combination of resonances as the individual modes are densely packed in the simulation. The peak at 830 nm covers the resonant wavelengths of both the b_1^7 and b_2^3 modes while the peak at 650 nm could be the combination of 3 or more resonances.

The spatial modulation spectrum of the nanorod dimer, seen in Figure 4.11(d), is a little more difficult to decipher. We see a peak at 820 nm, similar to the one seen in the dark field spectrum, which covers two cavity resonances. The main feature of the spectrum is a much larger peak at 1030 nm. This peak presents a problem as it does not appear to

be related to any resonance in the simulation. It is located in between the peaks of the b_1^3 and b_2^1 modes. Beyond this, the spectrum is fairly flat between 1150 nm and 1450 nm and then drops off as the wavelength moves further into the infrared. This must be due to the presence of the b_1^1 and b_1^3 modes, but does not allow us to distinguish between them.

While similar features are observed for both measurement techniques, certain resonances are observed in one measurement and not the other. This is the case for both the nanorod and the dimer. For the single nanorod, the b_1^1 mode is present in the dark field spectrum and not the spatial modulation spectrum. For the dimer, it is the b_1^3 mode that is clearly present in the dark field spectrum and not the spatial modulation. On the other hand, the b_2^1 mode is absent in both dark field spectra, while this resonance is clearly visible in the spatial modulation spectrum of the single nanorod and is likely part of the 1030 nm peak present in the spectrum of the nanorod dimer. The cavity resonances $(n \ge 3)$ for both nanoparticles are generally less well defined in the spatial modulation spectra; the magnitude of these resonances appearing to be lower compared to other resonances in the spectra.

This highlights two key differences between the simulation and the measurement. The absence of certain modes in the dark field spectra is likely due to the highly directional nature of the scattered light. The simulation calculates the absolute scattering cross section of a nanoparticle, which is the sum of all light scattered in every direction. The set-up, however, only detects light scattered at a certain angle. The measurement technique is reliant on the limited numerical aperture of the objective so as to not detect light directly from the source.

The other difference is a result of the angular dependence of the nanorod extinction spectrum and the finite numerical aperture of the focusing objective. Both the BEM and FEM simulations assume that the nanoparticle is illuminated by a plane wave, but this is not the case in the spatial modulation set-up. Due to the tight focusing of the light by the objective, the nanoparticle is effectively illuminated by a cone of light. This can lead to the suppression of the expected cavity resonances and introduce new resonances. Let us examine both of these effects in greater detail.

4.4.1 Directional scattering

The highly directional nature of the scattering from certain resonances leads to these resonances being detected in one set-up and not the other. The two techniques are measuring the light at different angles with respect to the input path. The spatial modulation set-up measures light parallel to the input channel, whereas the dark field set-up is estimated to be collecting light at approximately 70° to the input channel.

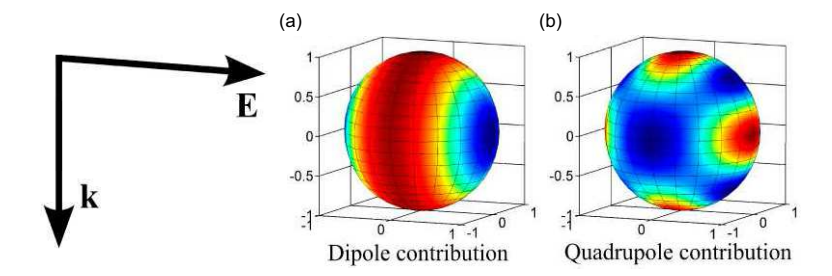


Figure 4.12: Far field scattered intensity profiles calculated from Mie theory for (a) a pure electric dipolar mode and (b) a pure electric quadrupolar mode.¹

Typical far field radiation patterns are seen in Figure 4.12 for a dipolar and quadrupolar resonance. The radiation from a dipolar resonance is equal in all directions orthogonal to the oscillation direction. For the quadrupolar mode, scattering occurs strongly in four lobes; two parallel to the direction of oscillation and one each in the forward and backward directions. This would suggest that the electic dipolar a_1^1 mode under TM polarised light should scatter equally perpendicular to the nanorod axis, but we have already seen that this resonance is not observed in the dark field measurements. Equally, the magnetic dipolar b_1^1 mode should be detectable for TE polarisation and not TM polarisation. The opposite of this was found to be the case, with the b_1^1 mode being much more prominent for TM polarisation.

Evidently there are some factors that complicate this matter. Firstly, these modes are not spectrally isolated and moving, even slightly, away from the resonance can radically change the scattering pattern [67, 101]. A number of studies, for example, have investgated the possibility of preferential forward and backward scattering by use of the Kerker conditions [102–105]. A second issue is that the strongest scattering in a given direction does not necessarily line up with the actual resonance position [106]. The strongest forward scatter from the b_1^1 mode in a sphere, for example, can be red-shifted compared to the strongest backscatter associated with the same mode.

The most crucial issue, though, is the presence of the glass interface [107]. Due to the substrate, the system is no longer symmetric. It is possible for some modes to couple to the surface of the substrate, reducing the scatter in other directions. Interference by light scattered into the substrate and reflected back will also effect the scattering away from the substrate. Predicting the scattering of a particle on the substrate becomes very difficult, making full three dimensional simulations essential.

Thus, to meaure the scattering from the nanorod, the detection channel needs as large a numerical aperture as possibe. In order to truly measure the scattering cross section of a nanoparticle, a different approach is needed. The system would need to be capable of collecting light at all angles, perhaps through the use of an integrating sphere. Otherwise multiple measurements that use different detection angles is the best course of action.

¹Image taken from "Large spectral extinction due to overlap of dipolar and quadrupolar plasmonic modes of metallic nanoparticles in arrays" by Burrows and Barnes [101].

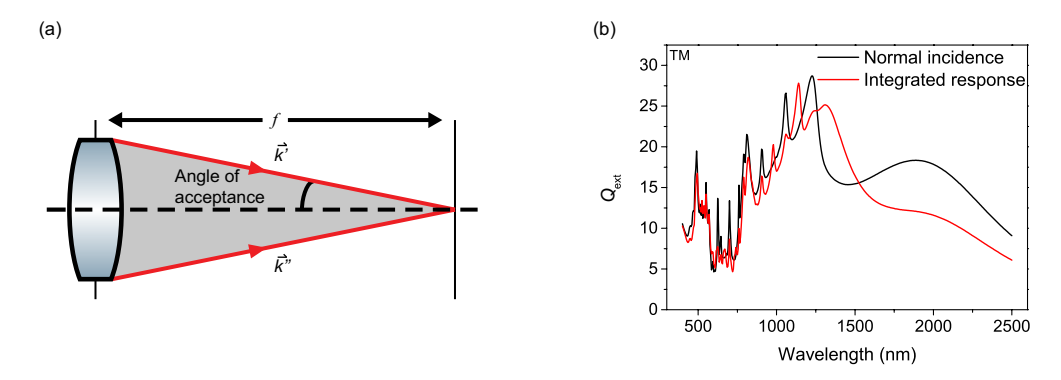


Figure 4.13: (a) 2D diagram showing how light focused by a lens is incident from a non-negligible solid angle. The shaded region indicates all possible angles of incidence between \vec{k}' and \vec{k}'' . (b) Exctinction spectra of a nanorod with a length of 1400 nm and a diameter of 300 nm under TM polarised illumination. In black is the extinction spectrum obtained using only light incident at 90°. In red is the extinction spectrum obtained when the results are integrated over the numerical aperture of the focusing objective.

4.4.2 Angular dependence

Both BEM and FEM simulation techniques assume that the nanorod is illuminated by a plane wave at normal incidence, however, this is not strictly the case with the experiment. Due to the short working distance and finite numerical aperture of the focusing objective, the nanorod is effectively illuminated by a cone of light, with \vec{k} vectors incident from a non-negligible solid angle. This is illustrated in Figure 4.13(a).

We already saw in Chapter 3 that the nanorod's extinction spectrum varies greatly with the angle of incidence. As the angle to the surface is reduced, the odd-order cavity modes are replaced with even-order modes, changing the resonance positions. To account for this, we can integrate the simulated extinction spectra over the numerical aperture of the focusing objective. This gives us a modified extinction spectrum, as seen in red in Figure 4.13(b).

The integrated response has the same overall structure as for a single angle of incidence owing to the fact that the cylindrical modes do not vary by much. The cavity resonances, however, are greatly effected. Those expected for normal incidence become reduced in magnitude and other resonances become visible. Only the lowest set of cavity resonances (the a_2^n modes) remain distinguishable in the case of a 1400 nm nanorod.

The reduction in the magnitude of these cavity resonances is problematic if we wish to observe these modes experimentally. A number of effects that are not considered in the idealistic simulation geometry can contribute to further suppression of the nanorod's cavity modes. Such effects may include a departure from the cylindrical geometry, caused by the crystalline growth of the GaP material, or imperfections and defects that occurred during the growth process. Thus, if one hopes to measure a specific set of

cavity resonances, the input path should have as low a numerical aperture as possible. Furthermore, careful consideration to both odd and even order modes needs to be given if the cavity modes are to be used for practical applications.

4.5 Spatial modulation maps

For the experiments in this chapter, the sample was mounted on a piezo-driven, three axis stage. This allowed for precise optimisation of the particles position with respect to the beam. This also allowed us to image the particle using the spatial modulation signal by scanning the particle position and recording the signal at each coordinate. During the measurements on longer and thicker nanorods, a perculiar result emerged. Exactly four nanorods produced an oscillating dT/T signal as the focus was scanned along their length. This signal was measured multiple times and was reproducible, even after removing the sample from the set-up and then replacing it. Under the SEM, these nanorods show no unique features to distinguish them from other nanorods.

Figures 4.14(a) and 4.14(b) show contour plots of the measured spatial modulation signal as the nanorod is translated by the stage. The 4 μ m dimer shows the results of a "normal" wire; a single optimum position for the best spatial modulation signal. The 16.6 μ m nanowire, on the other hand, is an example of the abnormal measurement seen in only four nanowires out of the thirty-five examined. These abnormal nanowires are longer, but this does not distinguish them from other strucutres that have been successfully measured. Figures 4.14(c), (d) and (e) show a 1D slice through the contour plot at the indicated positions. In the y-direction, the 2f profile typical of our measurements is retained, but in the x-direction we see a signal alternating between 0 and a value around -0.2 for the 16.6 μ m nanowire. Figure 4.14(f) illustrates the relation between the wavelength of the incident light and the peak-to-peak separation of the fringe pattern. As the wavelength increases, so does the peak separation.

The scaling of the oscillation pattern observed for a small subset of wires with the wavelength cannot be directly attributed to a property of the wires. In particular, it should be noted that the illumination is focused to a spot smaller than the nanowire length, therefore the wire is not excited homogeneously over its length and the end facets are not excited when placing the spot in the middle of the wire.

One tentative explanation could be related to the fact that these long nanorods are able to support multiple cavity modes, and that the fringe pattern would be related to the locations of antinodes in the standing wave. If this were the case, however, the peak separation would be much shorter, and a clear coupling mechanism of the localised illumination to these modes is lacking. The effective wavelength of the excitation in the nanorod is reduced compared to the free-space wavelength. The mode index is estimated to be a little over 3 for transverse excitations of such a nanowire [108]. In

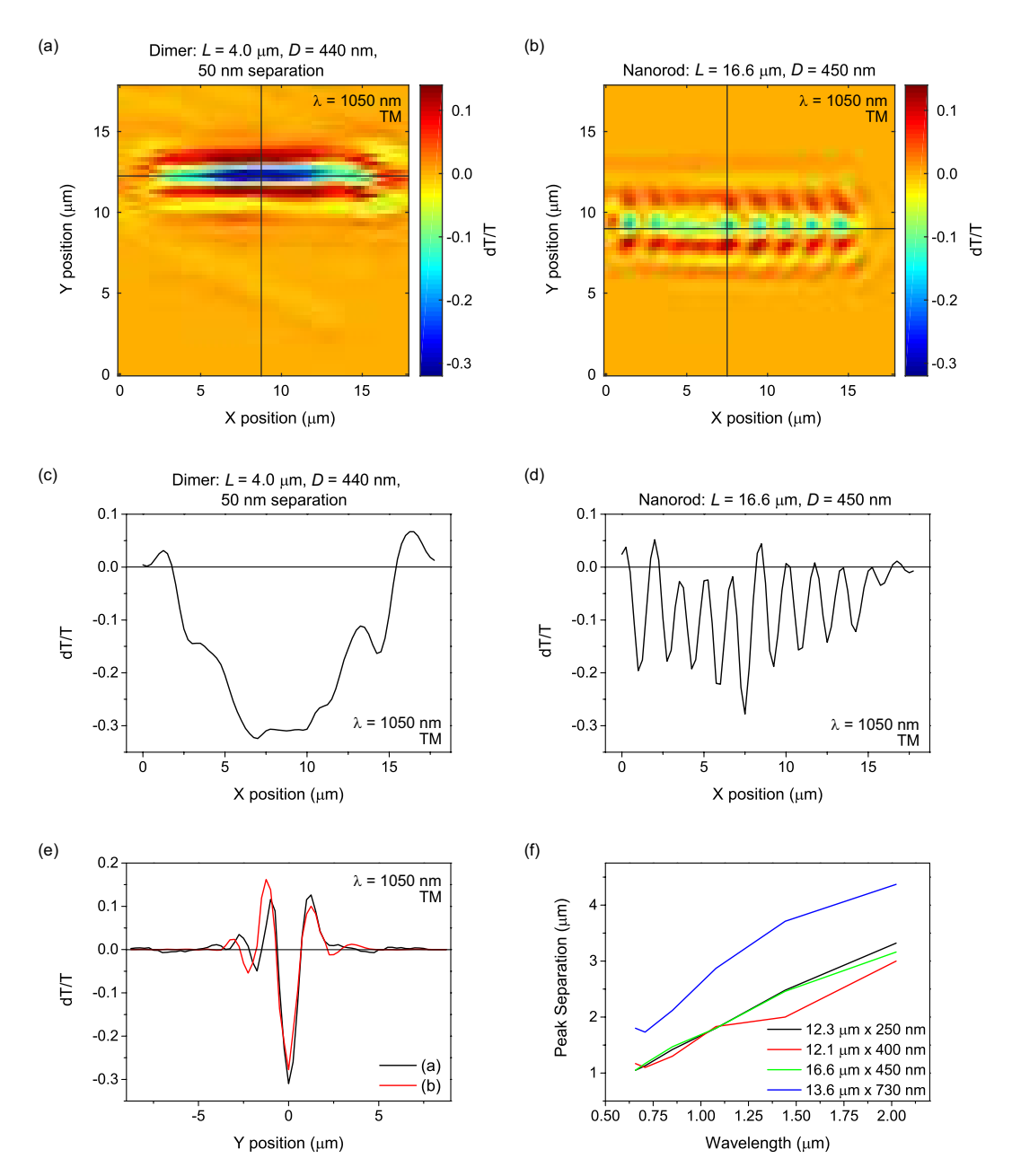


Figure 4.14: Investigation of fringes in the spatial modulation results. Results are shown for a "normal" wire (a, c) and an abnormal wire (b, d). (a, b) A 2D plot of the measured dT/T signal as the nanorod is moved, via a motorised stage, under TM illumination. Translation is in the plane perpendicular to the beam path. (c, d) The signal obtained at a constant y position, indicated by the horizontal line in the 2D plots. (e) The signal obtained at a constant x position, indicated by the vertical line in the 2D plots. (f) A plot illustrating how the peak separation increases with wavelength. The peak separation is the same for both TM and TE polarisation.

addition to this, the distance between antinodes in a standing wave is equal to half the wavelength, meaning the peak separation would need to be at least 6 times shorter than the incident wavelength. Instead, Figure 4.14 shows that, for three of the four nanorods, the peak separation is roughly 1.5 times the incident wavelength. For the 700 nm diameter nanorod, this is even greater.

Without any indication as to why these four nanorods are unique it is difficult to pinpoint the origin of this unusual response. All nanorods used were suitably isolated on the sample surface so that no interaction with adjacent nanorods would skew the results. These nanorods were found in different areas of the sample so it seems highly unlikely that the fringes are a result of interference from nearby on the sample surface. These results are yet to be fully explained.

4.6 Conclusions

In this chapter we have used both dark field and spatial modulation spectroscopy techniques to attempt to measure a nanorod's scattering and extinction cross section. Through both techniques we were able to measure a number of modes that matched what we expected from the BEM simulations. Each technique has advantages and disadvantages and provides vital information of the optical properties of a nanorod in the presence of a substrate. Such information is more practical to applications in photonics devices as a free standing structure is unfeasible in most cases.

In terms of measuring the absolute extinction or scattering cross sections, the measurements suffer from experimental limitations such as the finite numerical aperture of the input and detection channels. Instead, characterisation for practical applications is achieved by a combination of measurement techniques in conjunction with simulated data; the simulations providing the information needed to interpret the physical result.

Chapter 5

Gold Nanoantennas on VO₂ Thin Film

5.1 Introduction

The ability to reversibly switch or tune plasmonic resonant modes at visible and near-infrared wavelengths is highly sort after for numerous applications, particularly for data-storage and telecommunications technologies. The realisation of more complex optical circuits necessitates the development of ultracompact devices capable of controlling and switching light on the nanoscale and with incredibly short response times. Phase-change materials offer a potential solution through the ability to induce a large variation in the dielectric response.

A substantial amount of research has already been done on hybrid devices using a phase transition in conjunction with plasmonic nanostructures. Switchable metal hydride nanostructures have been shown to switch from a metallic to a dielectric state by the absorption of hydrogen [109, 110]. This process is reversible but slow, with complete switching times on the order of minutes. Investigations into gallium have demonstrated that a change in physical state leads to an unusually large change to the dielectric function [111]. A rather low melting temperature of 29.8 °C has seen its use in a metasurface device, switching the reflectivity via optical pumping.

Chalcogenides, in particular germanium-antimony-tellurium (GST), have received significant interest for data storage and memory applications. Switching a GST film from the amorphous to crystalline phase results in a large change in the materials dielectric function [112]. Such a material can be used to modulate an antenna's optical resonance, modifying the resonant wavelength by changing the particle's environment [113]. Modulation can also be achieved optically; the amorphous phase induced using a single, high-energy laser pulse, and recrystalisation achieved via repetetive pulsing at a lower

fluence [114]. The localisation and stability of this optical modulation has lead to its use for near field imaging as well as reversible writing of periodic structures [115, 116]. Combining GST with plasmonic resonators has lead to the development of tunable and switchable perfect absorbers [117].

While chalcogenides can provide a rewritable memory functionality, this typically comes with a relatively high operating temperature (the transition temperature lying at 160 °C). Vanadium dioxide (VO₂), on the other hand, demonstrates a reversible phase transition at only a mildly elevated temperature, normally at around 68 °C. Studies have already shown that this phase transition can be driven in a variety of ways. While it is possible to simply drive the transition thermally, it can also be induced electrically or optically. Optical pumping in particular opens up opportunities for very rapid and localised switching, allowing for the targeting of single devices.

Previous studies have already shown the thermal modulation of the optical resonance for an array of plasmonic structures [118, 119]. Limited optical modulation of a resonant structure has already been investigated using gold and VO₂ nanodisks in close proximity [120]. This device was polarisation selective and the resonance was only modulated for pump polarisation along the dimer axis. Alternatively, the resonance of a gold nanoparticle can be used to drive the VO₂ phase transition [121]

In this chapter, we look at the interaction between an isolated gold nanoantenna and a $\rm VO_2$ film. While the focus is on single antennas, dimer structures were also used. The antennas are designed to have a 200-300 nm particle length and 100 nm particle width, with the dimers having a 50 nm separation. We use both thermal and optical methods of inducing a phase change and examine how each effects the resonance of the gold nanoantennas.

5.2 Thermochromic transition of a VO₂ film

Films of vanadium dioxide are of particular interest as a phase-change material due to its ability to make an insulator-to-metal transition (IMT) at relatively low temperatures. The primary mechanism of the phase transition in VO₂ has been debated for at least four decades [122–128]. Several studies have attempted to classify VO₂, but more recent work has suggested that the IMT is a two stage process, involving mechanisms belonging to two different classes of IMT material [129]. These are the Mott- and Peierls-type transition.

5.2.1 Transition mechanisms

The Mott-transition arises from materials where the highest energy electron orbital is partially filled. According to early models based on non-interacting electrons, such a

material would be a metal, given a suitably small lattice constant. Several such materials, however, were found to be insulating when measured experimentally. These materials were defined as Mott insulators: "an antiferromagnetic material that would be a metal if no moments were formed" [130]. Electrostatic interaction between electrons means that, at low temperatures, an electron that gains enough energy to leave an atom then finds all other atoms to be "occupied". This results in a considerable amount of energy being required to free enough electrons such that movement through the lattice becomes unhindered [131].

The second type of phase transition, the Peierls transition, is caused by a distortion to the lattice structure. In the simplest case of a one-dimensional metal at zero temperature, the presence of an electron-phonon interaction leads to a periodic distortion in the lattice [132]. The atoms in the lattice undergo dimerisation, forming pairs. While this casues an increase in elastic energy in the lattice, this state is energetically favourable as it allows electrons to move to a lower energy state. With the increased distance between atoms and the lowered energy state of the electrons, a band gap is formed. At a finite temperature, however, electrons can be excited across this gap, which screen the electron-phonon interaction. This screening results in a reduction of the magnitude of the lattice distortion such that, at a critical temperature, the band gap collapses and the material becomes a conductor.

While the classification of the IMT in VO_2 has been a controversial topic, more recent studies have at least agreed on the core mechanics. The insulating and metallic phases in VO_2 differ in crystalographic structure, as shown in Figure 5.1. The metallic phase is a rutile tetragonal structure with each vanadium atom being at the center of an octahedron of oxygen atoms. Moving to the insulating phase, the lattice structure becomes monoclinic, with alternating V atoms dimerising. The V atoms then shift as the dimer twists. Associated with this structural change is a splitting of the d_{\parallel} orbital, forming a band gap.

The transition process is more complex, however. This structural change, which would seem characteristic of a Peierls transition, is preceded by a Mott-like electronic transition. It was initially stated by Haverkort $et\ al.$ that the fact that the system is close to a Mott-insulator state is what makes the lattice susceptible to the twisting of V-V dimers [133]. In going from the insulating to the metallic state, studies have shown that an intermediate state occurs resulting in a "monoclinic and correlated metal" phase, forming as nanoscale puddles that grow larger and eventually join together [127, 134]. In going from metallic to insulating states, the same process, rather than the reverse, appears to occur. Chen $et\ al.$ reported that the band gap associated with the monoclinic phase forms in two stages [129]. When the band gap first forms, it has an energy difference of 0.2 eV caused by orbital switching and the V-V dimerisation, which twists slightly. The band gap then widens from 0.2 to 0.8 eV as the twisting angle increases. It would seem, then, that the Peierls transition in VO₂ is always preceded by a Mott transition.

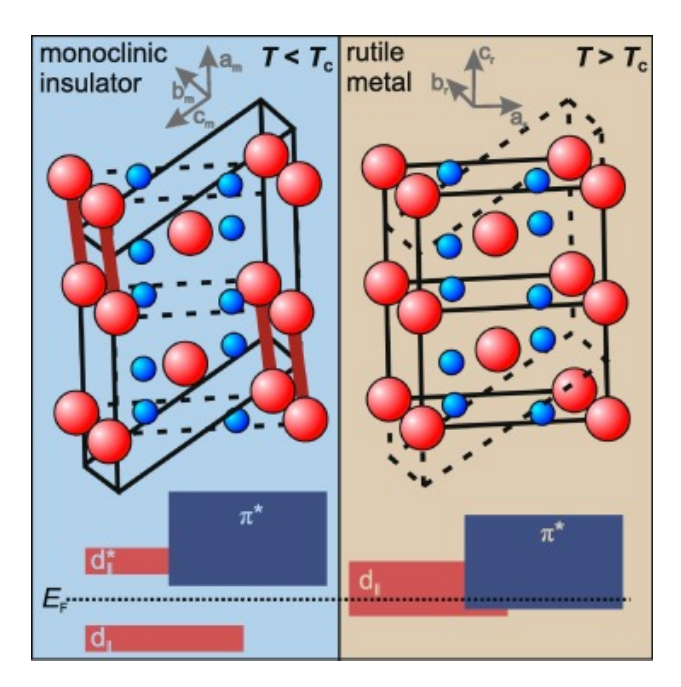


Figure 5.1: Diagramatic representations of the monoclinic insulating phase (left) and the rutile metallic phase (right) in VO_2 . The vanadium atoms are shown as red balls and the oxygen atoms as blue. The unit cell of each phase is indicated by the solid black lines. The bottom schematic shows the difference in electronic band structure in the vicinity of the Fermi level, $E_{\rm F}$.

A number of works have also shown that the phase transition does not have to be driven thermally. While the transition can be induced using a DC current, it has been determined that this process is actually due to Joule heating and is, ultimately, a thermal process [135]. Alternatively, it is possible to induce the phase transition optically. Time domain studies have shown that the change from insulating to metallic phase can be done on a sub-picosecond timescale, suggesting that no thermal process is involved [136]. Infact, it has been determined that the transition as a whole, from monoclinic to rutile lattice structure, occurs on several timescales [137–139]. The initial transition to a conducting phase, caused by screening of the phonon mode and subsequent collapse of the band gap occurs within a few-hundred femtoseconds. This intermediate metallic phase is then "stabilised" by the shift of the V atoms, estabilishing the rutile lattice structure after some number of picoseconds.

5.2.2 Change to the optical properties

In the previous section, we have considered how the structure of VO₂ changes at the atomic level, but this does not immediately reveal how the material reacts to an incoming light wave. For this purpose we consider the dielectric function, $\varepsilon = \varepsilon_1 + i\varepsilon_2$, in which any changes in the materials conductivity will be reflected. The dielectric function

¹Image taken from "Ultrafast dynamics during the photoinduced phase transition in VO₂" by Wegkamp and Stähler [139].

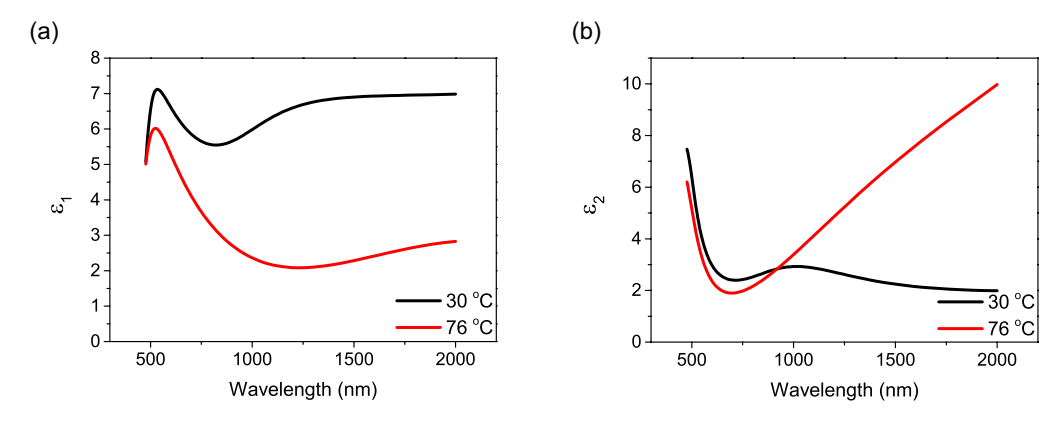


Figure 5.2: (a) Real and (b) imaginary parts of the dielectric function ε of VO₂ at 30 °C and 76 °C, corresponding to below and above the transition temperature.

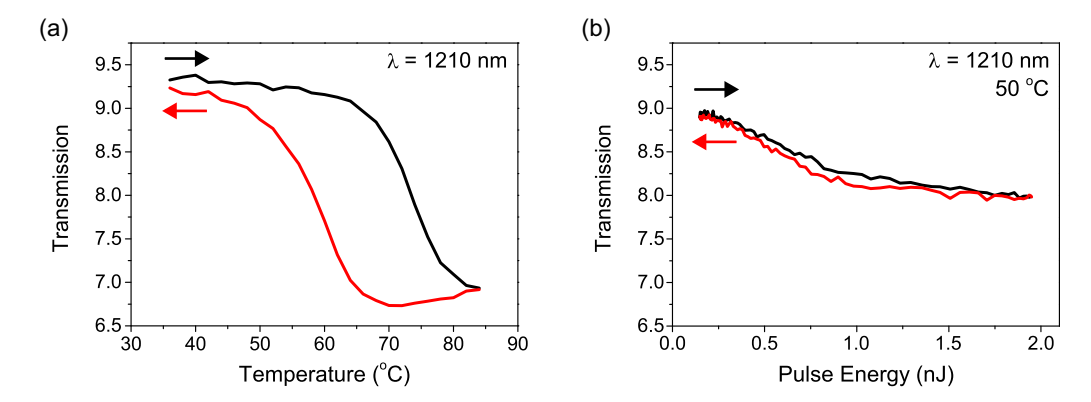


Figure 5.3: Transmission through the VO_2 film measured for a wavelength of 1210 nm while the IMT is induced. (a) The transition is induced by a change in temperature showing a hysteresis loop. (b) The transition is induced by an incident pump pulse, with varying energy, while the sample is kept at a constant temperature of 50 °C. No hysteresis can be seen in this case.

of both phases, calculated from experimental data, has been plotted in Figure 5.2. A large difference can be seen in both the real (ε_1) and imaginary (ε_2) parts of the dielectric function, particularly moving into the infrared spectrum. This is demonstrated experimentally by measuring the transmission through the VO₂ film, shown in Figure 5.3. As can be seen in Figure 5.3(a), VO₂ undergoes a dramatic change between 65 °C and 80 °C, indicated by a large drop in transmission.

A change to a more metallic state is expected to produce an increase in reflectivity and absorption, as the electrons become more mobile and are able to react more to the incident electromagnetic field. This process is observed as a drop in transmission, as the VO₂ transition is induced. Mathematically, the absorption of a material is described by the imaginary part of the permittivity, ε_2 . Figure 5.2(b) clearly shows a large increase of ε_2 at high temperature. For our measurement range of 1100 to 1700 nm, ε_2 is seen to increase by a factor of 2 or more.

Typically for a metal, the real part of the permittivity, ε_1 , is negative. This is clearly not the case for our data on metallic VO₂. This could be due to incomplete switching of the film. It is worth noting that this characterisation was performed at 76 °C, which is significantly lower than temperatures reported previously to be the upper limit of the transition. Qazilbash *et al.* found that the IMT was only complete for temperatures of 360 K (87 °C) and above [134]. The metallic nature of VO₂ is also limited by a low electronic mean free path, which is of the order of the lattice constant. This has been said to be typical of "bad metals" [134, 140–142].

Achieving this transition thermally leads to a the hysteresis effect, which can be an issue for precise or repeated modulation. By instead heating the sample to a point suitably below the threshold, switching can be achieved locally and on an ultrafast timescale. The transition is immediately reversible, as shown in Figure 5.3(b), allowing for a much more rapid transition which we can switch at rates of up to 200 kHz without a thermal buildup. The optical pump appears to have a reduced effect on the sample's transmission. This would seem to indicate incomplete switching of the VO₂, however, experiments on the gold nanoantennas, detailed later, indicate that the VO₂ film is completely switched by pumping with a pulse energy of \sim 1 nJ. This would suggest that there is another factor responsible for the reduced change to the sample transmission. As the pump beam is focussed on the surface of the film, it is possible that the full thickness of the film is not being switched.

5.3 Sample preparation and experimental set-up

The sample used in this chapter is shown diagramatically in Figure 5.4(a). A 30 nm thick layer of fluorine doped tin oxide (FTO) followed by a 50 nm thick layer of VO_2 is deposited on borosilicate glass via atmospheric pressure chemical vapour deposition (APCVD). The FTO is used as a template layer to ensure smooth deposition of VO_2 , rather than V_2O_5 , with a suitable transition temperature. Optimisation of the VO_2 layer was investigated in a collaboration with the University of Salford [47], through which a transition temperature of 68 °C and a surface roughness of less than 10 nm was achieved.

On top of the VO_2 layer, several arrays of gold nanoantennas were deposited, including both single nanorod and dimer structures. This was done using e-beam lithography by my colleague, Yudong Wang. Within the arrays, the nanorod length and dimer seperation were varied, while the width and thickness were kept at 100 nm and 50 nm, respectively. The distance between adjacent nanoantennas in the array was 5 μ m, ensuring that the nanoantennas behaved as isolated structures.

To measure the spectra of the nanorods, the same spatial modulation set-up was used as in the previous chapter, modified to simultaneously act as a pump-probe set-up.

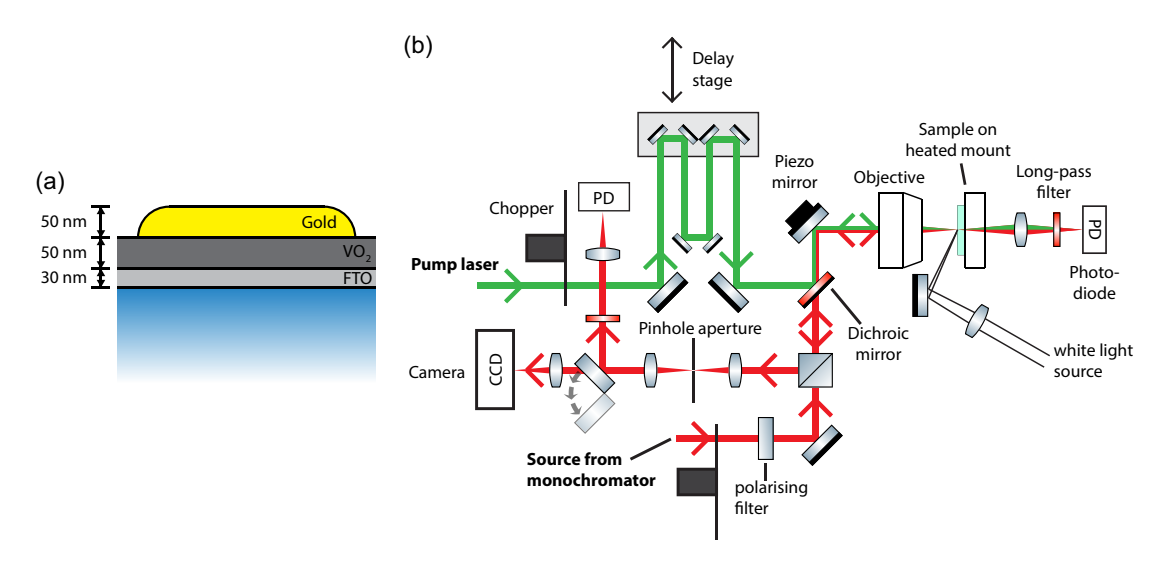


Figure 5.4: (a) Sample structure consisting of a gold antenna deposited on a substrate composed of layers of VO₂ and FTO on top of borosilicate glass. (b)Optical set-up for measuring the spectral response of our gold antennas, comprising spatial modulation and pump-probe techniques. A second, synchronised source is combined with the wavelength tunable measurement beam using a dichroic mirror. Long-pass filters are then used to prevent any signal from the pump beam from reaching the photodetector.

A second high power, synchronised source was brought collinear with the wavelength tunable source using a dichroic mirror which transmits light of 1100 nm and above and reflects light of shorter wavelengths. As can be seen in Figure 5.4(b), the pump beam is introduced just before the piezo-mirror. A series of long-pass filters are used in front of the photodectors to ensure that the pump source does not produce a measureable signal of its own.

In the set-up, a double pass delay line is included so that the relative delay between the pump and the probe pulse can be modified. This consists of two retroreflectors mounted on a motorised stage, allowing the delay to be modified by up to 3 ns with a precision of approximately 15 fs. Varying the delay allows us to measure how the IM transition evolves with time.

5.4 Effect of the IMT on the nanoantenna cross section

It is well established that the resonant wavelength of a nanoantenna is dependent on the refractive index of its surrounding medium [46]. By depositing nanoantennas on a VO_2 film, we gain the desirable ability to modify the resonant wavelength of a single nanoantenna. In Figure 5.5, we demonstrate this for both a thermally and optically induced phase change.

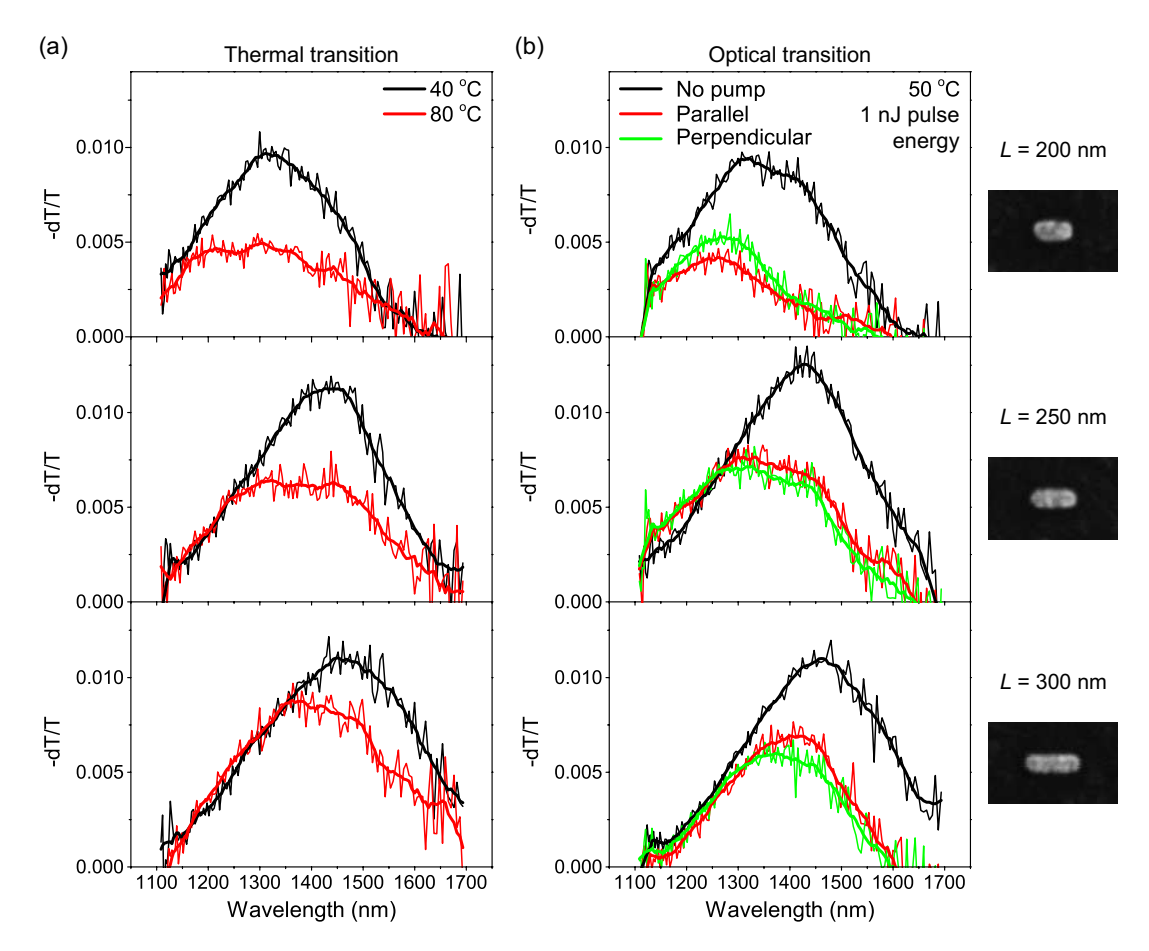
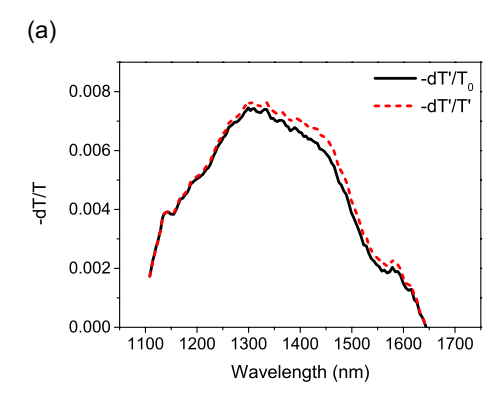


Figure 5.5: Resnance shift in gold nanoantennas of lengths $L=200,\,250$ and 300 nm, induced by modification of an underlying VO₂ film. (a) Thermally induced effect by raising the sample temperature from 40 °C to 80 °C. (b) Optically induced effect by a 1 nJ pump pulse on a film heated to 50 °C.

The spatial modulation spectra of three different sizes of nanoantenna were measured to see the resonance shift induced by both the thermal transition and the optical transition. For the thermal transition, shown in Figure 5.5(a), the spectra were measured with the sample heated to 40 °C and 80 °C, corresponding to temperatures that are suitably below and above the phase transition observed in Figure 5.3(a). For the optical transition, the spectra were all measured at a temperature of 50 °C, just below any notable thermal effect. To achieve the switched state, the sample was locally pumped using a polarised pulse laser at 1060 nm with a pulse energy of 1 nJ. The polarisation was adjusted with a $\frac{1}{2}\lambda$ wave-plate and linear polarising filter, ensuring the power was the same for both parallel and perpendicular beam polarisation.

The phase change in the VO_2 results in a blue-shift of the resonance peak and a reduction of its magnitude. The extent of this effect is the same for both the thermally and optically driven phase transition, as can be seen by comparing Figures 5.5(a) and 5.5(b). From this we can conclude that the pump pulse is achieving complete switching of the VO_2 , despite the reduced change to the sample transmission observed in Figure 5.3(b). It is



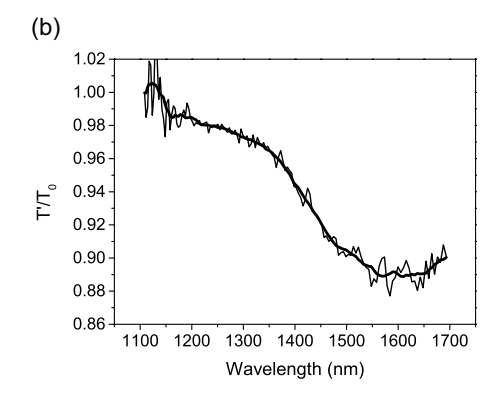


Figure 5.6: (a)Comparison of the shifted resonance signal of a 250 nm nanorod when normalised to the transmission of insulating or metallic VO_2 . (b) Transmission spectrum through metallic VO_2 as a fraction of the transmission through the unmodulated sample.

also notable that the polarisation of the pump laser does not alter the effect of optical pumping, indicating that the change in resonant wavelength is purely a result of non-resonant pumping, primarily due to the insulator-metal phase-shift in the VO₂ film.

To ensure that the change in transmission through the VO_2 film isn't skewing the results, the differential signal was calculated using unmodulated VO_2 and is plotted against the recorded signal in Figure 5.6(a). It is clear that the difference in modulated (T') and unmodulated (T₀) transmission signal is small compared to the antenna modulation. For further comparison, Figure 5.6(b) shows the extent of the modulation as a function of wavelength. Qualitatively, this is what we would expect based on the differences in the dielectric function in Figure 5.2. The reduction in transmission gets larger with increasing wavelength due to the increased modulation in ε_2 .

Dimer antennas were also measured to see how the modulation would effect coupled antennas. It was hoped that increasing the conductivity of the substrate would increase the coupling of the two nanorods and lead to a larger resonance shift. As can be seen in Figure 5.7, this was not the case.

The measurements of the dimer resonance are complicated by the additional degree of error found in the particle separation. This makes the results difficult to interpret. The resonance of the L=200 nm dimer on unmodulated VO_2 , for example, differs between the thermal and optical measurement. With such inconsistencies, it is difficult to draw any conclusions about the dimer structures.

In the case of a thermally induced transition, we observe a greatly reduced shift in the dimer resonance. This could be due to competing effects. It is expected that bringing nanorods into close proximity would produce a red-shift in the antenna resonance [143–145]. If increasing the conductivity in the VO₂ is increasing the coupling of the nanorods, then this effect would be in direct competition with the blue-shift observed for the single nanorods.

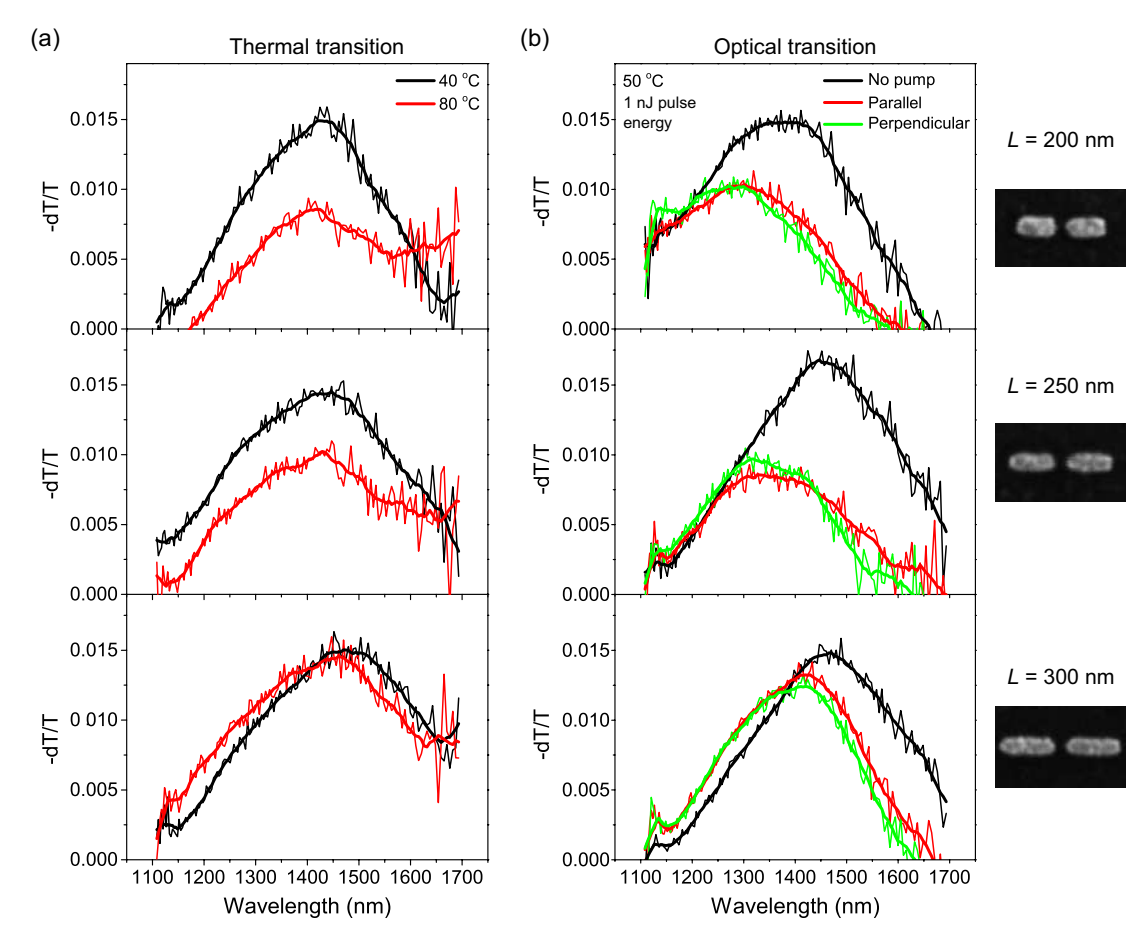


Figure 5.7: Resnance shift in gold nanoantenna dimers with arm lengths of L=200, 250 and 300 nm and a nanorod separation of 50 nm. The shift is induced by modification of an underlying VO₂ film. (a) Thermally induced effect by raising the sample temperature from 40 °C to 80 °C. (b) Optically induced effect by a 1 nJ pump pulse on a film heated to 50 °C.

So far, we have only considered a VO₂ film as existing in one of two states, however, it is evident from Figure 5.3 that the IMT property demonstrates a continuous change from one phase to the other. From this, one would expect to be able to vary the resonant wavelength in a continuous fashion as well. To test this, the spectrum of a 300 nm nanorod was measured while pumping with a pulse energy that was varied from 0.5 to 2 nJ using a continuously variable neutral density filter. The results are plotted in Figure 5.8.

As expected, it is possible to tune the resonance peak of the nanoantenna to any wavelength in the range of 1530 nm to 1340 nm, using a pulse energy of up to 2 nJ. Higher pulse fluences begin to damage the nanoantennas, however, it is clear from Figure 5.8(b) that the VO_2 film is almost completely switched by a 1 nJ pulse and increasing the fluence beyond 1.5 nJ does not achieve any significant further blue-shift.

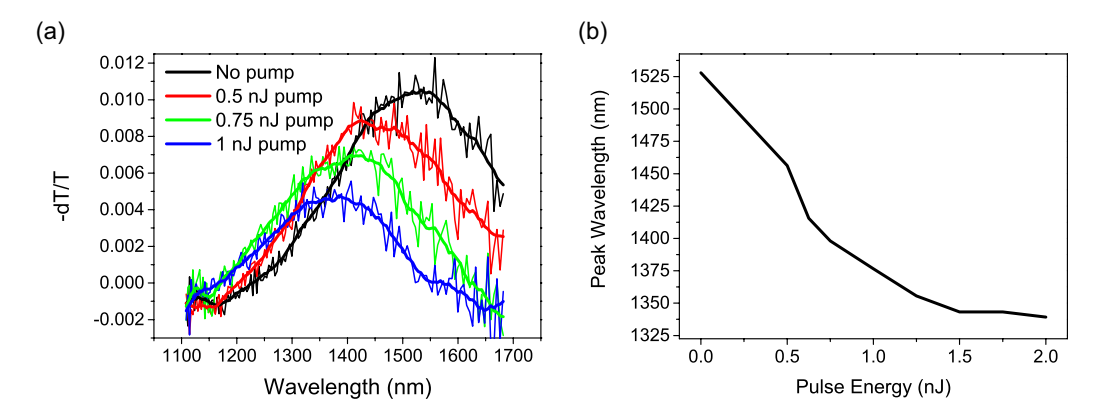


Figure 5.8: Continuous tunability of a gold nanoantenna from $\lambda = 1530$ nm to $\lambda = 1340$ nm by varying the pump power. (a) Spectra of a 300 nm nanorod when pumped with increasing pulse energy. (b) Position of the resonance peak as a function of the pulse energy of the pump laser.

5.5 Pulse energy dependent response

Given the ability of gold nanoantennas to concentrate and enhance the electromagnetic field in nanoscale volumes, one would expect that the presence of gold nanoantennas would increase the pumping efficiency; i.e. lower the pulse energy required to achieve complete switching of the VO₂ to the metallic phase. To investigate this, the response of the nanoantennas was measured at a fixed wavelength near its unmodified resonance while the pulse energy was varied. The results are plotted in Figure 5.9(a). Since each nanoantenna's resonance shows a different magnitude, however, the data was converted to a "relative effect" using each measurements initial and final value, seen in Figure 5.9(b).

The response of the nanoantennas would appear to show a greater relative change for pulse energies of 0.5 nJ or more. The nanoantenna resonance reaches its maximum change at 1.4 to 1.5 nJ, whereas the bare substrate is modified further for a pulse fluence greater than 2 nJ. If the VO₂ film is continuing to show evidence of a transition when the nanoantennas do not, then it seems likely that we are seeing further penetration of the pump pulse, causing a transition for a greater thickness of the film.

To see if the the presence of the antenna changes the response of the VO_2 we need to instead look at the transmission of the probe laser through the sample (the T signal). As the supercontinuum laser power depends on the wavelength, the same normalisation process was applied to the transmission signals as for Figure 5.9(b). The results are plotted in Figure 5.10.

In this case, no notable difference can be seen in the response of the substrate for the different sizes of nanoantennas or in their absence. We can, therefore, conclude that the presence of the nanoantenna does not change the response of the VO₂ and the continuing

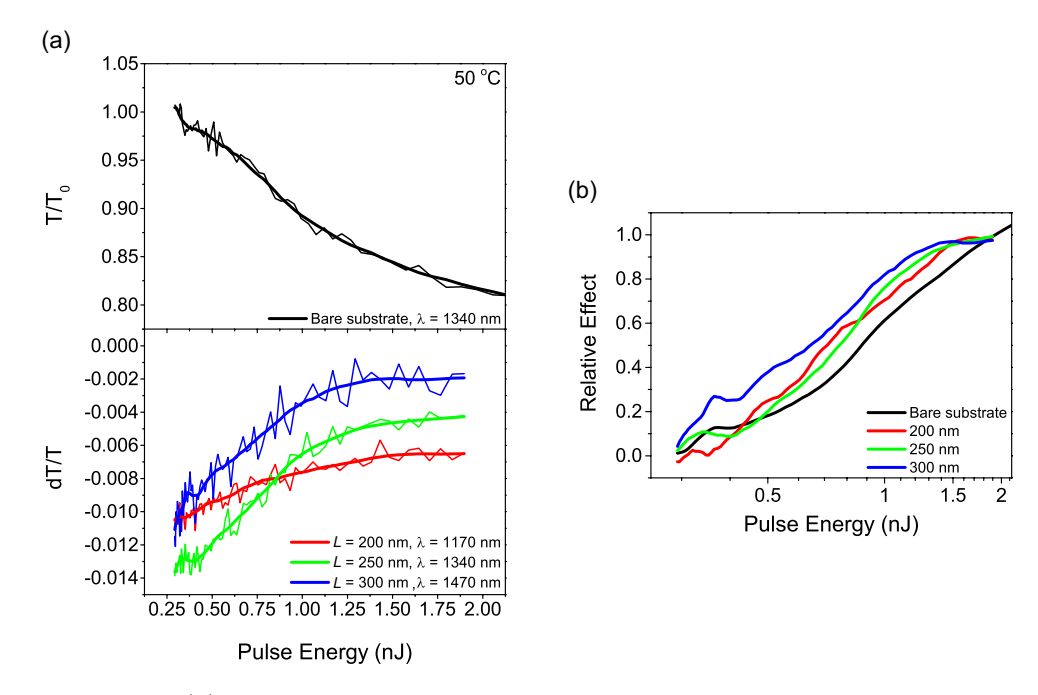
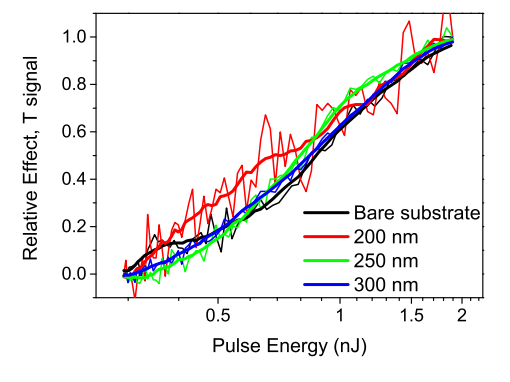


Figure 5.9: (a) Change to spatial modulation signal from nanorods of length L=200, 250 and 300 nm induced by varying pulse energy. Effect is measured at or close to the resonance wavelength. (b) Change in spatial modulation signal normalised to compare relative change.

Figure 5.10: Relative change to transmission through the substrate in the presence of nanorods of length L=200, 250 and 300 nm induced by varying pulse energy. Effect is measured at or close to the resonance wavelength.



change to the laser transmission above 1.5 nJ pulse energy is caused by inducing a phase change in a greater thickness of the VO_2 film.

5.6 Picosecond time response

In an attempt to obtain more information about the VO_2 phase transition, and how it may be modified by the presence of gold nanoantennas, the time evolution of the transition was studied. This is achieved by varying the the relative time delay between the arrival of the pump and the probe pulse. Similar to the power-based measurements, we measure the change to the spatial modulation signal as well as the transmission of the probe beam itself.

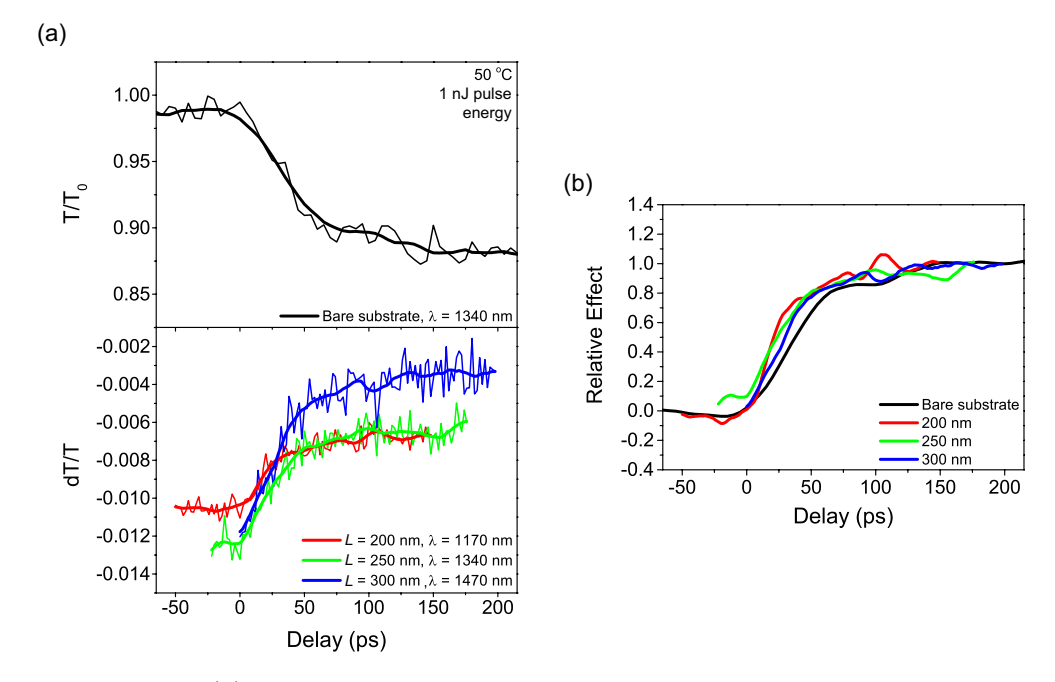


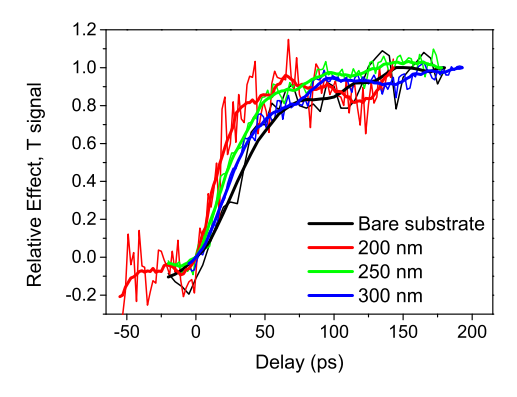
Figure 5.11: (a) Time response of spatial modulation signal from nanorods of length L=200, 250 and 300 nm induced by a 1 nJ pump pulse. Effect is measured at or close to the resonance wavelength. (b) Change in spatial modulation signal normalised to compare relative change.

Due to dispersion in the system, the arrival of the probe pulse, relative to the pump, varies with wavelength. For this reason, the t=0 point of the delay curves had to be adjusted. Once again, the difference in magnitude of the nanoantenna resonances make the initial data in Figure 5.11(a) difficult to interpret. There would appear to be a fast component followed by a continued, gradual reduction in both the sample transmission and the nanoantenna signal. The fast change occurs over the first few 10s of picoseconds after the arrival of the pump pulse, matching the time scale reported for establishing a stable metallic phase. The continuing modulation that follows is likely due to thermal diffusion from the initial pump pulse.

The normalised data in Figure 5.11(b) reveal that the switching of the nanoantenna resonance could be said to be marginally faster than that of the bare VO₂. The transition of the VO₂ film takes approximately 70 ps, whereas the transition in the presence of the nanoantennas is 40 to 60 ps, depending on the length of the nanoantenna. This is surprising, given that the nanoantennas are being pumped off resonance.

To check that this is indeed an effect being induced in the VO_2 and not just the nanoantenna, we again consider the measured transmission through the sample. The results shown in Figure 5.12 present the same effect as seen in Figure 5.11(b). This indicates that the presence of the nanoantenna somehow aids the VO_2 transition. It should be stated, however, that the effect is very small. Further experiments would need to be done, with proper callibration for the temporal dispersion in the system, before a more definite conclusion can be drawn.

Figure 5.12: Relative change to transmission through the substrate in the presence of nanorods of length L=200, 250 and 300 nm induced by varying the delay between pump and probe pulse. Effect is measured at or close to the resonance wavelength.



5.7 Conclusions

We have investigated the insulator to metal phase transition in a thin film of vanadium dioxide and the interaction with light of a gold nanoantenna deposited on top. We showed that complete switching of VO_2 to the metal phase can be achieved in a nanoscale volume via optical pumping, a process which is reversible on an ultrafast time scale. The transition was found to be a continuous process depending on the temperature or pulse energy used, allowing for controllable tuning of a nanoantenna resonance, with a maximum blue-shift of approximately 5% of the initial wavelength.

The primary mechanism that results in the modification of the antenna resonance is almost certainly the phase transition of the VO₂. It is clear that the pump wavelength is wholly off resonance and, as such, there is no significant change made, by the presence of the nanoantenna, to the transition mechanism.

Chapter 6

Gold Nanoantennas on Silicon Waveguide Resonators

6.1 Introduction

Progress in integrated photonics has lead to great advances in low loss, on-chip waveguides. With the ability to create optical circuits using the same technology as traditional CMOS computer chips, we are moving ever closer to all-optical signal processing. Telecommunications signals have been carried by optical pulses for some time, however the data still needs to be converted back to electrical impulses before it can be processed.

One of the challenges in optical signal processing is to rapidly modulate light within the circuit. This could be achieved using electrical phase modulation in a Mach-Zehnder type interferometer but, compared with optical devices, electrical devices can be slow as they are limited by the speed of the electrons in the device. To overcome this, much work has gone into developing devices that are capable of modulating light optically, i.e. controlling light with light. All-optical devices are of interest for processing data streams as repeated conversions between optical and electrical domains can cause latency and increase energy consumption. Ultimately, all-optical switching devices would be capable of processing and routing multiple data streams. Most nonlinear optical materials require extremely strong light intensities to achieve significant optical switching. The use of nanoscale elements to concentrate energy and enhance the light-matter interaction forms a potential strategy to reduce the optical power needed for all-optical devices.

This chapter presents experiments aimed at developing a framework for integrated alloptical devices exploiting coherent absorption by plasmonic nanoantennas. The prinicple of coherent absorption was first proposed by Chong *et al.* as a time reveresed analogue to the laser [146]. By replacing the gain medium of a laser with a loss medium, light that enters the cavity at a resonant wavelength can be completely absorbed. This scheme is

defined as a Coherent Perfect Absorber (CPA) and is an application of "critical coupling" whereby the loss is precisely matched to the rate at which light is coupled into the system [147].

Since the concept was first proposed, CPA devices have gained significant interest. Shortly after proposing the theory, the same group demonstrated the effect experimentally using a silicon wafer in a Mach-Zehnder interferometry set-up, through which they were able to reduce the output of the system to less than 1% of the input power [148]. Several theoretical designs have been put forward for introducing loss in a waveguide. A common feature is a ring-resonator in a SOI rib waveguide, where a CPA can be realised by introducing loss in the ring-resonator [149] or by modifying the phase between two beam paths [150]. A design has also been proposed for use in a plasmonic waveguide, using a pair of metal strips to introduce absorption [151]. Such a device would have a greatly reduced footprint on the order of 100 nm².

An experimental demonstration of CPA in a rib waveguide was recently reported by Rothenberg *et al.* [152]. The design comprised of a "racetrack" resonator (an extension of the ring-resonator) with absorption introduced via Si⁺ ion implantation. The device achieved an extinction of 24.5 dB (output approximately 0.35% of the input power).

In this chapter, we look at the use of a coherent absorber to achieve complete quenching of light within a racetrack resonator device. Gold nanoantennas were deposited at the center of a "figure-of-eight" racetrack resonator such that coherent absorption is achieved for odd or even resonator modes, depending on the position of the nanoantenna. The resonator devices were designed and simulated by Dr. Bruck in a continuation of his published work [153].

6.2 Principles of the rib waveguide

Before examining the design of the device used for our experiments, we introduce some of the features that are employed. The design of these waveguide devices is well established but may be unfamiliar to someone who is not from a silicon photonics background. A waveguide works on the basis of confining light in a high refractive index medium, analogous to an electron in a potential well. In this analogy, materials of a higher index have a lower potential, thus surrounding a higher index medium with materials of lower refractive index creates the potential well. Much like the electron, the confined electromagnetic wave takes the form of discreet solutions (modes). A familiar example of such a waveguide is an optical fibre, which has the higher index core completely encased in the cladding, the radial barrier between materials confining light in two dimensions. A rib waveguide is different in that lateral confinement is not achieved by separate materials of different refractive index but instead by creating a center region with a higher effective index in the vertical direction through etching of a rib into the slab.

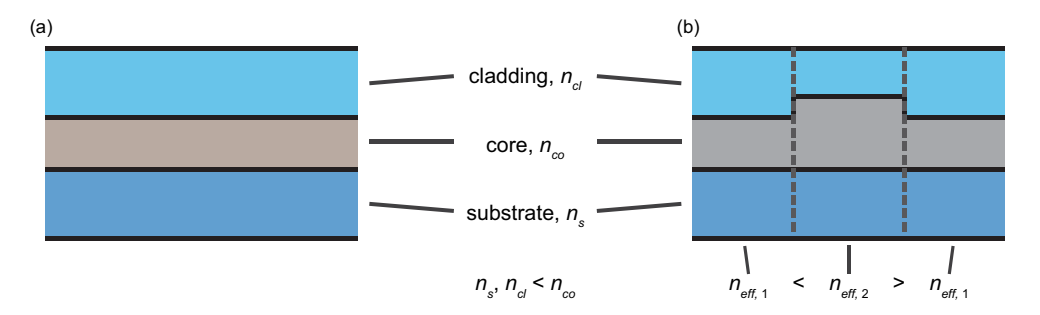


Figure 6.1: (a) A vertical slab waveguide consisting of three layers; the substrate, the core and the cladding. The central core material has a higher refractive index than the cladding and the substrate. (b) A rib waveguide made from the same materials. A central region of the core material is thicker. Dividing the waveguide into three slab regions and assigning each region an effective index, we get a higher effective index in the central region, effectively creating a slab waveguide in the horizontal direction.

Figure 6.1(a) shows the geometry of a slab waveguide, consisting of three uniform layers stacked vertically, with the central layer of a higher refractive index. The slab geometry would allow for vertical confinement within the slab. By completely removing sections of the core layer we could achieve horizontal confinement also, creating a wire waveguide. While desirable from a point of view of mode confinement, wire waveguides are generally more lossy due to issues of fidelity such as side-wall roughness. As an alternative, it is possible to achieve horizontal confinement by only partially etching the core layer. This is described by the effective index method [154, chap. 5, sec. 4].

As is illustrated in Figure 6.1(b), we can divide such a structure into three slab waveguides, with the central slab waveguide having a thicker core. The guided modes allowed in each of these slab waveguides can be assigned an effective index which, for the purposes of this chapter at least, can be thought of as the refractive index of the core adjusted for the part of the electromagnetic field that penetrates into the surrounding layers. The increased thickness of the core in the central region means that any guided mode will penetrate less into the surrounding layer for this region and, thus, the modes of the central slab region will have a higher effective index. Considering the three regions as homogenous layers with a refractive index equal to their effective index reveals the horizontal confinement of the system.

6.2.1 Grating coupler

One of the many techniques for coupling between SOI waveguides and optical fibres is to create a diffraction grating at the end of the waveguide. When a light wave is incident on a grating structure it is diffracted, the number of possible diffraction orders dictated by the grating period and the refractive index of the materials. The diffraction orders are spaced by a "grating vector" which lies in the direction of periodicity and has a

length

$$K = \frac{2\pi}{\Lambda},\tag{6.1}$$

where Λ is the period of the grating. From this, we can derive a coupling condition for an incident wavevector \vec{k}_{inc} at an angle θ from the normal to periodicity [155]

$$|\vec{k}_{inc}|\sin\theta + qK = k_0 n_{eff},\tag{6.2}$$

where q is the diffraction order, k_0 is the free-space wavelength and n_{eff} is the effective index of the waveguide mode. Typically, a small non-zero angle is used as this avoids unwanted back reflections. The above equation is, of course, only valid for a single wavelength device and makes no mention of the coupling efficiency. However, efficient waveguide coupling is not the subject of this thesis. This equation is included to convey the basic idea of grating coupling. Much work has been done to improve the efficient of grating couplers and to make them accepting of a larger bandwidth [156–161].

6.2.2 Directional coupler

A core component of the devices used in this chapter is the directional coupler. This structure allows the transfer of light between adjacent waveguides through evanescent coupling and was first demonstrated by Somekh *et al.* in 1973 [162]. The transfer of light is a cumulative process, thus most designs require a significant interaction length and for light in both waveguides to propagate with the same phase velocity. The easiest way to achieve this is to have two identical waveguides run parallel to each other for the required length.

In the case of two identical waveguides, this coupling mechanism allows complete transfer of light from one waveguide to the other. Throughout the interaction region, incident power oscillates between the two waveguides, thus it is possible to define a beam splitter of any ratio by setting the length of the interaction region. The rate of coupling is determined by the overlap of the evanescent field with the adjacent waveguide mode. The primary factors that effect this are the mode confinement and the separation between the waveguides. A more complete description along with mathematical derivation can be found in [163, chap. 10, sec. 3].

6.3 Device design and experimental set-up

Our device is designed to achieve coherent perfect absorption by interaction of a standing wave with a nanoantenna. The formation of the standing wave is essential as it creates antinodes and nodes, fixed positions where the electromagnetic field is enhanced or cancels out completely. The center of the resonator is unique as the wave at this point

must always be a node or antinode. By placing a nanoantenna on top of this position, we ensure that the nanoantenna is located at an antinode for all odd modes and a node for all even modes within the resonator. This means that for all odd modes of the resonator we should observe CPA while all even modes are unaffected. In terms of a measurement result, this would effectively halve the number of resonances observed in the transmission spectrum.

We also employ a second design which uses two nanoantennas on each resonator section positioned symmetrically about the center of the directional coupler. These are separated such that the nanoantennas are positioned on top of the antinodes of even order modes. In this case, we expect the result to be the inverse of the first design, with even order modes being completely absorbed and odd order modes remaining unaffected. These antinodes of the even order modes shift position, however, so this design will only work within a certain bandwidth.

The standing wave is produced by splitting the incoming light into two paths that couple into a racetrack resonator in opposing directions. The devices used for this experiment were designed by Dr. Bruck, and the complete design can be seen in Figure 6.2. At the core of the design is a figure-of-eight racetrack resonator. This consists of two adjacent resonators with a straight section in the middle to allow cross-coupling between them. The length of this section is such that 100% of the light should be transmitted across the gap. In this way, light which makes a clockwise loop around one resonator will then be transferred to the adjacent resonator where it will make an anti-clockwise loop, hence the figure-of-eight path. The separation between the resonators is 150 nm as this has been found to give the best 100% couplers for the waveguide geometry used and the operational wavelength of 1550 nm.

The standing wave is created by coupling equally into both directions around the race-track resanator. A multimode interference (MMI) slab region couples equally along two waveguide paths that loop back onto each other at the first directional coupler, used to couple light into the racetrack resonator. On the other side of the racetrack resonator is a final directional coupler that allows light to escape to one of two outputs. The outputs were not combined in this design to allow independent measurement of the two channels, and to enable reversal of the input and output (described below). Additionally, keeping the output separate removes any problems with length differences in the output paths due to fabrication errors. In future designs, combination of the two output waveguides into a single output will be relatively straightforward. The separations at the initial and final directional couplers are 200 nm and 240 nm, respectively. These separations are larger than for the center of the racetrack resonator by design, reducing the coupling between the waveguides and allowing for a high quality factor of the resonator.

The etched resonator device can be seen in Figure 6.3. To couple into the waveguide, grating couplers are used at the input and both outputs, an example of which is shown

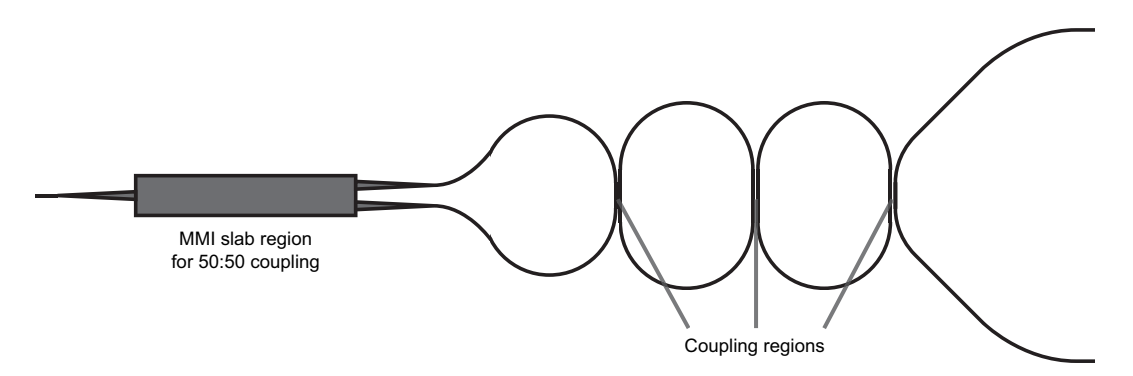


Figure 6.2: Design of the racetrack resonator device. An incident beam is coupled equally into two paths by a multimode intereference region. The two paths lead to the first directional coupler in opposite directions, allowing light to couple into the racetrack resonator in counter-propagating paths and create a standing wave. The central directional coupler transfers 100% of the light resulting in a figure-of-eight path around the racetrack resonator. A final directional coupler allows light to leave the system via two outputs. The input and two output paths connect to grating couplers, seen in Figure 6.3(b), for fibre coupling. The waveguide separation for the directional couplers, from left to right, is 200, 150 and 240 nm.

in Figure 6.3(b). The width at the grating needs to be much wider to accommodate the spot size from the fibre. A taper is included in the design to transition from the grating coupler to the device.

After an initial run of measurements, discussed in the next section, gold nanoantennas were deposited on top of the waveguides at the center of the racetrack resonator. As mentioned above, two designs are used; one with a single antenna on each waveguide at the center of the coupling region, and one with two antennas on each waveguide positioned symmetrically about center of the coupling region. An example of the antennas can be seen in Figure 6.3(c). The antennas are deposited via e-beam lithography using allignment markers located around each resonator design. This process was done by Zondy Webber of the Southampton Nanofabrication Centre.

The experimental set-up is shown in Figure 6.4. The light source is a tuneable laser and detector system which is callibrated and capable of accurately measuring the loss of a system. The laser module and components are designed to be used in conjunction with optical fibres. The output is first directed to a polarisation controller consisting of a linear polarising filter and half-wave plate. This ensures the correct polarisation for coupling into the SOI waveguide. Coupling into and out of the device requires positioning the tip of a fibre over the input and output gratings at an angle of 10° from vertical. Output from the device is coupled back into the measurement system for detection. A junction was added into the system so that the fibre tips at the input and output of the device could be swapped and the direction of light through the resonator reversed. The reason for this will be discussed later.

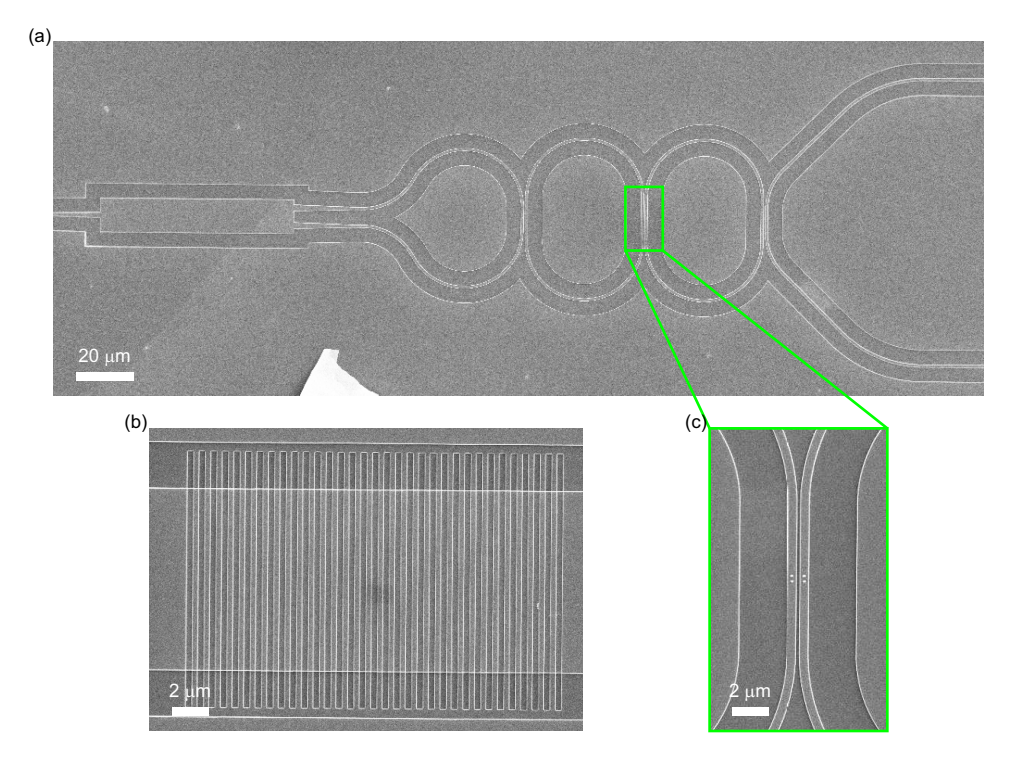


Figure 6.3: SEM images showing (a) the etched device design, (b) an example of a grating coupler, and (c) the position of deposited nanoantennas.

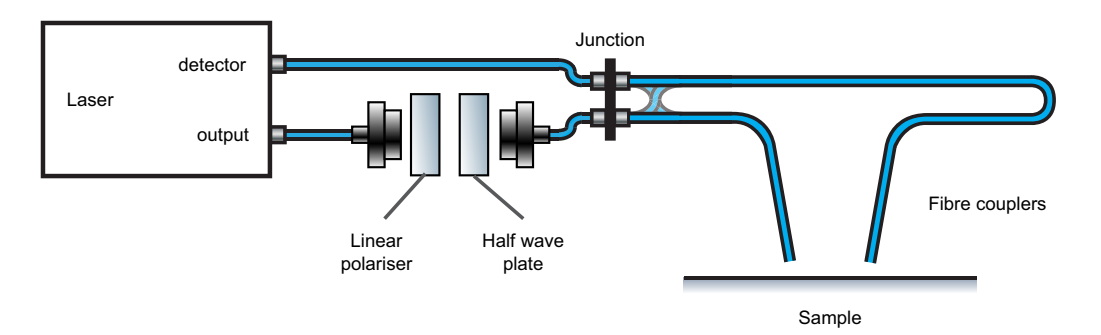


Figure 6.4: The experimental set-up. Light, output from a tunable laser source, is coupled into a fibre and passes through a polarisation controller consisting of a linear polariser and half-wave plate. Light is then coupled into and out of the sample by positioning the fibres, angled at 10° from vertical, above grating couplers. From the output coupler, the light travels back to the measurement system to be detected, allowing loss through the set-up to be measured. A junction coupler is included between input and output fibres to allow direction through the resonator device to be switched.

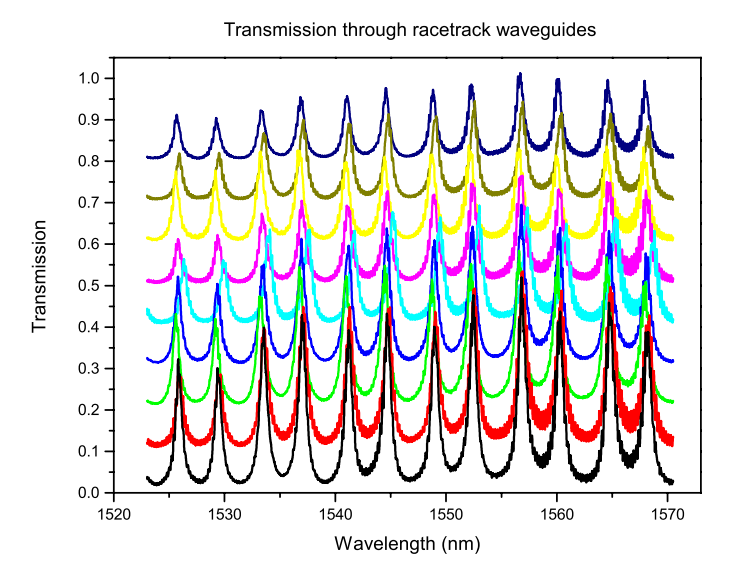


Figure 6.5: Transmission spectra of the racetrack resonator, normalised to the power transmitted through a straight waveguide. Nine spectra measured through different structures of identical design are overlaid, showing precise and reproducible etching of the resonator devices. Spectra are offset vertically by 0.1 with respect to each other to ensure that all are visible.

6.4 The racetrack resonator

The first step was to measure the response of the racetrack resonator devices without nanoantennas. This was to give us a baseline for comparison to the resonator devices with nanoantennas, and eliminate a difference in response caused by differences between resonator devices. The transmission spectra for nine resonator devices of identical design were measured, as seen in Figure 6.5. The spectra are normalised to the transmission measured through a straight waveguide located nearby on the sample. As can be seen, the response of the devices is very consistent in terms of fringe position, with the exception of the middle resonator device (in cyan) which is slightly red-shifted. This demonstrates the excellent reproducibility of the fabrication process.

The peaks in transmission occur when the wavelength of light matches a resonance of the racetrack resonantor, i.e. when the optical path around the resonator is equal to a whole number of wavelengths. The peak-to-peak separation, known as the free spectral range of the resonator, is approximately 3.8 nm.

6.5 The effect of the nanoantennas

After deposition of the nanoantennas on top of the resonator devices, the transmission through the devices was measured once again. In Figure 6.6, the spectra of three devices are plotted, comparing the transmission before and after nanoantenna deposition. We see the same resonance peaks but with a different height profile. In general, it would

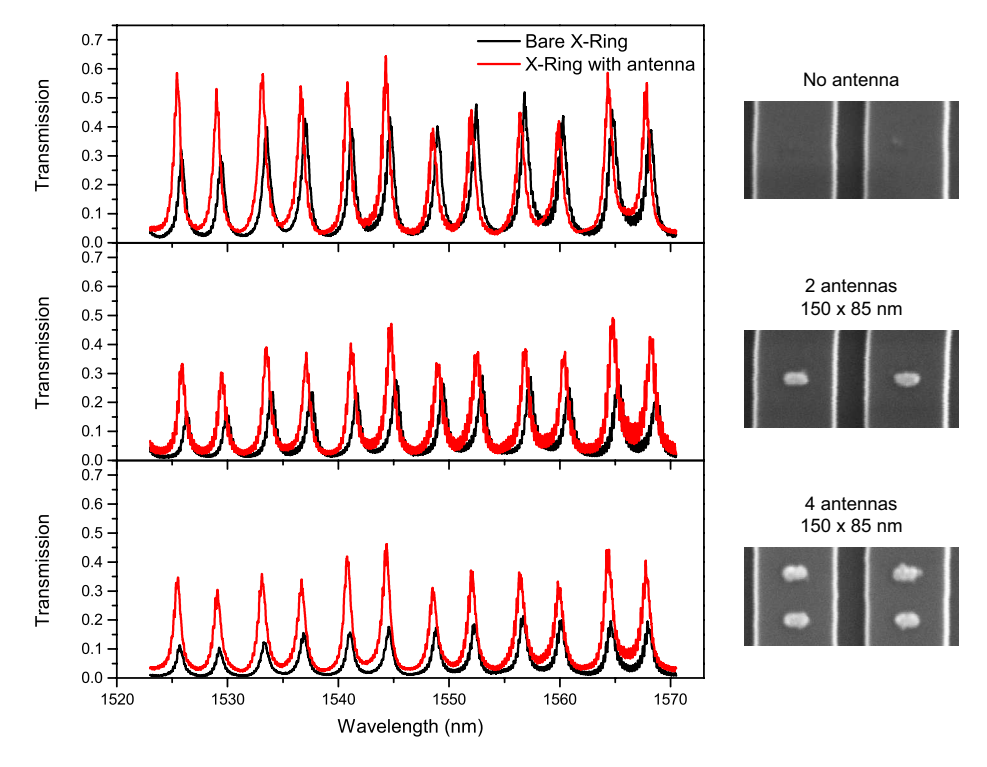


Figure 6.6: Initial measurement of transmission spectra through the resonator devicess before and after antenna deposition. Three different devices are shown; one with no nanoantennas, one with two nanoantennas and one with 4 nanoantennas of the same size. The transmission is normalised to that measured through a straight waveguide.

appear that the presence of the nanoantennas increases the transmission overall, with the result for 4 antennas showing the greatest enhancement over the bare resonator.

The position of the resonance peaks is slightly blue-shifted for all structures. This is a feature of all three spectra and would thus appear to be independent of the presence of antennas. This drift is likely caused by a change in the environment. The relative peak height within each device spectrum does not remain consistent. This must be a result of minute changes to the allignment at the input and output. Apart from the magnitude of the signal, there is no obvious, consistant contrast between a resonator with and without nanoantennas deposited on top. If there is a coherent absorption effect it must be smaller than the differences in magnitude between modes measured in Figure 6.6.

Since the overall transmission varied more than anticipated between the measurements taken before and after the nanoantenna deposition, a new approach was required. To get comparable data sets, transmission measurements were taken in both directions through the resonator device. In the forward direction through the device, the light is split and interferred with itself to create the standing wave required for coherent absorption, whereas going backward through the device results in only a single path being taken and no standing wave formed. Being able to switch the fibres at the junction shown

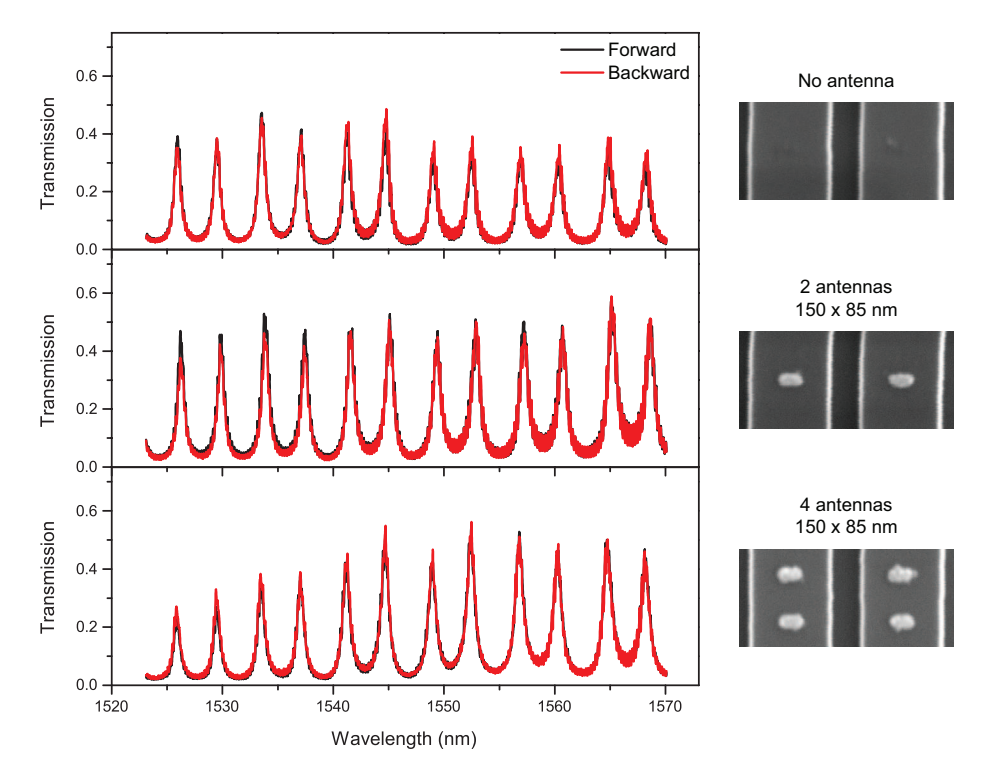


Figure 6.7: Transmission spectra measured forward and backward through the resonator device. The direction through the device is changed by swapping the in-coupling and out-coupling fibre at the the junction labelled in Figure 6.4. Aside from re-optimising the polarisation, the set-up is identical for both directions, ensuring a comparable measurement. The transmission is normalised to that measured through a straight waveguide.

in Figure 6.4 should eleminate any change to the transmission caused by differing fibre allingment. The results are plotted in Figure 6.7

As expected, this technique produces identical results for a resonator without nanoantennas deposited on top. Unfortunately, the same can be said for the other two resonator devices. Coherent absorption should result in a suppression of every other resonance but this is clearly not the case here. It is possible to pick out minute differences in the peak heights, however these do not occur with any regularity.

The next thing to investigate was if the nanoantenna were interacting at all with the light in the waveguide. To test this, we introduced a second laser source and modulated both sources in a pump-probe like experiment. If the light in the waveguide is able to interact with the nanoantenna, the pump laser will induce nonlinear absorption in the antenna which will then affect the second laser pulse. The modulation allows us to directly detect the nonlinear effect increasing our measurement sensitivity.

The modified set-up is seen in Figure 6.8. Each laser passes through a polarisation controller before being combined with a 90:10 fibre tap. The output from this fibre is then connected to the fibre coupling set-up as it was previously. The output coupling fibre is then connected to an InGaAs photodetector, instead of the laser system's inbuilt

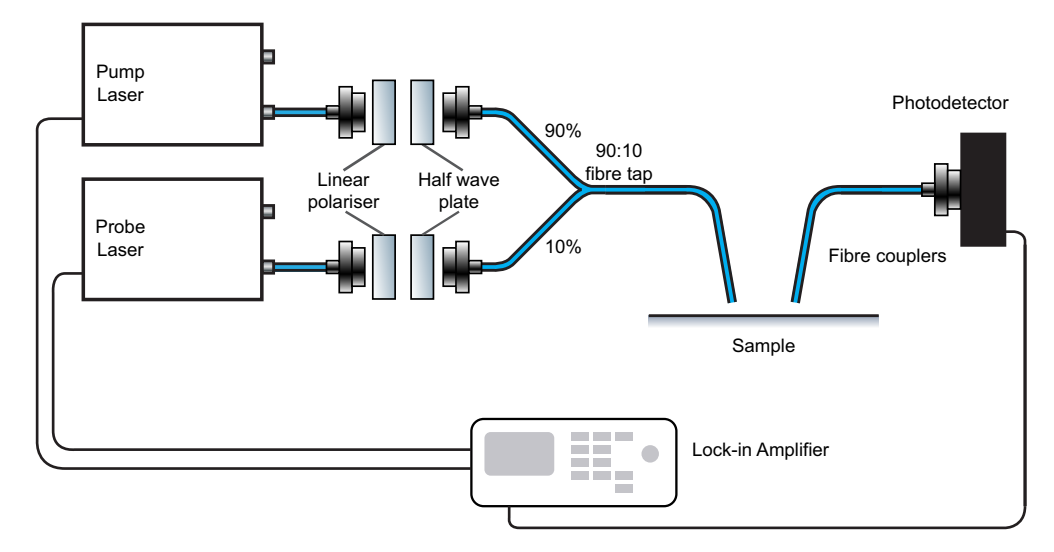


Figure 6.8: The modified experimental set-up. A second laser system is introduced with an additional polarisation controller and the two sources are combined using a fibre tap which couples light in a 90:10 ratio. The 90% branch is used as the pump source, which is varied in wavelength, and the 10% branch is used as the probe source with a fixed wavelength. Both sources are modulated, and the oscillating signals are detected by an InGaAs photodetector in conjunction with a dual reference lock-in amplifier. Signals are detected at the pump and probe frequencies, and at the sum frequency.

detector, so measurements can be taken in conjunction with a lock-in amplifier. Each laser source is internally modulated and the reference signal from each laser system is connected to the lock-in. For the purpose of this experiment, the laser connected to the 90% branch of the fibre tap is defined as the pump beam, and the laser connected to the 10% branch is defined as the probe beam.

The set-up allows us to measure three signals; the power of the pump and probe beams are detected at their respective modulation frequencies, while any cross interaction is detected at the sum frequency of the two modulations. The wavelength of the pump beam is varied while the wavelength of the probe is kept constant at 1549 nm, corresponding to a resonance peak. As the probe power shouldn't change, any signal detected at the sum frequency can be considered to be a modulation of the probe beam caused by the pump beam. This signal is then divided by the measured power of the probe beam to give a "dT/T" result. This has been plotted in Figure 6.9 and compared with the transmission of the pump beam which has, once again, been normalised to the transmission through a straight waveguide.

In this instance we see a clear difference caused by the presence of the nanoantennas. While the single pair of nanoantennas does appear to produce a small modulation, the four nanoantennas are the only combination that shows a quantifiable result. It should be noted, however, that the peak modulation is still only 0.4% of the overall probe power. The modulation for these nanoantennas shows a consistant zero-crossing when

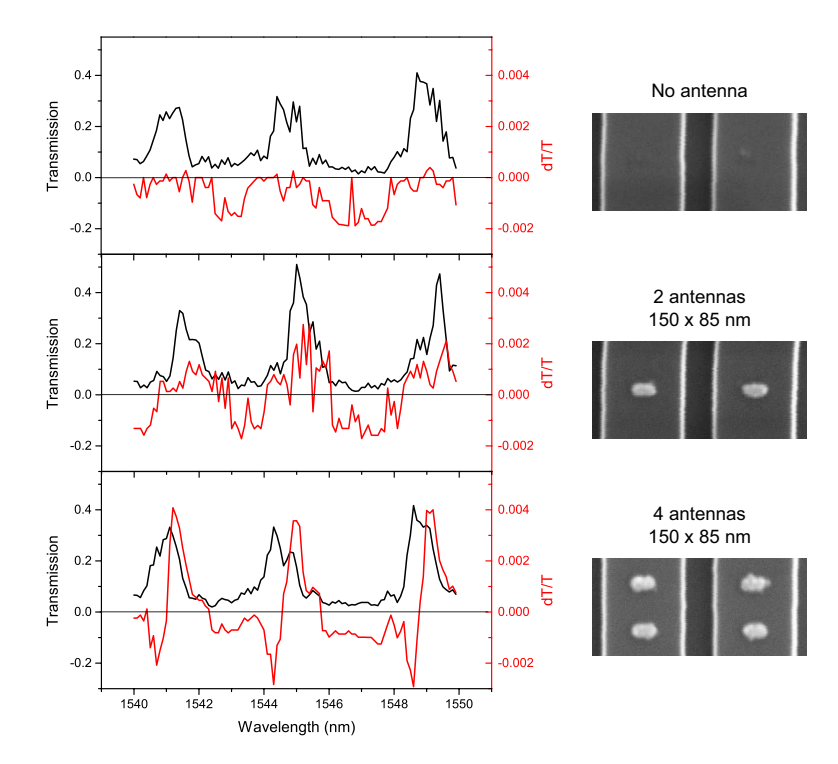


Figure 6.9: Transmision spectra of the pump beam (black) plotted against the relative modulation induced in the probe beam (red). The wavelength of the probe beam is kept at 1549 nm while the pump beam is swept from 1540 to 1550 nm. The transmission of the pump beam is normalised to that measured through a straight waveguide.

the pump laser reaches resonance. The negative trough is smaller in magnitude than the positive peak. This would seem to indicate a small red-shift and an overall increase in transmission. This is consistent with the results seen in Figure 6.6. The resonator with four antennas deposited on top saw the greatest increase in transmission over the bare resonator and, upon closer inspection, the blue-shift that was noted is reduced from 0.4 nm to 0.2 nm.

Evidently, this is not the result of coherent absorption. Not only do the antennas appear to be increasing transmission, the same effect is seen for all resonances. A result arising from coherent interaction would be dependent on the position of antinodes in the standing wave and, thus, would differ between adjacent resonances. This, instead, is likely to be a nonlinear thermal effect. Heating from the gold causes a change to the refractive index of the media, modifying the optical path length around the resonator and, thus, causing a red-shift of the device resonance. The apparent increase in transmission has yet to be explained.

6.6 Conclusions

We have investigated the interaction of nanoantennas with the wave propagating in a racetrack resonator, for use as a coherent absorbing device. We were unable to realise the necessary conditions for coherent perfect absorption, however, we did manage to find evidence of interaction between the guided light and the nanoantennas on the surface. The effect measured was small, showing a modulation of only 0.4% of the probe power.

While this result is not what we were looking for, it at least proves that interaction with nanoantennas deposited on top of a rib waveguide is possible. The design needs to be rethought, but coherent absorption should certainly be possible. The final experiment also serves as a proof of concept regarding modulation of light by light within a resonator device. With further investigation it may yet be possible to achieve all-optical modulation of light in this manner.

Chapter 7

Conclusions

7.1 Summary

In this thesis, we have investigated a number of parameters relating to the control of light by individual nanoantennas. Firstly, we examined the potential of semiconductor nanorods as a low loss alternative of metal nanostructures. Dielectric nanoparticles are capable of achieving large scattering cross sections, similar to metal nanoparticles, but without the loss associated with absorption. By studying the properties of semiconductor nanorods in both the far field and near field we were able to categorise the modes of low aspect ratio structures. The scattering and extinction spectra of the nanorod structures was found to consist of a mixture of two dimensional cavity modes and cylindrical leaky mode resonances.

For resonant applications, such as on-chip optical communication, the resonances need to be tuned in order to optimise the device operation. To this end, we investigated how the resonances of a low aspect ratio GaP nanorod evolved with the nanoparticle's dimensions. We found that the resonant wavelength of the various modes could be, for the most part, predicted by a simple formula based on combining longitudinal cavity modes and cylindrical Mie modes. In addition, we found that a strong enhancement of the electric field could be achieved at the center of a dimer comprised of two nanorods placed end-to-end. While this enhancement is not likely to match that which has been demonstrated with metal nanoparticles, semiconductors could certainly serve as a viable alternative in situations where loss due to absorption in the metal is unacceptable.

Having thoroughly examined the theoretical optical properties of our GaP nanorod structures, we moved to confirm these results experimentally. The theoretical results proved to be not truly representative of the scattering and extinction of a nanorod when placed on a glass substrate. While a number of spectral features could be identified in the experimental measurements, it is clear that simulation or experimentation alone is not

enough to gain an understanding of the nanoparticle's optical properties in situ. Both dark field and spatial modulation measurement techniques have drawbacks in the experimental set-up. The low numerical aperture required by the dark field set-up in order to avoid detecting light direct from the illumination source limits the scattering channels that can be detected. This is a problem for Mie type scatters as the light scattered by certain resonances can be highly directional. The results of the spatial modulation set-up, on the other hand, were skewed by the tight focus of the objective, exciting modes at more than one angle of incidence, and by preferential forward or backward scattering from the nanorod. Thus, a combination of simulation and multiple experimental techniques provides the best opportunity to characterise these nanorod devices. It is also evident that, in using these structures for photonic devices, consideration must be given to the operational angles as this can greatly modify the nanorod's response as well as the strength of the scattered signal.

Returning to metal nanoantennas, we investigated the use of a thin film of VO_2 to modify the optical response of gold nanoantennas. We found that the insulator-to-metal transition of the VO_2 produced a suppression and blue-shift of the single nanorod resonance. The switched VO_2 shifted the resonance by about 5% of the initial wavelength and reduced the peak spatial modulation signal by more than 50%. The modulation at fixed wavelength was found to be as much as 90% of the spatial modulation signal. Complete switching of the VO_2 to the metallic phase can be achieved via optical pumping. This allows for the IMT to be induced in a targeted area in a reversible manner and on an ultrafast timescale.

Finally, we examined the possibility of modulating light within a SOI rib waveguide via a gold nanoantenna deposited strategically on top. While we were not able to achieve modulation in the manner the device was designed for, we were able to demonstrate that coupling of light with the gold nanoantenna does occur. Using a pump-probe experiment, we demonstrated the ability to modulate a carrier signal with a second laser pulse. The device may not have worked as intended, but with further investigation it is believed that this device may provide the first step towards integrated all-optical modulation devices suitable for optical data processing.

7.2 Outlook

The research presented in this thesis is by no means complete. There are a number of opportunities for further investigation. The work in Chapters 3 and 4 serves as a tool kit for a wealth of applications based on semiconductor nanorod devices, from photovoltaics to nanoscale lasers. The characterisation techniques could yet be refined. The dark field set-up could be adapted to use more angles of incidence and cover a larger scattering angle. More advanced dark field systems use a large diameter focusing lens and block

the central portion of the light to produce a ring of light incident at a large angle. A smaller diamter lens is then positioned on the opposite side of the sample in the shadow created by the beam block. Thus the collimating lens only captures scattered light [106, 164]. In addition, further information about the scattering angle could potentially be obtained by imaging in the back focal plane [165, 166]. In such a set-up, an image is created where the distance from the center is associated with the angle at which the light is captured by the collimating lens.

Also of interest would be the nonlinear response of the GaP nanorods. Bulk GaP is known to have a significant nonlinear component [167–169]. Pump-probe could be used to investigate how this modifies the nanorod resonances. Furthermore, it is expected that lifetime measurements would reveal more about the cavity resonances. A number of the cavity resonances were seen to be spectrally narrow in the simulations. One would thus expect these modes to have a high quality factor associated with them.

For the work on gold antennas on a VO₂ film, the next step would be to investigate more complex antenna architectures. The focus in Chapter 5 was on non-resonant pumping. By either tuning the transverse resonance or introducing an additional arm perpendicular to the nanoantenna, resonant pumping could be used, potentially reducing the energy required to switch the primary antenna. With on-chip and chip-to-chip optical communications in mind, other geometries would also be worth investigating. Highly directional emitters, such as the Yagi-Uda antenna [166, 170–172], could lead to more application centered research.

The investigation into the interaction of nanoantennas and light in a waveguide is the first tentative step towards a new type of technology. There are many directions to go. The first is to identify why the device did not work as designed. It is possible that a deviation from the initial design in terms of the size of the antennas, or the waveguides themselves, resulted in greatly reduced coupling efficiency. Research could also be done to investigate the impact of a cladding layer or oxidation layer on top of the device. Beyond this, one avenue of investigation would be to vary the nanoantenna position or even attempt to embed the nanorods within the waveguide. Alternatively, one could investigate the design of the waveguide and whether different combinations of structures could lead to functional optical logic circuits. This would be a significant step towards a light based computer.

Information processing via optical circuitry requires the ability to emit, guide, detect and modulate light. While all of these capabilites have been demonstrated independently, we have yet to see a device that incorporates all these aspects together. There is much more work that needs to be done in order to progress our understanding of these devices to the point that we can combine them together in an efficient manner. The size of commercially viable devices is still bulky compared to state of the art electronics. Miniaturisation

would be a further step required before true photonic-electronic integration becomes possible.

In conclusion, this work is merely a small step towards a wealth of light based technologies. While the research is still very fundamental, it may yet pave the way for photovoltaic and optical circuit devices. It is my belief that the next stage of computer processing will be based on photons rather than electrons but, even so, there will be a large crossover necessitating the use of hybrid electronic and photonic devices.

Appendix A

Additional BEM Simulations of GaP Nanorods

A.1 Extending the simulation to longer lengths

To ensure that we were seeing convergence of the antenna modes with the radial modes of the nanorod, the parameter space was extended to include nanorods with a length up to $2.5~\mu m$. The resulting contour plots can be seen in Figure A.1. We observe that the antenna modes do indeed converge to the transverse modes, as expected, but this not the only notable feature. The transverse modes under TM polarisation show a continuous progression, each fading out to be overlapped by the antenna modes. Under TE polarisation, however, discrete modes are visible.

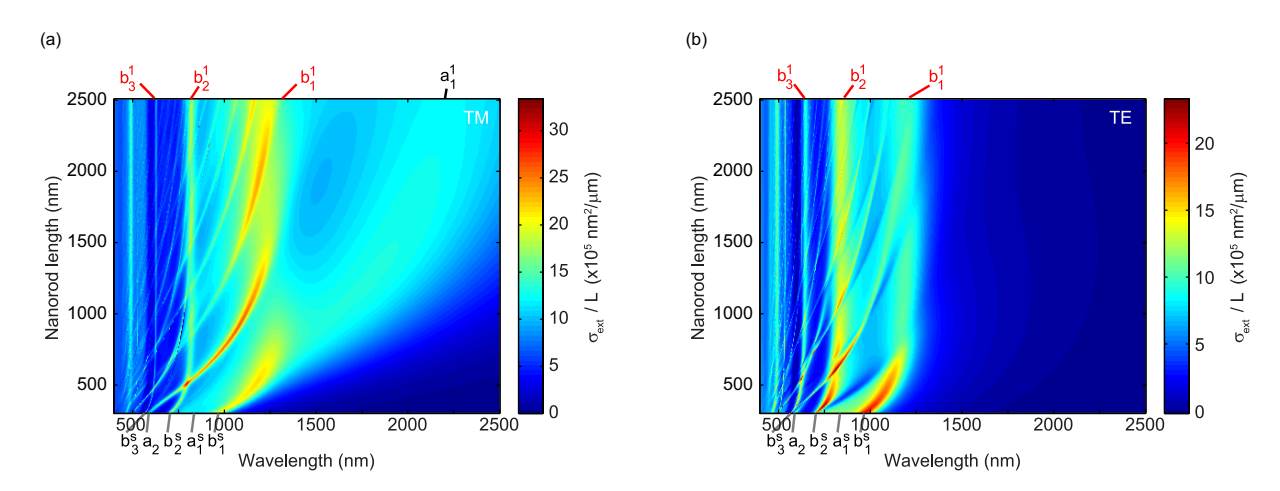


Figure A.1: Extinction spectra obtained under (a) TM and (b) TE polarized light. A nanorod with a constant diameter of 300 nm and a length varied between 300 nm and 2500 nm. The extinction has been normalised to the nanorod length to make the resonances more visible for smaller lengths.

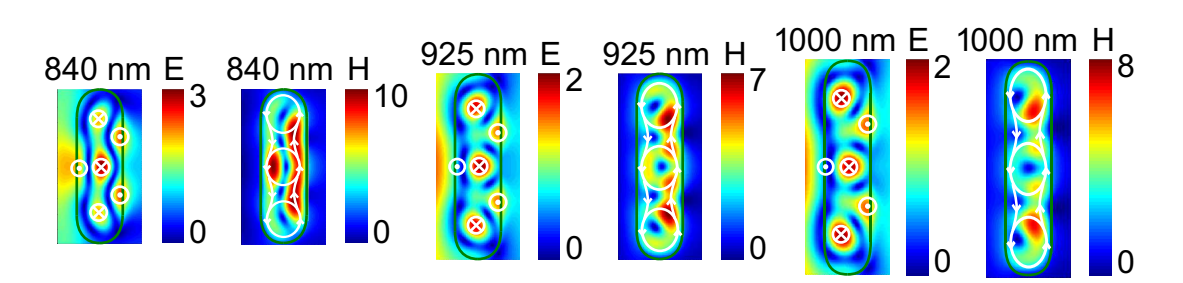


Figure A.2: One branch of the b_2^1 mode in a nanorod of length 1000 nm, 1200 nm and 1400 nm. The resonant wavelength initially matches the TE_{11} infinite wire mode but is shifted as the nanorod is made longer. This branch never crosses the b_1^5 mode.

Both the b_1^1 and b_2^1 mode, under TE polarised light, show an anti-crossing behaviour at regular intervals as the nanorod is made longer. This is most clear in the b_2^1 mode. Initially, this effect would seem to be related to the b_1^n antenna modes but, for longer nanorods, it can be seen that there is no correlation with the crossing points of these modes. The anti-crossing behaviour, then, is a feature of the mode itself, indicating a unique dependence on nanorod length.

The transverse modes are seen to originate from the magnetic Mie resonances meaning that, for TE polarised light, the resonant field is oriented along the nanorod. This being the case, the modes are not simply radial modes and a longitudinal resonance condition is introduced. What is curious is that the mode persists for longer nanorods but has a much lower Q-factor. The near field plots and resonant wavelength for this mode are given in Figure A.2.

A.2 Varying the nanorod diameter

We have studied, in depth, the effect that varying the length of a nanorod has on its extinction spectra. In Figure A.3 we now look at the effect of varying the diameter. As one might expect, based on knowledge of Mie resonances, the nanorod modes have a very strong dependence on the diameter for both TM and TE polarised illumination. We can more clearly see the link between the modes of a nanorod and that of the spherical Mie resonances. It can be seen that the n=3 mode of each resonance originates from one of the spherical modes. For TM polarized light, a_2^3 can be traced to the a_2^s mode and a_3^3 can be traced to the a_3^s mode. Similarly, for TE polarized light, the b_1^s mode can be seen to converge with the b_3^s mode and b_2^s converges with the b_4^s mode.

Creating a dimer structure from two spheres makes a clear change to the extinction spectra. This suggests strong coupling between the particles, as has been seen in previous studies. However, the effect is reduced when deviating from a spherical structure. Figure A.3(c) shows a notable blue shift of the b_1^s resonance, leaving the a_1^s resonance

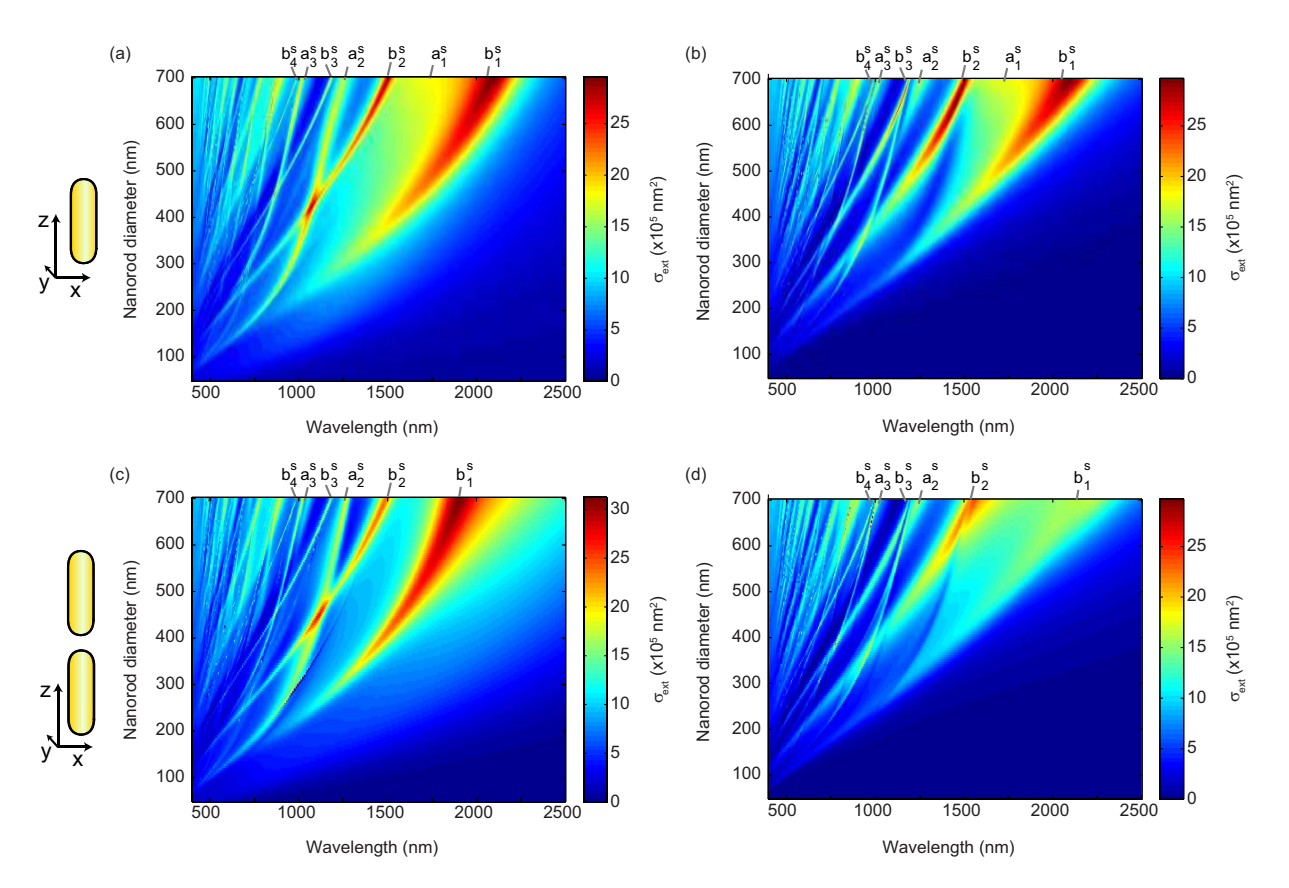


Figure A.3: Extinction spectra obtained under (a,c) TM and (b,d) TE polarized light. (a,b) A nanorod with a constant length of 700 nm and a diameter varied between 50 nm (a high aspect-ratio nanorod) and 700 nm (a sphere). (c,d) Extinction spectra of a dimer structure consisting of two such structures with an inter-particle separation of 20 nm.

indistinguishable. The effect of the second particle is even more pronounced for TE polarization. in Figure A.3(d), the b_1^s , a_1^s and even b_2^s show a notable supression.

A.3 Mode characterization and additional near field profiles

Here, we provide a more complete view of all the nanorod modes discussed in the main text. Each mode identified in the dispersion plots is displayed in Figures A.4-A.7. We start with the Fabry-Pérot (FP) modes for TM polarized light. In Figure A.4, we illustrate the a_2^n and a_3^n modes. The xy cross section through the nanorod is determined by the subscript l, while the number of "rows" of dipoles along the nanorod length is determined by the superscript n. Thus, a_2^5 , as an example, shows a dipolar magnetic field and two opposing electire dipoles in the xy-plane through its center and 5 layers of this pattern along its length.

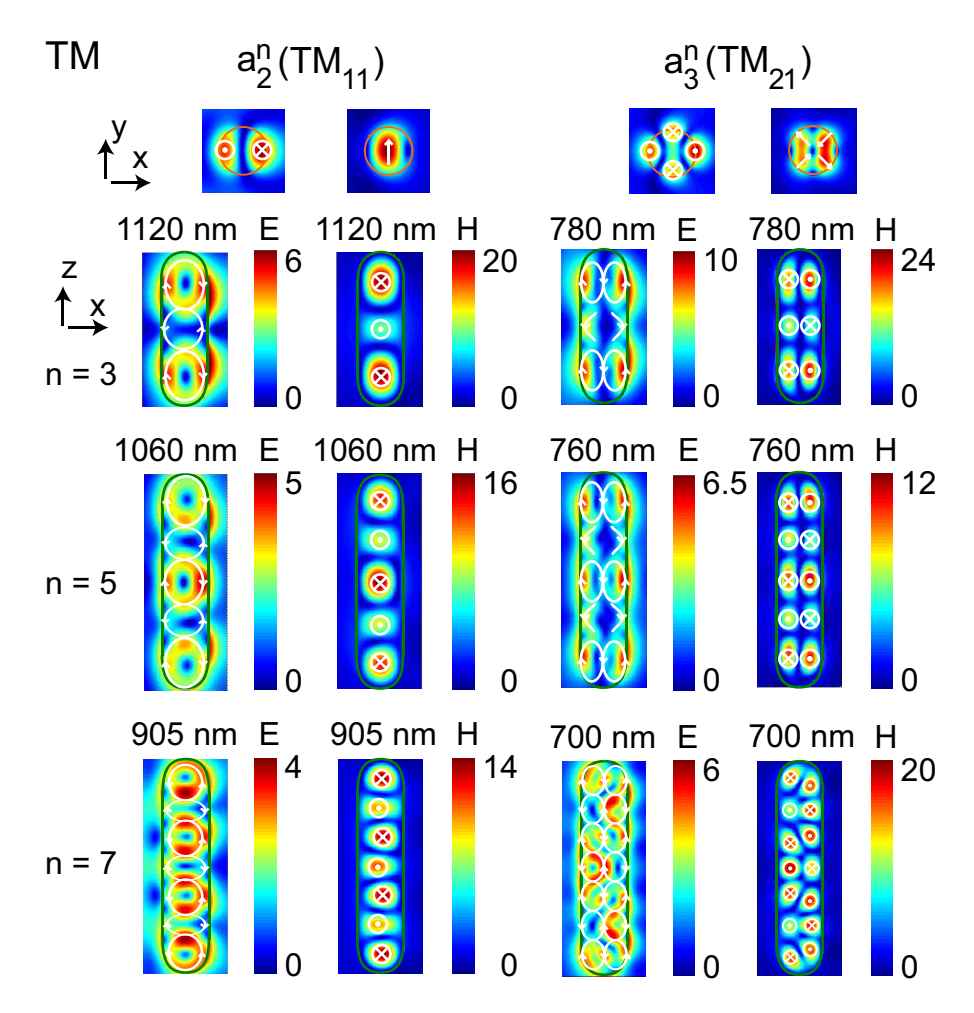


Figure A.4: Near field plots through the center of the nanorod for modes that take the form of a_2^n and a_3^n . The xz plots for n=3 are shown for a nanorod length of 1000 nm and xz plots for n=5,7 are given for a nanorod length of 1400 nm. The resonant wavelength is given above each plot. Typical xy distributions are given at the top of the figure.

In Figure A.5, we see the cylindrical nanorod modes, corresponding to the inifite wire modes that can be calculated analytically. In this case, the near field distribution in the z direction is perturbed as the nanorod is extended. It is for this reason that the resonant wavelength varies very little for nanorods longer than 600 nm.

Turning our attention to the case of TE polarized illumination, we obtain magenetic FP modes. These initially look very similar to the modes in Figure A.4, however, we established in the previous section that these modes originate from the magnetic modes of the sphere. In addition, there is an increased ratio of magnetic to electric field enhancement, i.e. the magnetic field inside the nanorod is found to be even more concentrated for these modes.

Through careful scrutiny of the data, a further family of modes was identified for TE polarized light. Figure A.6 shows the near field plots of b_3^3 and b_3^5 . These modes

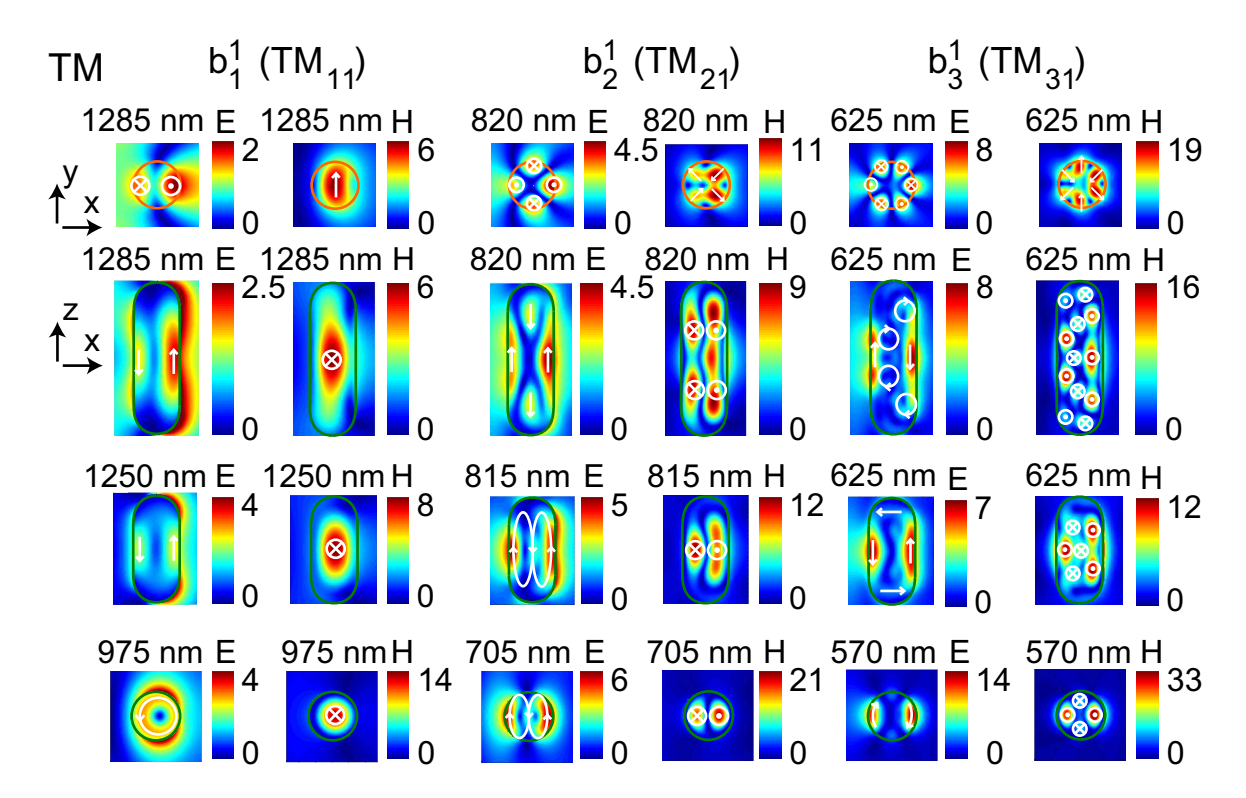


Figure A.5: Near field plots through the center of the nanorod for TM b_l^1 modes. These modes correspond to the modes found in the infinite wire model. The xz plots are given for a 300 nm diameter sphere and nanorods with a length of 700 nm and 1000 nm. The xy plots are given for the 1000 nm long nanorod but are representative of the mode at all lengths.

are characterized by having four magnetic dipoles in the xy cross section and a corresponding quadrupolar electric field distribution. Due to the density of modes at shorter wavelengths, these modes could only be imaged for very particular nanorod lengths.

In Figure A.7, we see the evolution of the infinite wire mode for TE polarization. As discussed above, these are not strictly single modes but represent perturbations of the mode with a stable resonant wavelength.

A.4 Near field enhancement

Here we present a more complete set of data regarding the near field enhancement effects discussed in the main text. In particular, Figure A.8 contains mid-gap field enhancement factors of both the E- and H-field for both TM and TE polarized light. Here we can more clearly see the relation between the enhancement effects and the nanorod resonances. The magnetic field suppression, for example, matches very well to the FP a_2^n modes of the nanorod, seen for TM polarized illumination.

For TE polarized light, we can see that the magnetic field enhancement is clearly associated with the FP b_1^n nanorod modes, as well as the b_1^1 cylindrical mode for shorter

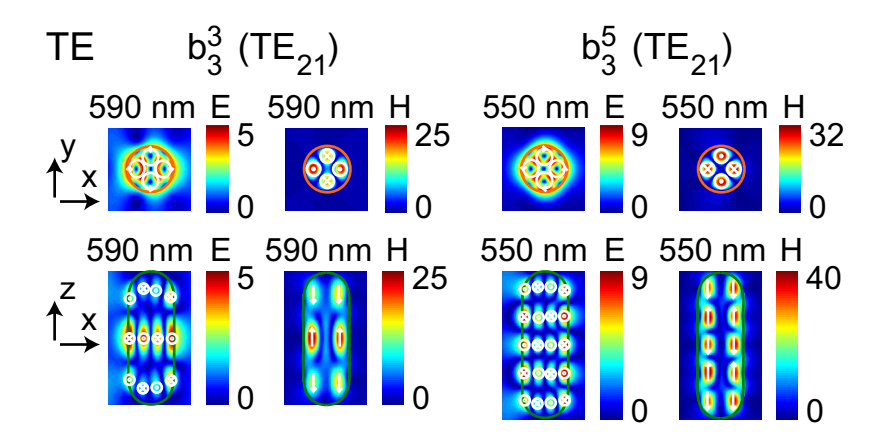


Figure A.6: Near field distributions for the b_3^3 mode in a 880 nm long nanorod and the b_3^5 in 980 nm long nanorod. The different dimensions are necessary due to the density of resonances for shorter wavelengths. Like other mode groups, the xy field distributions are almost identical save for their magnitude.

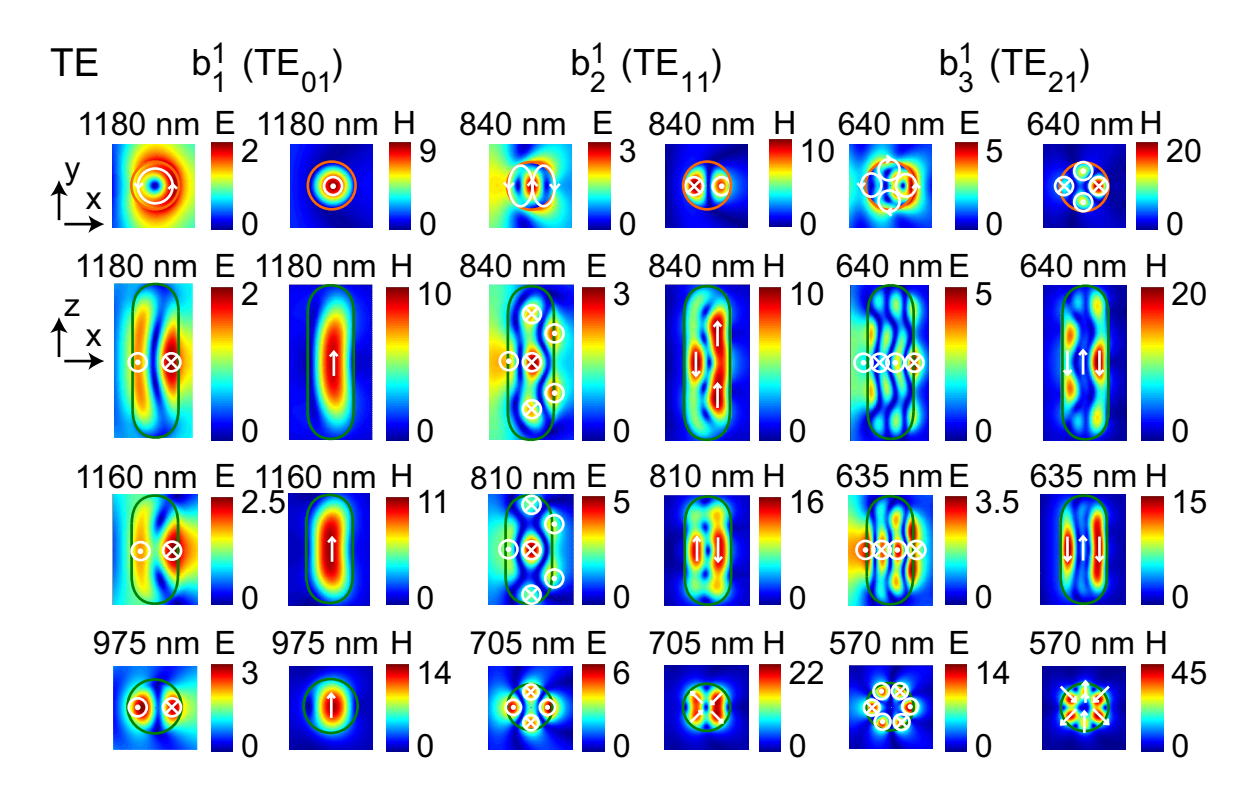


Figure A.7: Near field plots through the center of the nanorod for TE b_l^1 modes. These modes correspond to the modes found in the infinite wire model. The xz plots are given for a 300 nm diameter sphere and nanorods with a length of 700 nm and 1000 nm. The xy plots are given for the 1000 nm long nanorod but are representative of the mode at all lengths.

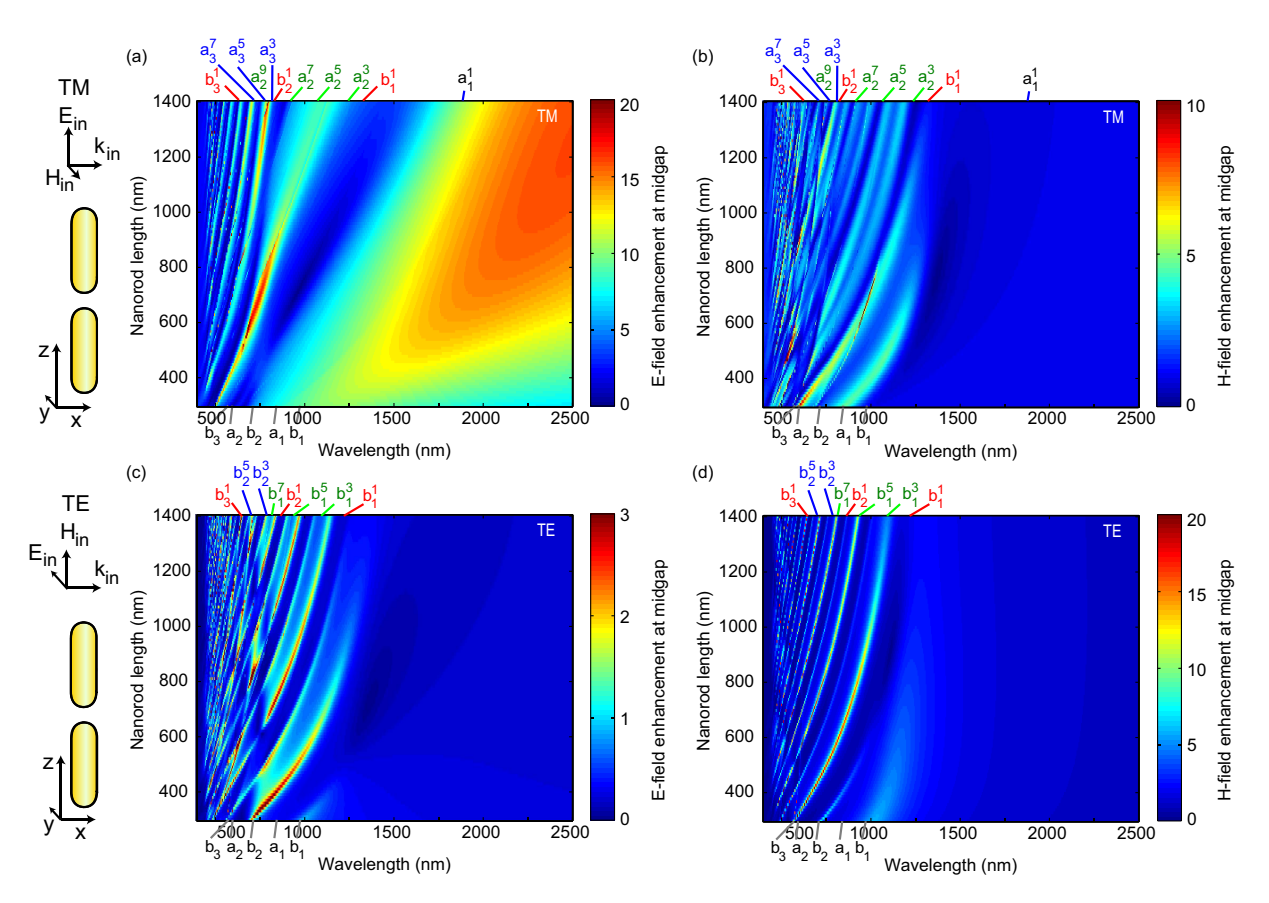


Figure A.8: (a,c) Electric and (b,d) magnetic near field enhancement at the center of a 300 nm diameter nanowire dimer, as a function of nanowire length, for TM (a,b) and TE (c,d) polarized incident light.

nanorods. In Figure A.9, we take a closer look at the near field maps of the corresponding modes. We see that, much like the electric field for TM, these modes have longitudinal magnetic dipoles in phase at both tips of the nanorod. Such magnetic interactions are not prominent for modes where the magnetic field strength is contained further inside the wire, as is the case for the b_1^1 mode in longer nanorods. For b_2^n modes, with opposing dipoles near each tip, we see no enhancement effects, which we attribute to destructive interference of these dipoles.

Single spectra for the case of a single nanorod and a dimer with component length L=1400 nm are presented in Figure A.10. Of particularly interest is Figure A.10(f), not presented in the main text, which shows an enhancement of 2 orders of magnitude in the intensity of the magnetic field for b_1^5 and higher n modes.

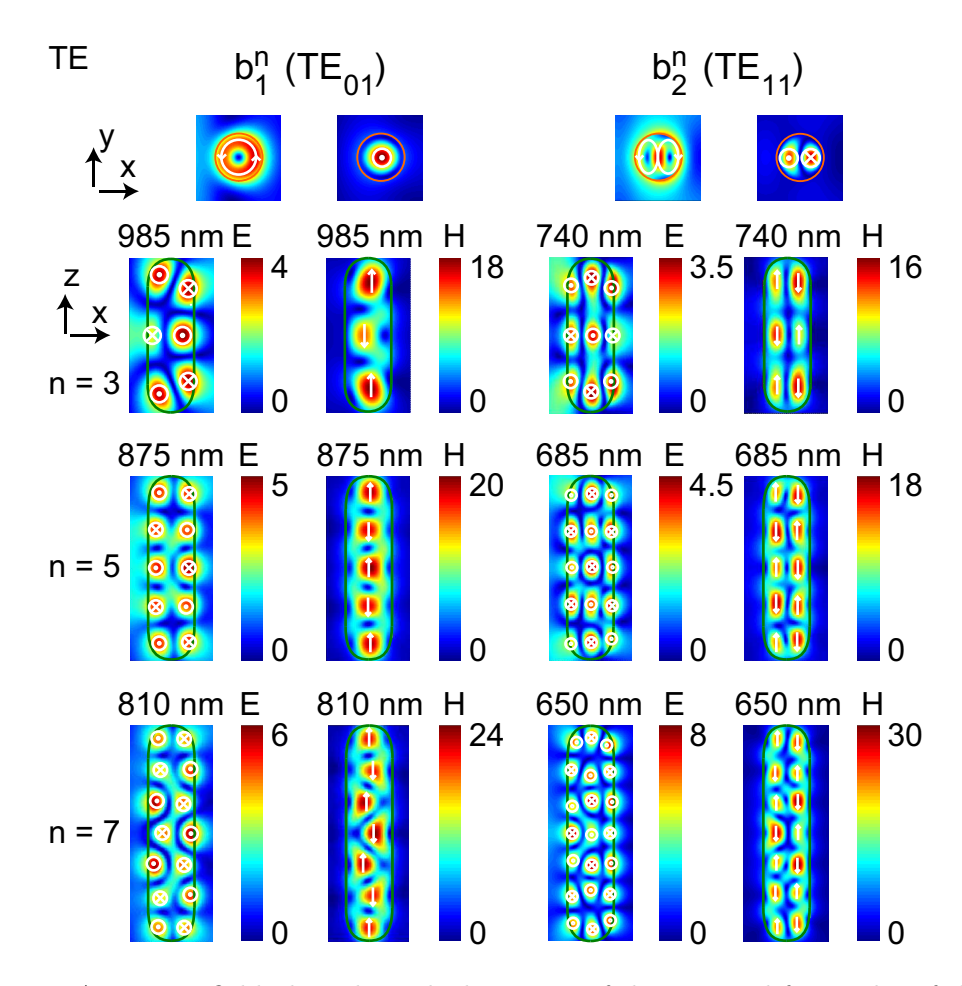


Figure A.9: Near field plots through the center of the nanorod for modes of the form of b_1^n and b_2^n . The xz plots for n=3 are shown for a nanorod length of 1000 nm, the xz plots for n=5 are given for a nanorod length of 1200 nm, and the xz plots for n=7 are given for a nanorod length of 1400 nm. The resonant wavelength is given above each plot. Typical xy distributions are given at the top of the figure.

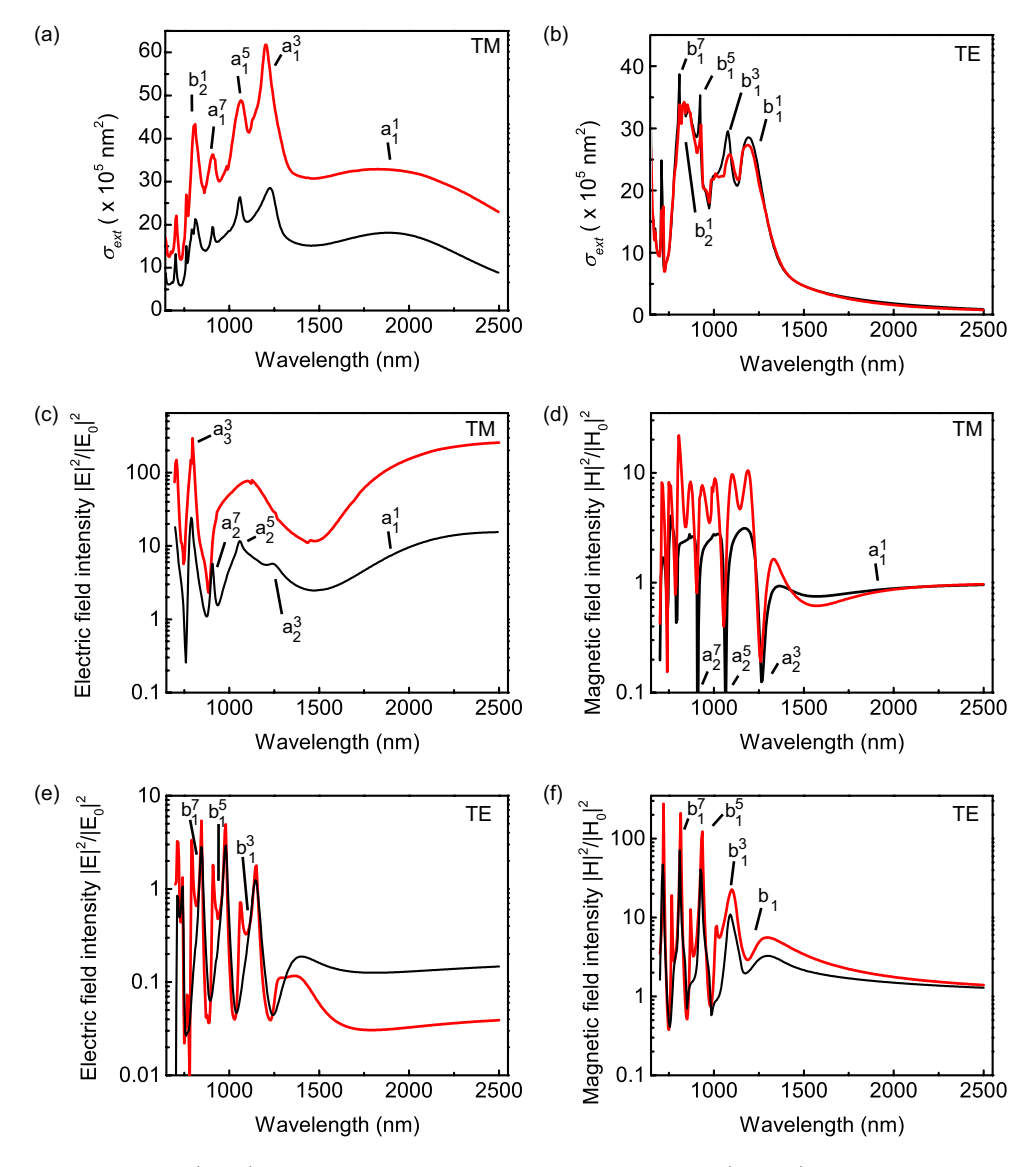


Figure A.10: (a, b) Extinction cross section of nanorod (black), length 1400 nm and diameter 300 nm, and a dimer consisting of two such nanorods (red) for TM (a) and TE (b) polarised illumination. (c-f) Electric (c, e) and magnetic (d, f) near field intensity enhancement for TM (c, d) and TE (e, f) polarised incident light, at the mid-gap of dimer (red) and 10 nm away from the tip of a single L=1400 nm nanowire (black).

References

- [1] D. J. Traviss, M. K. Schmidt, J. Aizpurua, and O. L. Muskens, "Antenna Resonances in Low Aspect Ratio Semiconductor Nanowires," Opt. Express, vol. 23, no. 17, pp. 22771–22787, 2015.
- [2] M. Faraday, "The Bakerian Lecture: Experimental Relations of Gold (and Other Metals) to Light," *Philos. Trans. R. Soc. London*, vol. 147, pp. 145–181, 1857.
- [3] G. Mie, "Beiträge zur Optik trüber Medien, speziell kolloidaler Metallösungen," Ann. Phys., vol. 330, no. 3, pp. 377–445, 1908.
- [4] K. R. Catchpole and A. Polman, "Plasmonic solar cells," Opt. Express, vol. 16, no. 26, pp. 21793–21800, 2008.
- [5] H. A. Atwater and A. Polman, "Plasmonics for Improved Photovoltaic Devices," *Nat. Mater.*, vol. 9, no. 3, pp. 205–213, 2010.
- [6] M. Law, L. E. Greene, J. C. Johnson, R. Saykally, and P. Yang, "Nanowire Dye-Sensitized Solar Cells," Nat. Mater., vol. 4, no. 6, pp. 455–459, 2005.
- [7] B. Tian, X. Zheng, T. J. Kempa, Y. Fang, N. Yu, G. Yu, J. Huang, and C. M. Lieber, "Coaxial Silicon Nanowires as Solar Cells and Nanoelectronic Power Sources," *Nature*, vol. 449, no. 7164, pp. 885–889, 2007.
- [8] E. C. Garnett and P. Yang, "Silicon Nanowire Radial p-n Junction Solar Cells," J. Am. Chem. Soc., vol. 130, no. 29, pp. 9224–9225, 2008.
- [9] L. Tang, S. E. Kocabas, S. Latif, A. K. Okyay, D.-S. Ly-Gagnon, K. C. Saraswat, and D. A. B. Miller, "Nanometre-scale germanium photodetector enhanced by a near-infrared dipole antenna," *Nat. Photonics*, vol. 2, no. 4, pp. 226–229, 2008.
- [10] M. W. Knight, H. Sobhani, P. Nordlander, and N. J. Halas, "Photodetection with Active Optical Antennas," *Science*, vol. 332, no. 6030, pp. 702–704, 2011.
- [11] P. Servati, A. Colli, S. Hofmann, Y. Q. Fu, P. Beecher, Z. A. K. Durrani, A. C. Ferrari, A. J. Flewitt, J. Robertson, and W. I. Milne, "Scalable Silicon Nanowire Photodetectors," *Phys. E*, vol. 38, no. 1-2, pp. 64–66, 2007.

[12] S.-K. Kim, R. W. Day, J. F. Cahoon, T. J. Kempa, K.-D. Song, H.-G. Park, and C. M. Lieber, "Tuning Light Absorption in Core/Shell Silicon Nanowire Photovoltaic Devices Through Morphological Design," *Nano Lett.*, vol. 12, no. 9, pp. 4971–4976, 2012.

- [13] S.-K. Kim, K.-D. Song, T. J. Kempa, R. W. Day, C. M. Lieber, and H.-G. Park, "Design of nanowire optical cavities as efficient photon absorbers," ACS Nano, vol. 8, no. 4, pp. 3707–3714, 2014.
- [14] P. Fan, U. K. Chettiar, L. Cao, F. Afshinmanesh, N. Engheta, and M. L. Brongersma, "An Invisible Metal-Semiconductor Photodetector," *Nat. Photonics*, vol. 6, no. 6, pp. 380–385, 2012.
- [15] O. Hayden, R. Agarwal, and C. M. Lieber, "Nanoscale avalanche photodiodes for highly sensitive and spatially resolved photon detection," *Nat. Mater.*, vol. 5, no. 5, pp. 352–356, 2006.
- [16] M. H. Huang, S. Mao, H. Feick, H. Yan, Y. Wu, H. Kind, E. Weber, R. Russo, and P. Yang, "Room-Temperature Ultraviolet Nanowire Nanolasers," *Science*, vol. 292, no. 5523, pp. 1897–1899, 2001.
- [17] J. C. Johnson, H.-J. Choi, K. P. Knutsen, R. D. Schaller, P. Yang, and R. J. Saykally, "Single gallium nitride nanowire lasers," *Nat. Mater.*, vol. 1, no. 2, pp. 106–110, 2002.
- [18] X. Duan, Y. Huang, R. Agarwal, and C. M. Lieber, "Single-nanowire electrically driven lasers," *Nature*, vol. 421, no. 6920, pp. 241–245, 2003.
- [19] M. A. Zimmler, J. Bao, F. Capasso, S. Müller, and C. Ronning, "Laser action in nanowires: Observation of the transition from amplified spontaneous emission to laser oscillation," *Appl. Phys. Lett.*, vol. 93, no. 5, p. 051101, 2008.
- [20] A. V. Maslov and C. Z. Ning, "Far-field emission of a semiconductor nanowire laser," *Opt. Lett.*, vol. 29, no. 6, pp. 572–574, 2004.
- [21] I. Friedler, C. Sauvan, J. P. Hugonin, P. Lalanne, J. Claudon, and J. M. Gérard, "Solid-state Single Photon Sources: The nanowire Antenna," Opt. Express, vol. 17, no. 4, pp. 2095–2110, 2009.
- [22] N. Gregersen, T. R. Nielsen, J. Mørk, J. Claudon, and J.-M. Gérard, "Designs for high-efficiency electrically pumped photonic nanowire single-photon sources," *Opt. Express*, vol. 18, no. 20, pp. 21204–21218, 2010.
- [23] S. N. Dorenbos, H. Sasakura, M. P. Van Kouwen, N. Akopian, S. Adachi, N. Namekata, M. Jo, J. Motohisa, Y. Kobayashi, K. Tomioka, T. Fukui, S. Inoue, H. Kumano, C. M. Natarajan, R. H. Hadfield, T. Zijlstra, T. M. Klapwijk,

V. Zwiller, and I. Suemune, "Position controlled nanowires for infrared single photon emission," *Appl. Phys. Lett.*, vol. 97, no. 17, p. 171106, 2010.

- [24] W. Srituravanich, N. Fang, C. Sun, Q. Luo, and X. Zhang, "Plasmonic Nanolithography," *Nano Lett.*, vol. 4, no. 6, pp. 1085–1088, 2004.
- [25] F. Tam, G. P. Goodrich, B. R. Johnson, and N. J. Halas, "Plasmonic Enhancement of Molecular Fluorescence," *Nano Lett.*, vol. 7, no. 2, pp. 496–501, 2007.
- [26] V. G. Kravets, G. Zoriniants, C. P. Burrows, F. Schedin, A. K. Geim, W. L. Barnes, and A. N. Grigorenko, "Composite Au Nanostructures for Fluorescence Studies in Visible Light," *Nano Lett.*, vol. 10, no. 3, pp. 874–879, 2010.
- [27] E. Dulkeith, M. Ringler, T. A. Klar, J. Feldmann, A. Muñoz Javier, and W. J. Parak, "Gold nanoparticles quench fluorescence by phase induced radiative rate suppression," *Nano Lett.*, vol. 5, no. 4, pp. 585–589, 2005.
- [28] S. Mayilo, M. A. Kloster, M. Wunderlich, A. Lutich, T. A. Klar, A. Nichtl, K. Kürzinger, F. D. Stefani, and J. Feldmann, "Long-Range Fluorescence Quenching by Gold Nanoparticles in a Sandwich Immunoassay for Cardiac Troponin T," *Nano Lett.*, vol. 9, no. 12, pp. 4558–4563, 2009.
- [29] A. E. Prigodich, P. S. Randeria, W. E. Briley, N. J. Kim, W. L. Daniel, D. A. Giljohann, and C. A. Mirkin, "Multiplexed Nanoflares: mRNA Detection in Live Cells," *Anal. Chem.*, vol. 84, no. 4, pp. 2062–2066, 2012.
- [30] P. L. Stiles, J. A. Dieringer, N. C. Shah, and R. P. Van Duyne, "Surface-Enhanced Raman Spectroscopy," *Annu. Rev. Anal. Chem.*, vol. 1, pp. 601–626, 2008.
- [31] M. Fleischmann, P. J. Hendra, and A. J. McQuillan, "Raman spectra of pyridine adsorbed at a silver electrode," *Chem. Phys. Lett.*, vol. 26, no. 2, pp. 163–166, 1974.
- [32] K. Kneipp, A. S. Haka, H. Kneipp, K. Badizadegan, N. Yoshizawa, C. Boone, K. E. Shafer-Peltier, J. T. Motz, R. R. Dasari, and M. S. Feld, "Surface-Enhanced Raman Spectroscopy in Single Living Cells Using Gold Nanoparticles," Appl. Spectrosc., vol. 56, no. 2, pp. 150–154, 2002.
- [33] J. F. Li, Y. F. Huang, Y. Ding, Z. L. Yang, S. B. Li, X. S. Zhou, F. R. Fan, W. Zhang, Z. Y. Zhou, D. Y. Wu, B. Ren, Z. L. Wang, and Z. Q. Tian, "Shell-isolated nanoparticle-enhanced Raman spectroscopy," *Nature*, vol. 464, no. 7287, pp. 392–395, 2010.
- [34] H. Liao, C. L. Nehl, and J. H. Hafner, "Biomedical applications of plasmon resonant metal nanoparticles," *Nanomedicine*, vol. 1, no. 2, pp. 201–208, 2006.

[35] A. J. Haes, L. Chang, W. L. Klein, and R. P. Van Duyne, "Detection of a biomarker for Alzheimer's disease from synthetic and clinical samples using a nanoscale optical biosensor," J. Am. Chem. Soc., vol. 127, no. 7, pp. 2264–2271, 2005.

- [36] K. M. Mayer, F. Hao, S. Lee, P. Nordlander, and J. H. Hafner, "A single molecule immunoassay by localized surface plasmon resonance," *Nanotechnology*, vol. 21, no. 25, p. 255503, 2010.
- [37] A. E. Cetin and H. Altug, "Fano Resonant Ring/Disk Plasmonic Nanocavities on Conducting Substrates for Advanced Biosensing," ACS Nano, vol. 6, no. 11, pp. 9989–9995, 2012.
- [38] C. Loo, A. Lowery, N. Halas, J. West, and R. Drezek, "Immunotargeted Nanoshells for Integrated Cancer Imaging and Therapy," *Nano Lett.*, vol. 5, no. 4, pp. 709– 711, 2005.
- [39] A. M. Gobin, M. H. Lee, N. J. Halas, W. D. James, R. A. Drezek, and J. L. West, "Near-Infrared Resonant Nanoshells for Combined Optical Imaging and Photothermal Cancer Therapy," *Nano Lett.*, vol. 7, no. 7, pp. 1929–1934, 2007.
- [40] G. F. Paciotti, L. Myer, D. Weinreich, D. Goia, N. Pavel, R. E. McLaughlin, and L. Tamarkin, "Colloidal Gold: A Novel Nanoparticle Vector for Tumor Directed Drug Delivery," *Drug Deliv.*, vol. 11, no. 3, pp. 169–183, 2004.
- [41] D. R. Smith, J. B. Pendry, and M. C. K. Wiltshire, "Metamaterials and negative refractive index," *Science*, vol. 305, no. 5685, pp. 788–792, 2004.
- [42] D. Schurig, J. J. Mock, B. J. Justice, S. A. Cummer, J. B. Pendry, A. F. Starr, and D. R. Smith, "Metamaterial electromagnetic cloak at microwave frequencies," *Science*, vol. 314, no. 5801, pp. 977–980, 2006.
- [43] N. Yu and F. Capasso, "Flat optics with designer metasurfaces," Nat. Mater., vol. 13, no. 2, pp. 139–150, 2014.
- [44] C. F. Bohren and D. R. Huffman, Absorption and Scattering of Light by Small Particles. Weinheim: Wiley-VCH, 1998.
- [45] J. Dorfmuller, R. Vogelgesang, W. Khunsin, C. Rockstuhl, C. Etrich, and K. Kern, "Plasmonic Nanowire Antennas: Experiment, Simulation, and Theory," Nano Lett., vol. 10, no. 9, pp. 3596–3603, 2010.
- [46] L. Novotny, "Effective Wavelength Scaling for Optical Antennas," Phys. Rev. Lett., vol. 98, no. 26, p. 266802, 2007.
- [47] J. M. Gaskell, M. Afzaal, D. W. Sheel, H. M. Yates, K. Delfanazari, and O. L. Muskens, "Optimised atmospheric pressure CVD of monoclinic VO₂ thin films with picosecond phase transition," Surf. Coatings Technol., vol. 287, pp. 160–165, 2016.

[48] R. Yan, D. Gargas, and P. Yang, "Nanowire photonics," Nat. Photonics, vol. 3, no. 10, pp. 569–576, 2009.

- [49] F. M. Ross, "Controlling nanowire structures through real time growth studies," *Reports Prog. Phys.*, vol. 73, no. 11, p. 114501, 2010.
- [50] A. E. Krasnok, A. E. Miroshnichenko, P. A. Belov, and Y. S. Kivshar, "All-Dielectric Optical Nanoantennas," Opt. Express, vol. 20, no. 18, pp. 20599–20604, 2012.
- [51] M. D. Birowosuto, A. Yokoo, G. Zhang, K. Tateno, E. Kuramochi, H. Taniyama, M. Takiguchi, and M. Notomi, "Movable High-Q Nanoresonators Realized by Semiconductor Nanowires on a Si Photonic Crystal Platform," *Nat. Mater.*, vol. 13, no. 3, pp. 279–285, 2014.
- [52] P. Albella, M. Ameen Poyli, M. K. Schmidt, S. A. Maier, F. Moreno, J. J. Sáenz, and J. Aizpurua, "Low-Loss Electric and Magnetic Field-Enhanced Spectroscopy with Subwavelength Silicon Dimers," J. Phys. Chem. C, vol. 117, no. 26, pp. 13573–13584, 2013.
- [53] U. Zywietz, M. K. Schmidt, A. B. Evlyukhin, C. Reinhardt, J. Aizpurua, and B. N. Chichkov, "Electromagnetic Resonances of Silicon Nanoparticle Dimers in the Visible," ACS Photonics, vol. 2, no. 7, pp. 913–920, 2015.
- [54] P. R. Wiecha, A. Arbouet, H. Kallel, P. Periwal, T. Baron, and V. Paillard, "Enhanced nonlinear optical response from individual silicon nanowires," *Phys. Rev. B*, vol. 91, no. 12, p. 121416, 2015.
- [55] A. Mirzaei and A. E. Miroshnichenko, "Electric and magnetic hotspots in dielectric nanowire dimers," *Nanoscale*, vol. 7, no. 14, pp. 5963–5968, 2015.
- [56] A. E. Miroshnichenko and Y. S. Kivshar, "Fano Resonances in All-Dielectric Oligomers," *Nano Lett.*, vol. 12, no. 12, pp. 6459–6463, 2012.
- [57] I. Staude, A. E. Miroshnichenko, M. Decker, N. T. Fofang, S. Liu, E. Gonzales, J. Dominguez, T. S. Luk, D. N. Neshev, I. Brener, and Y. Kivshar, "Tailoring Directional Scattering Through Magnetic and Electric Resonances in Subwavelength Silicon Nanodisks," ACS Nano, vol. 7, no. 9, pp. 7824–7832, 2013.
- [58] J. Suehiro, N. Nakagawa, S.-I. Hidaka, M. Ueda, K. Imasaka, M. Higashihata, T. Okada, and M. Hara, "Dielectrophoretic Fabrication and Characterization of a ZnO Nanowire-Based UV Photosensor," *Nanotechnology*, vol. 17, no. 10, pp. 2567– 2573, 2006.
- [59] A. Zhang, S. You, C. Soci, Y. Liu, D. Wang, and Y.-H. Lo, "Silicon Nanowire Detectors Showing Phototransistive Gain," Appl. Phys. Lett, vol. 93, no. 12, p. 121110, 2008.

[60] L. Cao, J.-S. Park, P. Fan, B. Clemens, and M. L. Brongersma, "Resonant Germanium Nanoantenna Photodetectors," *Nano Lett.*, vol. 10, no. 4, pp. 1229–1233, 2010.

- [61] V. Sivakov, G. Andrä, A. Gawlik, A. Berger, J. Plentz, F. Falk, and S. H. Christiansen, "Silicon Nanowire-Based Solar Cells on Glass: Synthesis, Optical Properties, and Cell Parameters," *Nano Lett.*, vol. 9, no. 4, pp. 1549–1554, 2009.
- [62] L. Cao, J. S. White, J.-S. Park, J. A. Schuller, B. M. Clemens, and M. L. Brongersma, "Engineering Light Absorption in Semiconductor Nanowire Devices," Nat. Mater., vol. 8, no. 8, pp. 643–647, 2009.
- [63] P. E. Landreman and M. L. Brongersma, "Deep-Subwavelength Semiconductor Nanowire Surface Plasmon Polariton Couplers," *Nano Lett.*, vol. 14, no. 2, pp. 429– 434, 2014.
- [64] O. L. Muskens, S. L. Diedenhofen, B. C. Kaas, R. E. Algra, E. P. A. M. Bakkers, J. Gómez Rivas, and A. Lagendijk, "Large photonic strength of highly tunable resonant nanowire materials," *Nano Lett.*, vol. 9, no. 3, pp. 930–934, 2009.
- [65] R. Paniagua-Domínguez, G. Grzela, J. Gómez Rivas, and J. A. Sánchez-Gil, "Enhanced and Directional Emission of Semiconductor Nanowires Tailored Through Leaky/Guided Modes," *Nanoscale*, vol. 5, no. 21, pp. 10582–10590, 2013.
- [66] E. Xifré-Pérez, R. Fenollosa, and F. Meseguer, "Low Order Modes in Microcavities Based on Silicon Colloids," *Opt. Express*, vol. 19, no. 4, pp. 3455–3463, 2011.
- [67] A. García-Etxarri, R. Gómez-Medina, L. S. Froufe-Pérez, C. López, L. Chantada, F. Scheffold, J. Aizpurua, M. Nieto-Vesperinas, and J. J. Sáenz, "Strong Magnetic Response of Submicron Silicon Particles in the Infrared," *Opt. Express*, vol. 19, no. 6, pp. 4815–4826, 2011.
- [68] M. K. Schmidt, R. Esteban, J. J. Sáenz, I. Suárez-Lacalle, S. Mackowski, and J. Aizpurua, "Dielectric antennas—a suitable platform for controlling magnetic dipolar emission," Opt. Express, vol. 20, no. 13, pp. 13636–50, 2012.
- [69] B. Rolly, J.-M. Geffrin, R. Abdeddaim, B. Stout, and N. Bonod, "Controllable emission of a dipolar source coupled with a magneto-dielectric resonant subwavelength scatterer," Sci. Rep., vol. 3, p. 3063, 2013.
- [70] W. Liu, A. E. Miroshnichenko, R. F. Oulton, D. N. Neshev, O. Hess, and Y. S. Kivshar, "Scattering of Core-Shell Nanowires with the Interference of Electric and Magnetic Resonances," Opt. Lett., vol. 38, no. 14, pp. 2621–2624, 2013.
- [71] M. K. Schmidt, J. Aizpurua, X. Zambrana-Puyalto, X. Vidal, G. Molina-Terriza, and J. J. Sáenz, "Isotropically polarized speckle patterns," *Phys. Rev. Lett.*, vol. 114, no. 11, p. 113902, 2015.

[72] A. García-Etxarri and J. A. Dionne, "Surface-enhanced circular dichroism spectroscopy mediated by nonchiral nanoantennas," *Phys. Rev. B*, vol. 87, no. 23, p. 235409, 2013.

- [73] A. B. Evlyukhin, S. M. Novikov, U. Zywietz, R. L. Eriksen, C. Reinhardt, S. I. Bozhevolnyi, and B. N. Chichkov, "Demonstration of magnetic dipole resonances of dielectric nanospheres in the visible region," *Nano Lett.*, vol. 12, no. 7, pp. 3749–3755, 2012.
- [74] P. Spinelli, M. A. Verschuuren, and A. Polman, "Broadband omnidirectional antireflection coating based on subwavelength surface Mie resonators," Nat. Commun., vol. 3, p. 692, 2012.
- [75] Y. Yang, W. Wang, P. Moitra, I. I. Kravchenko, D. P. Briggs, and J. Valentine, "Dielectric meta-reflectarray for broadband linear polarization conversion and optical vortex generation," *Nano Lett.*, vol. 14, no. 3, pp. 1394–1399, 2014.
- [76] C. Wu, N. Arju, G. Kelp, J. A. Fan, J. Dominguez, E. Gonzales, E. Tutuc, I. Brener, and G. Shvets, "Spectrally selective chiral silicon metasurfaces based on infrared Fano resonances," *Nat. Commun.*, vol. 5, p. 3892, 2014.
- [77] G. Grzela, R. Paniagua-Domínguez, T. Barten, Y. Fontana, J. A. Sánchez-Gil, and J. Gómez Rivas, "Nanowire Antenna Emission," *Nano Lett.*, vol. 12, no. 11, pp. 5481–5486, 2012.
- [78] G. Brönstrup, N. Jahr, C. Leiterer, A. Csáki, W. Fritzsche, and S. Christiansen, "Optical Properties of Individual Silicon Nanowires for Photonic Devices," ACS Nano, vol. 4, no. 12, pp. 7113–7122, 2010.
- [79] G. Chen, J. Wu, Q. Lu, H. R. Gutierrez, Q. Xiong, M. E. Pellen, J. S. Petko, D. H. Werner, and P. C. Eklund, "Optical Antenna Effect in Semiconducting Nanowires," *Nano Lett.*, vol. 8, no. 5, pp. 1341–1346, 2008.
- [80] J. Wu, A. K. Gupta, H. R. Gutierrez, and P. C. Eklund, "Cavity-enhanced stimulated raman scattering from short GaP nanowires," *Nano Lett.*, vol. 9, no. 9, pp. 3252–3257, 2009.
- [81] L. K. van Vugt, S. Rühle, P. Ravindran, H. C. Gerritsen, L. Kuipers, and D. Van-maekelbergh, "Exciton polaritons confined in a ZnO nanowire cavity," *Phys. Rev. Lett.*, vol. 97, no. 14, p. 147401, 2006.
- [82] R. F. Oulton, V. J. Sorger, T. Zentgraf, R.-M. Ma, C. Gladden, L. Dai, G. Bartal, and X. Zhang, "Plasmon lasers at deep subwavelength scale," *Nature*, vol. 461, no. 7264, pp. 629–632, 2009.
- [83] D. R. Abujetas, R. Paniagua-Domínguez, and J. A. Sánchez-Gil, "Unraveling the Janus Role of Mie Resonances and Leaky/Guided Modes in Semiconductor

Nanowire Absorption for Enhanced Light Harvesting," *ACS Photonics*, vol. 2, no. 7, pp. 921–929, 2015.

- [84] L. Huang, Y. Yu, and L. Cao, "General Modal Properties of Optical Resonances in Subwavelength Nonspherical Dielectric Structures," *Nano Lett.*, vol. 13, no. 8, pp. 3559–3565, 2013.
- [85] J. van de Groep and A. Polman, "Designing dielectric resonators on substrates: combining magnetic and electric resonances," Opt. Express, vol. 21, no. 22, pp. 26285–26302, 2013.
- [86] D.-J. Cai, Y.-H. Huang, W.-J. Wang, W.-B. Ji, J.-D. Chen, Z.-H. Chen, and S.-D. Liu, "Fano Resonances Generated in a Single Dielectric Homogeneous Nanoparticle with High Structural Symmetry," J. Phys. Chem. C, vol. 119, no. 8, pp. 4252–4260, 2015.
- [87] H.-S. Ee, J.-H. Kang, M. L. Brongersma, and M.-K. Seo, "Shape-dependent light scattering properties of subwavelength silicon nanoblocks," *Nano Lett.*, vol. 15, no. 3, pp. 1759–1765, 2015.
- [88] F. J. García de Abajo and A. Howie, "Relativistic Electron Energy Loss and Electron-Induced Photon Emission in Inhomogeneous Dielectrics," Phys. Rev. Lett., vol. 80, no. 23, pp. 5180–5183, 1998.
- [89] J. Aizpurua, G. W. Bryant, L. J. Richter, F. J. García de Abajo, B. K. Kelley, and T. Mallouk, "Optical Properties of Coupled Metallic Nanorods for Field-Enhanced Spectroscopy," Phys. Rev. B, vol. 71, no. 23, p. 235420, 2005.
- [90] A. Borghesi and G. Guizzetti, "Gallium Phosphide (GaP)," in Handbook of Optical Constants of Solids (E. D. Palik, ed.), pp. 445–464, London: Academic Press, 1998.
- [91] E. R. Encina and E. A. Coronado, "Near Field Enhancement in Ag Au Nanospheres Heterodimers," J. Phys. Chem. C, vol. 115, no. 32, pp. 15908–15914, 2011.
- [92] J. Fischer, N. Vogel, R. Mohammadi, H.-J. Butt, K. Landfester, C. K. Weiss, and M. Kreiter, "Plasmon Hybridization and Strong Near-Field Enhancements in Opposing Nanocrescent Dimers with Tunable Resonances," *Nanoscale*, vol. 3, no. 11, pp. 4788–4797, 2011.
- [93] G. F. Walsh and L. Dal Negro, "Enhanced Second Harmonic Generation by Photonic-Plasmonic Fano-Type Coupling in Nanoplasmonic Arrays," *Nano Lett.*, vol. 13, no. 7, pp. 3111–3117, 2013.
- [94] R. Fernández-García, Y. Sonnefraud, A. I. Fernández-Domínguez, V. Giannini, and S. A. Maier, "Design Considerations for Near-Field Enhancement in Optical Antennas," Contemp. Phys., vol. 55, no. 1, pp. 1–11, 2014.

[95] E. Xifré-Pérez, F. J. García de Abajo, R. Fenollosa, and F. Meseguer, "Photonic Binding in Silicon-Colloid Microcavities," *Phys. Rev. Lett.*, vol. 103, no. 10, p. 103902, 2009.

- [96] L. Cao, P. Fan, and M. L. Brongersma, "Optical Coupling of Deep-Subwavelength Semiconductor Nanowires," *Nano Lett.*, vol. 11, no. 4, pp. 1463–1468, 2011.
- [97] P. Albella, R. Alcaraz de la Osa, F. Moreno, and S. A. Maier, "Electric and Magnetic Field Enhancement with Ultralow Heat Radiation Dielectric Nanoantennas: Considerations for Surface-Enhanced Spectroscopies," ACS Photonics, vol. 1, no. 6, pp. 524–529, 2014.
- [98] M. R. Shcherbakov, A. S. Shorokhov, D. N. Neshev, B. Hopkins, I. Staude, E. V. Melik-Gaykazyan, A. A. Ezhov, A. E. Miroshnichenko, I. Brener, A. A. Fedyanin, and Y. S. Kivshar, "Nonlinear Interference and Tailorable Third-Harmonic Generation from Dielectric Oligomers," ACS Photonics, vol. 2, no. 5, pp. 578–582, 2015.
- [99] G. Schider, J. R. Krenn, A. Hohenau, H. Ditlbacher, A. Leitner, F. R. Aussenegg, W. L. Schaich, I. Puscasu, B. Monacelli, and G. Boreman, "Plasmon dispersion relation of Au and Ag nanowires," *Phys. Rev. B*, vol. 68, no. 15, p. 155427, 2003.
- [100] J. Dorfmüller, R. Vogelgesang, R. T. Weitz, C. Rockstuhl, C. Etrich, T. Pertsch, F. Lederer, and K. Kern, "Fabry-Pérot resonances in one-dimensional plasmonic nanostructures," *Nano Lett.*, vol. 9, no. 6, pp. 2372–2377, 2009.
- [101] C. P. Burrows and W. L. Barnes, "Large spectral extinction due to overlap of dipolar and quadrupolar plasmonic modes of metallic nanoparticles in arrays," Opt. Express, vol. 18, no. 3, pp. 3187–3198, 2010.
- [102] M. Kerker, D.-S. Wang, and C. L. Giles, "Electromagnetic scattering by magnetic spheres," J. Opt. Soc. Am., vol. 73, no. 6, pp. 765–767, 1983.
- [103] M. Nieto-Vesperinas, R. Gomez-Medina, and J. J. Saenz, "Angle-suppressed scattering and optical forces on submicrometer dielectric particles," J. Opt. Soc. Am. A, vol. 28, no. 1, pp. 54–60, 2011.
- [104] J. M. Geffrin, B. García-Cámara, R. Gómez-Medina, P. Albella, L. S. Froufe-Pérez, C. Eyraud, A. Litman, R. Vaillon, F. González, M. Nieto-Vesperinas, J. J. Sáenz, and F. Moreno, "Magnetic and electric coherence in forward- and back-scattered electromagnetic waves by a single dielectric subwavelength sphere," Nat. Commun., vol. 3, p. 1171, 2012.
- [105] P. Spinelli and A. Polman, "Light Trapping in Thin Crystalline Si Solar Cells Using Surface Mie Scatterers," *IEEE J. Photovoltaics*, vol. 4, no. 2, pp. 554–559, 2014.

[106] Y. H. Fu, A. I. Kuznetsov, A. E. Miroshnichenko, Y. F. Yu, and B. Luk'yanchuk, "Directional visible light scattering by silicon nanoparticles," *Nat. Commun.*, vol. 4, p. 1527, 2013.

- [107] J. Muller, G. Parent, G. Jeandel, and D. Lacroix, "Finite-difference time-domain and near-field-to-far-field transformation in the spectral domain: application to scattering objects with complex shapes in the vicinity of a semi-infinite dielectric medium," J. Opt. Soc. Am. A, vol. 28, no. 5, pp. 868–878, 2011.
- [108] S. Mokkapati, D. Saxena, H. H. Tan, and C. Jagadish, "Optical design of nanowire absorbers for wavelength selective photodetectors," Sci. Rep., vol. 5, p. 15339, 2015.
- [109] N. Strohfeldt, A. Tittl, M. Schäferling, F. Neubrech, U. Kreibig, R. Griessen, and H. Giessen, "Yttrium hydride nanoantennas for active plasmonics," *Nano Lett.*, vol. 14, no. 3, pp. 1140–1147, 2014.
- [110] F. Sterl, N. Strohfeldt, R. Walter, R. Griessen, A. Tittl, and H. Giessen, "Magnesium as Novel Material for Active Plasmonics in the Visible Wavelength Range," Nano Lett., vol. 15, no. 12, pp. 7949–7955, 2015.
- [111] R. F. Waters, P. A. Hobson, K. F. MacDonald, and N. I. Zheludev, "Optically switchable photonic metasurfaces," Appl. Phys. Lett., vol. 107, no. 8, p. 081102, 2015.
- [112] K. Shportko, S. Kremers, M. Woda, D. Lencer, J. Robertson, and M. Wuttig, "Resonant bonding in crystalline phase-change materials," *Nat. Mater.*, vol. 7, no. 8, pp. 653–658, 2008.
- [113] A.-K. U. Michel, D. N. Chigrin, T. W. W. Maß, K. Schönauer, M. Salinga, M. Wuttig, and T. Taubner, "Using low-loss phase-change materials for mid-infrared antenna resonance tuning," *Nano Lett.*, vol. 13, no. 8, pp. 3470–3475, 2013.
- [114] A.-K. U. Michel, P. Zalden, D. N. Chigrin, M. Wuttig, A. M. Lindenberg, and T. Taubner, "Reversible Optical Switching of Infrared Antenna Resonances with Ultrathin Phase-Change Layers Using Femtosecond Laser Pulses," ACS Photonics, vol. 1, no. 9, pp. 833–839, 2014.
- [115] P. Kühler, F. J. García de Abajo, P. Leiprecht, A. Kolloch, J. Solis, P. Leiderer, and J. Siegel, "Quantitative imaging of the optical near field," *Opt. Express*, vol. 20, no. 20, pp. 22063–22078, 2012.
- [116] Y. Katsumata, T. Morita, Y. Morimoto, T. Shintani, and T. Saiki, "Self-organization of a periodic structure between amorphous and crystalline phases in a GeTe thin film induced by femtosecond laser pulse amorphization," Appl. Phys. Lett., vol. 105, no. 3, p. 031907, 2014.

[117] A. Tittl, A.-K. U. Michel, M. Schäferling, X. Yin, B. Gholipour, L. Cui, M. Wuttig, T. Taubner, F. Neubrech, and H. Giessen, "A Switchable Mid-Infrared Plasmonic Perfect Absorber with Multispectral Thermal Imaging Capability," Adv. Mater., vol. 27, no. 31, pp. 4597–4603, 2015.

- [118] J. Y. Suh, E. U. Donev, R. Lopez, L. C. Feldman, and R. F. Haglund Jr., "Modulated optical transmission of subwavelength hole arrays in metal-VO₂ films," *Appl. Phys. Lett.*, vol. 88, no. 13, p. 133115, 2006.
- [119] M. A. Kats, R. Blanchard, P. Genevet, Z. Yang, M. M. Qazilbash, D. N. Basov, S. Ramanathan, and F. Capasso, "Thermal tuning of mid-infrared plasmonic antenna arrays using a phase change material," *Opt. Lett.*, vol. 38, no. 3, pp. 368–370, 2013.
- [120] K. Appavoo and R. F. Haglund Jr., "Polarization selective phase-change nanomodulator," *Sci. Rep.*, vol. 4, p. 6771, 2014.
- [121] K. Appavoo, B. Wang, N. F. Brady, M. Seo, J. Nag, R. P. Prasankumar, D. J. Hilton, S. T. Pantelides, and R. F. Haglund Jr., "Ultrafast phase transition via catastrophic phonon collapse driven by plasmonic hot-electron injection," *Nano Lett.*, vol. 14, no. 3, pp. 1127–1133, 2014.
- [122] A. Zylbersztejn and N. F. Mott, "Metal-insulator transition in vanadium dioxide," *Phys. Rev. B*, vol. 11, no. 11, pp. 4383–4395, 1975.
- [123] R. M. Wentzcovitch, W. W. Schulz, and P. B. Allen, "VO₂: Peierls or Mott-Hubbard? A view from band theory," *Phys. Rev. Lett.*, vol. 72, no. 21, pp. 3389–3392, 1994.
- [124] T. M. Rice, H. Launois, and J. P. Pouget, "Comment on 'VO₂: Peierls or Mott-Hubbard? A view from band theory'," *Phys. Rev. Lett.*, vol. 73, no. 22, p. 3042, 1994.
- [125] R. M. Wentzcovitch, W. W. Schulz, and P. B. Allen, "Wentzcovitch et al. reply," Phys. Rev. Lett., vol. 73, no. 22, p. 3043, 1994.
- [126] A. Cavalleri, T. Dekorsy, H. H. W. Chong, J. C. Kieffer, and R. W. Schoenlein, "Evidence for a structurally-driven insulator-to-metal transition in VO₂: A view from the ultrafast timescale," *Phys. Rev. B*, vol. 70, no. 16, p. 161102, 2004.
- [127] H.-T. Kim, Y. W. Lee, B.-J. Kim, B.-G. Chae, S. J. Yun, K.-Y. Kang, K.-J. Han, K.-J. Yee, and Y.-S. Lim, "Monoclinic and correlated metal phase in VO₂ as evidence of the Mott transition: coherent phonon analysis," *Phys. Rev. Lett.*, vol. 97, no. 26, p. 266401, 2006.
- [128] Z. Yang, C. Ko, and S. Ramanathan, "Oxide Electronics Utilizing Ultrafast Metal-Insulator Transitions," *Annu. Rev. Mater. Res.*, vol. 41, pp. 337–367, 2011.

[129] S. Chen, J. Liu, H. Luo, and Y. Gao, "Calculation Evidence of Staged Mott and Peierls Transitions in VO₂ Revealed by Mapping Reduced-Dimension Potential Energy Surface," J. Phys. Chem. Lett., vol. 6, no. 18, pp. 3650–3656, 2015.

- [130] N. F. Mott, Metal-Insulator Transitions. London: Taylor & Francis, 2nd ed., 1999.
- [131] N. F. Mott and R. Peierls, "Discussion of the paper by de Boer and Verwey," *Proc. Phys. Soc.*, vol. 49, no. 4S, pp. 72–73, 1937.
- [132] G. Grüner, "The dynamics of charge-density waves," Rev. Mod. Phys., vol. 60, no. 4, pp. 1129–1181, 1988.
- [133] M. W. Haverkort, Z. Hu, A. Tanaka, W. Reichelt, S. V. Streltsov, M. A. Korotin, V. I. Anisimov, H. H. Hsieh, H.-J. Lin, C. T. Chen, D. I. Khomskii, and L. H. Tjeng, "Orbital-assisted metal-insulator transition in VO₂," *Phys. Rev. Lett.*, vol. 95, no. 19, p. 196404, 2005.
- [134] M. M. Qazilbash, M. Brehm, B.-G. Chae, P.-C. Ho, G. O. Andreev, B.-J. Kim, S. J. Yun, A. V. Balatsky, M. B. Maple, F. Keilmann, H.-T. Kim, and D. N. Basov, "Mott transition in VO₂ revealed by infrared spectroscopy and nano-imaging," *Science*, vol. 318, no. 5857, pp. 1750–1753, 2007.
- [135] A. Zimmers, L. Aigouy, M. Mortier, A. Sharoni, S. Wang, K. G. West, J. G. Ramirez, and I. K. Schuller, "Role of thermal heating on the voltage induced insulator-metal transition in VO₂," *Phys. Rev. Lett.*, vol. 110, no. 5, p. 056601, 2013.
- [136] A. Cavalleri, C. Tóth, C. W. Siders, J. A. Squier, F. Ráksi, P. Forget, and J. C. Kieffer, "Femtosecond Structural Dynamics in VO₂ during an Ultrafast Solid-Solid Phase Transition," *Phys. Rev. Lett.*, vol. 87, no. 23, p. 237401, 2001.
- [137] S. Wall, D. Wegkamp, L. Foglia, K. Appavoo, J. Nag, R. F. Haglund Jr., J. Stähler, and M. Wolf, "Ultrafast changes in lattice symmetry probed by coherent phonons," Nat. Commun., vol. 3, p. 721, 2012.
- [138] S. Wall, L. Foglia, D. Wegkamp, K. Appavoo, J. Nag, R. F. Haglund Jr., J. Stähler, and M. Wolf, "Tracking the evolution of electronic and structural properties of VO₂ during the ultrafast photoinduced insulator-metal transition," *Phys. Rev. B*, vol. 87, no. 11, p. 115126, 2013.
- [139] D. Wegkamp and J. Stähler, "Ultrafast dynamics during the photoinduced phase transition in VO₂," *Prog. Surf. Sci.*, vol. 90, no. 4, pp. 464–502, 2015.
- [140] P. B. Allen, R. M. Wentzcovitch, W. W. Schulz, and P. C. Canfield, "Resistivity of the high-temperature metallic phase of VO₂," *Phys. Rev. B*, vol. 48, no. 7, pp. 4359–4363, 1993.

[141] V. J. Emery and S. A. Kivelson, "Superconductivity in bad metals," *Phys. Rev. Lett.*, vol. 74, no. 16, pp. 3253–3256, 1995.

- [142] M. M. Qazilbash, K. S. Burch, D. Whisler, D. Shrekenhamer, B. G. Chae, H. T. Kim, and D. N. Basov, "Correlated metallic state of vanadium dioxide," *Phys. Rev. B*, vol. 74, no. 20, p. 205118, 2006.
- [143] B. M. Reinhard, M. Siu, H. Agarwal, A. P. Alivisatos, and J. Liphardt, "Calibration of Dynamic Molecular Rulers Based on Plasmon Coupling between Gold Nanoparticles," *Nano Lett.*, vol. 5, no. 11, pp. 2246–2252, 2005.
- [144] P. K. Jain, W. Huang, and M. A. El-Sayed, "On the Universal Scaling Behavior of the Distance Decay of Plasmon Coupling in Metal Nanoparticle Pairs: A Plasmon Ruler Equation," *Nano Lett.*, vol. 7, no. 7, pp. 2080–2088, 2007.
- [145] C.-p. Huang, X.-g. Yin, L.-b. Kong, and Y.-y. Zhu, "Interactions of Nanorod Particles in the Strong Coupling Regime," *J. Phys. Chem. C*, vol. 114, no. 49, pp. 21123–21131, 2010.
- [146] Y. D. Chong, L. Ge, H. Cao, and A. D. Stone, "Coherent perfect absorbers: Time-reversed lasers," Phys. Rev. Lett., vol. 105, no. 5, p. 053901, 2010.
- [147] A. Yariv, "Critical coupling and its control in optical waveguide-ring resonator systems," *IEEE Photonics Technol. Lett.*, vol. 14, no. 4, pp. 483–485, 2002.
- [148] W. Wan, Y. Chong, L. Ge, H. Noh, A. D. Stone, and H. Cao, "Time-reversed lasing and interferometric control of absorption," *Science*, vol. 331, no. 6019, pp. 889–892, 2011.
- [149] A. Mock, "Low-Power All-Optical Switch Based on Time-Reversed Microring Laser," *IEEE Photonics J.*, vol. 4, no. 6, pp. 2229–2235, 2012.
- [150] R. R. Grote, J. B. Driscoll, and R. M. Osgood Jr., "Integrated optical modulators and switches using coherent perfect loss," Opt. Lett., vol. 38, no. 16, pp. 3001–3004, 2013.
- [151] H. Park, S.-Y. Lee, J. Kim, B. Lee, and H. Kim, "Near-infrared coherent perfect absorption in plasmonic metal-insulator-metal waveguide," *Opt. Express*, vol. 23, no. 19, pp. 24464–24474, 2015.
- [152] J. M. Rothenberg, C. P. Chen, J. J. Ackert, J. I. Dadap, A. P. Knights, K. Bergman, R. M. Osgood Jr., and R. R. Grote, "Experimental demonstration of coherent perfect absorption in a silicon photonic racetrack resonator," *Opt. Lett.*, vol. 41, no. 11, pp. 2537–2540, 2016.
- [153] R. Bruck and O. L. Muskens, "Plasmonic nanoantennas as integrated coherent perfect absorbers on SOI waveguides for modulators and all-optical switches," *Opt. Express*, vol. 21, no. 23, pp. 27652–27661, 2013.

- [154] C. R. Pollock and M. Lipson, Integrated Photonics. Dordrecht: Kluwer, 2003.
- [155] T. Suhara and H. Nishihara, "Integrated optics components and devices using periodic structures," *IEEE J. Quantum Electron.*, vol. 22, no. 6, pp. 845–867, 1986.
- [156] S. Ura, T. Fujii, T. Suhara, and H. Nishihara, "Efficiency-enhanced third-order grating coupler," Appl. Opt., vol. 38, no. 14, pp. 3003–3007, 1999.
- [157] D. Taillaert, P. Bienstman, and R. Baets, "Compact efficient broadband grating coupler for silicon-on-insulator waveguides," Opt. Lett., vol. 29, no. 23, pp. 2749– 2751, 2004.
- [158] P. Cheben, S. Janz, D.-X. Xu, B. Lamontagne, A. Delage, and S. Tanev, "A broad-band waveguide grating coupler with a subwavelength grating mirror," *IEEE Photonics Technol. Lett.*, vol. 18, no. 1, pp. 13–15, 2006.
- [159] D. Taillaert, F. Van Laere, M. Ayre, W. Bogaerts, D. Van Thourhout, P. Bienstman, and R. Baets, "Grating Couplers for Coupling between Optical Fibers and Nanophotonic Waveguides," *Jpn. J. Appl. Phys.*, vol. 45, no. 8A, pp. 6071–6077, 2006.
- [160] X. Chen, C. Li, C. K. Y. Fung, S. M. G. Lo, and H. K. Tsang, "Apodized Waveguide Grating Couplers for Efficient Coupling to Optical Fibers," *IEEE Photonics Technol. Lett.*, vol. 22, no. 15, pp. 1156–1158, 2010.
- [161] C. Li, H. Zhang, M. Yu, and G. Q. Lo, "CMOS-compatible high efficiency doubleetched apodized waveguide grating coupler," Opt. Express, vol. 21, no. 7, pp. 7868– 7874, 2013.
- [162] S. Somekh, E. Garmire, A. Yariv, H. Garvin, and R. Hunsperger, "Channel optical waveguide directional couplers," *Appl. Phys. Lett.*, vol. 22, no. 1, pp. 46–47, 1973.
- [163] R. R. A. Syms and J. R. Cozens, Optical Guided Waves and Devices. Maidenhead: McGraw-Hill, 1992.
- [164] M. Hu, C. Novo, A. Funston, H. Wang, H. Staleva, S. Zou, P. Mulvaney, Y. Xia, and G. V. Hartland, "Dark-field microscopy studies of single metal nanoparticles: understanding the factors that influence the linewidth of the localized surface plasmon resonance," J. Mater. Chem., vol. 18, no. 17, pp. 1949–1960, 2008.
- [165] T. H. Taminiau, F. D. Stefani, F. B. Segerink, and N. F. van Hulst, "Optical antennas direct single-molecule emission," *Nat. Photonics*, vol. 2, no. 4, pp. 234– 237, 2008.
- [166] A. G. Curto, G. Volpe, T. H. Taminiau, M. P. Kreuzer, R. Quidant, and N. F. van Hulst, "Unidirectional Emission of a Quantum Dot Coupled to a Nanoantenna," Science, vol. 329, no. 5994, pp. 930–933, 2010.

[167] M. Barmentlo, G. W. 't Hooft, E. R. Eliel, E. W. M. van der Ham, Q. H. F. Vrehen, A. F. G. van der Meer, and P. W. van Amersfoort, "Sum-frequency generation with a free-electron laser: A study of gallium phosphide," *Phys. Rev. A*, vol. 50, no. 1, pp. R14–R17, 1994.

- [168] V. A. Mel'nikov, L. A. Golovan, S. O. Konorov, D. A. Muzychenko, A. B. Fedotov, A. M. Zheltikov, V. Y. Timoshenko, and P. K. Kashkarov, "Second-harmonic generation in strongly scattering porous gallium phosphide," *Appl. Phys. B*, vol. 79, no. 2, pp. 225–228, 2004.
- [169] K. Rivoire, Z. Lin, F. Hatami, W. T. Masselink, and J. Vučković, "Second harmonic generation in gallium phosphide photonic crystal nanocavities with ultralow continuous wave pump power," Opt. Express, vol. 17, no. 25, pp. 22609–22615, 2009.
- [170] T. H. Taminiau, F. D. Stefani, and N. F. van Hulst, "Enhanced directional excitation and emission of single emitters by a nano-optical Yagi-Uda antenna," Opt. Express, vol. 16, no. 14, pp. 10858–10866, 2008.
- [171] T. Kosako, Y. Kadoya, and H. F. Hofmann, "Directional control of light by a nano-optical YagiUda antenna," *Nat. Photonics*, vol. 4, no. 5, pp. 312–315, 2010.
- [172] T. Coenen, E. J. R. Vesseur, A. Polman, and A. F. Koenderink, "Directional Emission from Plasmonic YagiUda Antennas Probed by Angle-Resolved Cathodoluminescence Spectroscopy," Nano Lett., vol. 11, no. 9, pp. 3779–3784, 2011.